SIMULATION AND DESIGN OF SOFT ROBOTIC SWIMMERS WITH ARTIFICIAL MUSCLE

By

Andrew Michael Hess

A DISSERTATION

Submitted to
Michigan State University
in partial fulfillment of the requirements
for the degree of

Mechanical Engineering – Doctor of Philosophy Computational Mathematics, Science, and Engineering – Dual Major

ABSTRACT

SIMULATION AND DESIGN OF SOFT ROBOTIC SWIMMERS WITH ARTIFICIAL MUSCLE

By

Andrew Michael Hess

Soft robots take advantage of rich nonlinear dynamics and large degrees of freedom to perform actions often by novel means beyond the capability of conventional rigid robots. Nevertheless, there are considerable challenges in analysis, design, and optimization of soft robots due to their complex behaviors. This is especially true for soft robotic swimmers whose dynamics are determined by highly nonlinear fluid-structure interactions. We present a holistic computational framework that employs a multi-objective evolutionary method to optimize feedback controllers for maneuvers of a soft robotic fish under artificial muscle actuation.

The resultant fluid-structure interactions are fully solved by using a novel fictitious domain/active strain method, developed to numerically study the swimming motion of thin, light-weight soft robots composed of smart materials that can actively undergo reversible large deformations. We assume the elastic material to be neo-Hookean, and behave like an artificial "muscle" which, when stimulated, generates a principal stretch of contraction. Instead of imposing active stresses, here we adopt an active strain approach to impose contracting strains to drive elastic deformation following a multiplicative decomposition of the deformation gradient tensor. The hydrodynamic coupling between the fluid and the solid is then resolved by using the fictitious domain method where the induced flow field is virtually extended into the solid domain. Pseudo body forces are employed to enforce the interior fictitious fluid motion to be the same as the structural movement. To demonstrate this method we carry out a series of numerical explorations for soft robotic swimmers of both 2D and 3D geometries that prove these robot prototypes can effectively perform undulatory and jet-propulsion locomotion when active contracting strains are appropriately distributed on elastica.

To complete our framework we then demonstrate the design and optimization of a maneuverable, undulatory, soft robotic fish. In particular, we consider a two-dimensional elastic plate with finite thickness, subjected to active contractile strains on both sides of the body. Compared to the conventional approaches that require specifying the entire-body curvature variation, we demonstrate that imposing contractile active strains locally can produce various swimming gaits, such as forward swimming and turning, using far fewer control parameters. The parameters of a pair of proportional-integral-derivative (PID) controllers, used to control the amplitude and the bias of the active strains, respectively, are optimized for tracking a moving target involving different trajectories and Reynolds numbers, with three objectives, tracking error, cost of transport, and elastic strain energy. The resulting Pareto fronts of the multi-objective optimization problem reveal the correlation and trade-off among the objectives and offer key insight into the design and control of soft swimmers.

Furthermore, we expand upon these core studies by investigating a variety processes and phenomena that are of potential importance to the design of soft robotic fish. Rich and complex phenomena occur at the interface between fluids and elastic solids that can influence the behavior of the overall system. This is especially true in the case of soft robots where wrinkling, folding, and similar wavelike behavior can occur at the surface and affect the momentum transfer which is necessary to produce locomotion. To begin to understand this behavior we analytically investigate the linear stability of a viscoelastic gel-like film subjected to Newtonian Couette flow in the limit of vanishing Reynolds number.

The final avenue of study attempts to answer the question of how to design and optimize the body shape in conjunction with the actuation scheme of a soft robotic fish. The flexibility of soft materials and actuators lead to large degrees of freedom creating a wide array of possibilities but at the same time overwhelming the traditional design process. We demonstrate a viable solution to this issue by using evolutionary optimization to simultaneously optimize both the shape and actuation of a simple 2D soft robotic fish in a simple case study.

Copyright by ANDREW MICHAEL HESS 2019



ACKNOWLEDGEMENTS

First and foremost I would like to thank my advisor, Dr. Tong Gao, for his expertise and guidance throughout the projects that make up this dissertation. As his first doctoral student, this process was a learning experience for us both and I believe one that left us both the better for it. I hope that the feeling is mutual and that our continued collaborations will bear fruit for years to come.

I would like to thank my committee members, Dr. Farhad Jaberi, Dr. Ahmed Naguib, and Dr. Mohsen Zayernouri for their support, suggestions, and imparted wisdom from the beginning as I sat in their classrooms to the very end as I stood before them to defend my work.

I gratefully acknowledge my collaborators such as Dr. Xiaobo Tan and Dr. Zhaowu Lin among innumerable others who have and continue to share their knowledge and expertise without which none of this would have been possible.

Last but not least, I thank those who supported me through thick and thin. Mom & Dad and my grandparents who were always there for me regardless of how rocky the path, at times, became. Brittany, my longtime partner in crime, who stuck with me from undergrad through all the trials and tribulations that lead to us each becoming some variety of "Dr". And friends new and old whose companionship kept me sane along the way, Krissy, Coco, Mattei, Seward, Kevin, Chris, Rachel, Joe, Chad, Taylor, Connor, Sanders, ...

TABLE OF CONTENTS

LIST OF	TABI	ES	ix
LIST OF	FIGU	RES	X
CHAPT	ER 1	INTRODUCTION	1
CHAPT	ER 2	STABILITY OF COUETTE FLOW PAST A GEL FILM	4
2.1	Mathe	matical Model	5
	2.1.1	Constitutive equations	5
	2.1.2	Universal Eulerian description	7
2.2	Linear	Stability Analysis	9
	2.2.1	Base state	9
	2.2.2		10
2.3	Result	S	12
	2.3.1		12
	2.3.2		13
	2.3.3		15
2.4			16
CHAPT	ED 2	A ELLUD CEDUCEUDE INTEDACTION CEUDY OF COFT DODOTIC	
CHAPI	EK 3	A FLUID-STRUCTURE INTERACTION STUDY OF SOFT ROBOTIC	10
2.1	N f . d		19
3.1			20
	3.1.1		20
	3.1.2		21
	3.1.3		23
			23
			25
			27
3.2			29
	3.2.1		31
	3.2.2	Three-Dimensional Cases	
			36
			38
		\mathcal{E}	40
3.3	Concl	uding Remarks	44
CHAPT	ER 4	CFD-BASED MULTI-OBJECTIVE CONTROLLER OPTIMIZATION	
		FOR SOFT ROBOTIC FISH WITH MUSCLE-LIKE ACTUATION	47
4.1	Mathe	matical Model	48
4.2	Contro		52
	4.2.1		52
	4.2.2	Multi-Objective Optimization	

4.3	Result	and Discussion	(
	4.3.1	Undulatory Swimming	6
	4.3.2	Optimization and Analysis	58
		4.3.2.1 Trajectory Comparison	58
		4.3.2.2 Pareto Fronts of Optimized Solutions 6)(
		4.3.2.3 Objective Correlations and Parameter Trends 6	2
4.4	Conclu	ding Remarks	5
СНАРТ	ER 5	FUTURE WORK	57
5.1	Body S	hape Optimization for Muscle Driven Undulatory Swimming 6) 7
CHAPT	ER 6	CONCLUSIONS	']
RIRLIO	GRAPI	Y 7	17

LIST OF TABLES

Table 3.1:	The amplitude of the central point on the free end and the Strouhal number and the average drag coefficient for a flexible beam	29
Table 3.2:	The amplitude of the central point on the plate trailing edge and the Strouhal number and the average drag coefficient for a flag flapping in uniform flow	30
Table 4.1:	Summary of the variables (PID tuning parameters) and objectives considered in the optimization	56

LIST OF FIGURES

Figure 2.1:	Schematic for a Couette flow past a gel film. Nonlinear solid models: (a) neo-Hookean, (b) Kelvin-Voigt, (c) Zener	•	5
Figure 2.2:	The growth rate $Re(\alpha)$ as a function of k for the neo-Hookean solid: (a) $H=0.4, T=0$; (b) $H=4.0, T=0$; (c) $H=0.4, T=10$; (d) $H=4.0, T=10$. The open circles are the results obtained by Gkanis & Kumar [33]		12
Figure 2.3:	Comparison of the growth rate $Re(\alpha)$ as a function of k for the neo-Hookean, Kelvin-Voigt, and Zener solids: (a) $H=0.4, T=0, G=5$; (b) $H=4.0, T=0, G=5$; (c) $H=0.4, T=10, G=11$; (d) $H=4.0, T=10, G=5$		13
Figure 2.4:	(a) Schematic for a sinusoidal surface perturbation. The contributions of the first normal-stress difference and the solid viscous effect are marked by the black and red solid arrows, respectively. The open arrows represent the stabilizing effect due to surface tension. (b,c): Critical values of the imposed strain G_c and the critical wavenumber k_c as a function of H . The black dotted lines are drawn at the locations where either G_c or k_c tends to infinity. Inset in (c): Growth-rate curves near $H \approx 1$ where short-wave instabilities recur.		14
Figure 3.1:	Schematic of the 1D three element Hill's muscle model. It is composed of a contractile element (CE) in series with a nonlinear spring (SE) which are both in parallel with another nonlinear spring (PE)		21
Figure 3.2:	Time evolution of the displacements in both x - and y -directions of the central point on the plate trailing edge (point A, see inset of (a)) of a thin flexible plate in uniform flow	•	28
Figure 3.3:	Time evolution of the transverse displacement of the central point on the plate trailing edge of a thin flexible plate in uniform flow	•	30
Figure 3.4:	(a) Schematic of a 2D beam under contracting actuation. The active segment is highlighted in orange. The microscopic mechanical model of the active contraction is illustrated by the zoom-in schematic on bottom. (b) Either a constant (i.e., a step-like) or a sinusoidal contraction is applied during the first half period $0 \le t < T/2$ on the two surfaces alternatively. Then the actuation is turned off for the second half $T/2 \le t < T$. (c) Convergence study for the 2D beam under a sinusoidal actuation by varying domain size, mesh resolution, and time step. The other parameters are Re = 500, $G = 1000$, $\delta = 0.4$, $\alpha = 0.15$, and $T = 2$	•	31

Figure 3.5:	Swimming motions of a 2D elastic beam under the constant and sinusoidal actuation when fixing Re = 500 and $T = 2.0$. (a) Instantaneous velocity as a function time. (b) Strain energy E as a function of time. Inset in (b): Envelope trajectories of the plate midline during one actuation period. Snapshots of the corresponding vorticity fields are shown in panels (c) (constant) and (d) (sinusoidal)	32
Figure 3.6:	100 and Re = 500 when fixing $T = 1.0$ for sinusoidal actuation following Eq. (3.20). (a) Instantaneous velocities as a function time. (b) Mean elastic energy densities e as a function of time. Inset in (b): Envelope trajectories of the plate midline during one actuation period. Snapshots of the corresponding vorticity fields are shown in panels (c) at Re = 100 and (d) at Re = 500,	32
Figure 3.7:	Measurements of the averaged swimming speed $\langle U \rangle$ in (a-c), and power P (solid blue lines) and efficiency η (dashed blue lines) in (d-f) of an swimming beam under a sinusoidal actuation following Eq. (3.20) when fixing Re = 500, α = 0.15, and varying T , G and δ , respectively	34
Figure 3.8:	(a) Examples of different actuation patterns (horizontal vs. diagonal) on the top surface of a square plate, and the corresponding bending deformations in (b) and (c)	36
Figure 3.9:	Snapshots of circular plate under (a-c) radial and (d-e) azimuthal actuation	36
Figure 3.10:	Snapshots of an oblate bell under (a-c) radial and (d-e) azimuthal actuation	37
Figure 3.11:	Snapshots of 3D vortex-core structures (a) and the projection of 2D vortices on the $x-y$ plane (b) of an elastic plate that performs undulation under a sinusoidal actuation following Eq. (3.20). The computation parameters are chosen as $\alpha=0.2$, $\delta=0.5$, $T=1.0$, $G=1000$, and $R=1000$. (c) Instantaneous swimming velocity as a function of time. The color bar represents the magnitude of the 3D vorticity, i.e., $ \omega_f $ (b) Drag coefficient	
	$C_d = F_y / \left(\frac{1}{2} \langle U \rangle^2 A\right)$ (red line) and wake-induced force (i.e., Lamb vector)	
	coefficient $C_w = -F_L/\left(\frac{1}{2}\langle U\rangle^2 A\right)$ (blue line) as functions of time. (e) Strain energy E as a function of time	38
Figure 3.12:	Simulation results of an undulating swimming motion by varying δ while fixing $\alpha = 0.2$, $T = 1.0$, $G = 1000$ and $Re = 1000$. (a) Instantaneous swimming speed U at $\delta = 0.3, 0.5, 0.7$, respectively. (b) Time-averaged swimming speed $\langle U \rangle$ and strain energy $\langle E \rangle$ as a function of δ for periodic locomotion. (c) Power P and efficiency n as a function of δ	2 0
	locomotion. (c) Power P and efficiency η as a function of δ	9

Figure 3.13:	Typical vortex structures of an elastic bell undergoing jellyfish-like swimming in the moving coordinates, when choosing $\alpha=0.8$, $T=2.0$, $G=100$, $Re=500$, $\varepsilon=0.1$, $\delta=0.21$, and $h=0.03$. (a) Vortex core overlaid on the solid mesh. The color bar represents the magnitude of the 3D vorticity, i.e., $ \omega_f $. Inset: Schematic of the swimming elastic bell with a thickened top and azimuthal actuation. (b-i) In-plane fluid velocity vector field (u,v) overlaid on the colormap of vorticity on a 2D cross section plane during one period	41
Figure 3.14:	Highlights of bell's rowing motion accompanying whole-body vibrations through the kinematics of the bell arm during the contracting and refilling process (a). The instantaneous strain energy (b) and COM velocity(c) as function of time.	42
Figure 3.15:	(a) Phase diagram of (α, Re) for a swimming bell undergoing jet-propulsion locomotion. The while and black symbols represent the forward and backward locomotion, respectively. The background color represents the time-averaged steady-state swimming velocity $\langle U \rangle$ at late times. (b) Typical instantaneous COM velocities when choosing $\alpha's$ in different regimes at $\text{Re}=250.\ldots$.	42
Figure 3.16:	Comparison of the dynamics of soft robotic baby-jellyfish by distributing active contractions (marked by the blue lines) on (a) arms (i.e., radially) and partial of the circular disk (i.e., azimuthally), and (b) arms only. The four sequential snapshots in (a) highlight a stable directional locomotion in one actuation period. The snapshot in (b) shows an example of unstable asymmetric deformations without applying the azimuthal contraction in the disk to stabilize the structure.	45
Figure 4.1:	(a) Schematic of a 2D beam under contractile actuation (view from above). The active segment is of length δ . The microscopic mechanical model of the active contraction is illustrated by the zoom-in schematic on bottom. (b) Contractile actuation applied alternatively on the surfaces of two sides, which exponentially decays in the thickness (y) direction (not shown in the figure).	49
Figure 4.2:	Schematic illustrating the control scheme based on the translational and rotational motion of a soft swimmer in relation to a moving target \mathbf{x}_t	52
Figure 4.3:	Free-swimming of a 2D elastic beam at Re = 500 and T = 2.0. (a) Instantaneous snapshot of vorticity field. (b) Envelope trajectories of the beam midline during one actuation period: (top) numerical results; (bottom) fitted results by Eq. (4.14). (c) Mean values of \overline{U} , \overline{E} , and C_{ot} as function of contraction strength α	57
Figure 4.4:	Simulation results for the soft swimmer at $\alpha_0 = 0.2$, Re = 500, and $G = 1000$: (a) Center of mass (CoM) paths at different values of β ; (b) Turning curvature R^{-1} as a function of β	58

Figure 4.5:	CoM trajectories of a soft swimmer tracking a moving target that is moving along both the (a) straight and (b) sinusoidal paths (black lines), when the swimmer is subjected to the PID control. The (red) and (blue) lines correspond to the controllers that have the lowest and a moderate error \bar{e} (but lowest elastic energy \bar{E}), respectively. The black arrows mark the target's moving directions	60
Figure 4.6:	Pareto fronts in the space of tracking error (\bar{e}) , cost of transport (C_{ot}) , and elastic strain energy (\bar{E}) for various target speeds v with Re = 500. Bluesquare: $v = 0.1$. Red-triangle: $v = 0.2$. Green-circle: $v = 0.3$. Straight path: (a-d). Sinusoidal path: (e-h). The leftmost panels (a) and (e) are 3D views of the objective spaces. The panels to their right are 2D projections of the respective distribution that visualize the trends between each pair of objectives. (b) and (f): \bar{e} vs C_{ot} . (c) and (g): \bar{e} vs \bar{E} . (d) and (h): C_{ot} vs \bar{E}	62
Figure 4.7:	Pareto fronts in the space of tracking error (\bar{e}) , cost of transport (C_{ot}) , and elastic strain energy (\bar{E}) for various Re with $v=0.2$. Blue-square: Re = 500. Red-triangle: Re = 1000. Green-circle: Re = 1500. Yellow-diamond: Re = 2000. Straight path: (a-d). Sinusoidal path: (e-h). The leftmost panels (a) and (e) are 3D views of the objective spaces. The panels to their right are 2D projections of the respective distribution that visualize the trends between each pair of objectives. (b) and (f): \bar{e} vs C_{ot} . (c) and (g): \bar{e} vs \bar{E} . (d) and (h): C_{ot} vs \bar{E}	63
Figure 4.8:	Comparison of the Pearson correlation coefficients (ρ) of the objectives for varying v (left) and varying Re (right). Blue-square = \bar{e} to C_{ot} . Red-triangle = \bar{e} to \bar{E} . Yellow-circle = C_{ot} to \bar{E}	64
Figure 4.9:	The trends of $k_{p,position}$ vs. \bar{e} . (a-b) Cases of varying v . (c-d) Cases of varying Re. (Left) panels are from the straight path and (right) from the sinusoidal path. The black dashed lines delineate the borders between the meaningful and trivial solutions	65
Figure 5.1:	An example of a randomly generated swimmer body. The blue line is the body surface and the dots are interpolation points for the Catmull-Rom spline. Muscle actuation is limited to within the active region	68
Figure 5.2:	Sample objective space population distribution for generation 100 of a variable body shape optimization	68
Figure 5.3:	Sample convergence history of the extreme (most optimal) values for each objective in a variable body shape optimization	69
Figure 5.4:	Sample configurations over progressive generations: (a) fastest swimming speed, (b) highest swimming efficiency, and (c) lowest average elastic energy	70

CHAPTER 1

INTRODUCTION

There has been tremendous interest in the development and design of soft robots in recent years, owing to rapid advancement of technology in soft actuators, sensing, and additive manufacturing. Compared to the conventional "rigid" robots, soft robots can take advantage of a large number of degrees of freedom to achieve versatile locomotion and dexterous manipulation as many biological organisms do. These abilities open up the possibility of soft robots that are smaller, lighter, and more efficient than their traditional counterparts [4, 60, 84, 23, 65]. While many promising examples of soft robots have appeared, including soft swimmers emulating rays [74], juvenile jellyfish [70], and eel larvae [15], most soft robots use pneumatic actuation or cable-driven actuation [84], which presents challenges in terms of system complexity, noise, and footprint, among other concerns. Liquid crystal elastomers (LCE), dielectric elastomer (DEA) [15], and shape memory alloy [32], offer the promise of compact, muscle-like actuation for soft robots. These so-called smart materials have attracted growing attention because of the intriguing shape or volume recovery properties under different external stimuli, such as electric, magnetic, thermal, chemical, light and pneumatic [83, 7, 50, 72, 89, 96]. However, understanding of the interplay between soft body and such muscle-like actuation remains limited. In particular, a systematic design tool for soft robotic systems is lacking that accounts for model dynamics and multiple objectives of interest.

Designing soft swimming robots that undergo active deformations in a fluid is considerably challenging. First of all, fast swimming motions are typically resultant from a significant amount of momentum exchange between the fluid and solid structures to overcome viscous drag force in the fluid, which require robots to generate rapid and stable structural deformations reversibly. Meanwhile, efficient locomotion of a deformable object requires the employment of specific swimming patterns (or swimming gaits) to take advantage of thrust forces from the resultant fluid drag and wake structures behind [57], which is critical especially in the small or finite Reynolds number regime where the viscous effect is important [79]. To take all the factors into account, the dynamical

performances of soft robots with various geometries, material properties, as well as the imposed active control schemes, need to be determined jointly with the induced fluid motions. In addition, dynamic instabilities may occur when light-weight structures move in fluid [81, 24], which adds complexities in understanding the control mechanisms of how soft robots perform a stable swimming motion. In general, while various different types of soft robots have been manufactured and tested, it is desired to understand their precise swimming mechanisms, which requires the combination of experimental studies with accurate modeling and simulations in design, analysis, and optimization.

In Chapter 4 we present a novel study on multi-objective optimization of feedback controllers for soft robots based on high-fidelity CFD simulation that explicitly accounts for muscle-like biomimetic actuation. Oftentimes, instead of fully resolving such nonlinear fluid/elastic-structure interactions (FESI), people oversimplify the problem by solving a reduced fluid-solid coupling system in mathematical modeling and numerical simulations. For example, the majority of numerical studies of fish-like swimmers assume that the undulatory motion (or swimming gait) approximately follows a traveling-wave form which can be experimentally measured for a free-swimming biological fish [32, 48, 99]. Typically, one treats the fish body as deformable but prescribes the curvature of its backbone deformation to a certain traveling-wave form [25, 93]. While convenient, these studies may oversimplify the nonlinear FESI to be a (quasi) one-way coupling problem, and, in the meantime, introduce too many free parameters to define the body actuation, which adds significant complexities in designing control schemes later. More importantly, soft swimmers will not always follow a specific swimming gait, which only approximate the solitary swimming motion at a quasi-steady state. In reality, they can constantly switch between straight-swimming and turning motions with acceleration/deceleration, especially when coordinating with many other swimmers during schooling [76, 31, 47].

To model soft actuation materials, an alternative to prescribing the entire body deformation or curvature is to build micro-mechanical models that take into account the intrinsic muscle-like behaviors locally. Generally speaking, there are typically two different ways of modeling the

so-called artificial muscles. One way is to decompose the total deformation of the material into two parts: elastic deformation caused by mechanical stress and active deformation/strain caused by other stimuli [14, 95, 58]. For example, deformation of hydrogel can be decomposed into the elastic part and the swelling part [14]; deformation of liquid crystal elastomer can also be decomposed into the elastic strain and the stimuli-induced strain. Another approach is the active stress method, where the total stress is decomposed into a mechanical part and an active part, both of which can induce deformation [91]. In many cases, the above two methods can be flexibly used in achieving arbitrary deformations. In fact they are mathematically identical, due to the fact that the active deformation introduced here is a first-order approximation of nonlinear elasticity, and is independent of mechanical stress. These two methods have been widely used in modeling active soft elastic structures in biological systems (e.g., cardiovascular mechanics) and synthetic active soft materials [2]. While these elasticity models provide much more flexible yet simple local actuation schemes, solving for the resultant nonlinear deformation is computationally expensive when coupled with another (nonlinear) flow solver. To address these challenges, we have recently implemented the active strain approach in a fictitious domain (FD) method, and demonstrated that the FD/active-strain method is capable of solving the fully-coupled FESI for an arbitrary shape subjected to distributed contractive active strains [58], which is presented in Chapter 3.

When a soft material interacts with fluid flows, the coupling between the fluid force and material elasticity can generate waves propagating at the fluid/solid interface. Understanding this behavior is critical to the study of biological swimmers and their artificial analogs as it can greatly effect the viability and efficiency of a potential swimming mode. The soft materials of which soft robots are made are often viscoelastic with nonlinear behavior. Previous studies suggest that nonlinearity has a destablizing effect on the fluid-elastic solid system thus further amplifying the importance of understanding this behavior [33]. Chapter 2 presents an analytical study of the stability of the interface between a nonlinear, viscoelastic gel film and a Newtonian fluid undergoing Couette flow.

CHAPTER 2

STABILITY OF COUETTE FLOW PAST A GEL FILM

The interaction of viscous fluid and soft objects is of considerable importance in a wide range of problems, such as rheology of complex fluids, coating, biological locomotion, and soft lubrication [108, 90, 29, 87]. Kumaran et al. [51] first studied the stability of an incompressible viscoelastic gel film in a Newtonian Couette flow by ignoring inertia, where a linear model is adopted to describe deformation. They found the fluid/solid interface becomes unstable when the imposed shear goes beyond a certain critical number, and the critical value of the imposed fluid shear strength varies inversely with the film thickness for sufficiently thick solids, which is verified by the following experiments by Kumaran & Muralikrishnan [52, 69]. For sufficiently thin solids, however, the linear elastic model overpredicts the critical values of the fluid shear that drives the interfacial instability. Gkanis & Kumar [33] studied the similar problem by employing a neo-Hookean solid model which admits finite/large deformation. While observing similar behaviors for thick gels, their model predicts a much smaller critical shear for thin gels, which suggests that incorporating solid nonlinearity can effectively destabilize the system. It has been identified that such interfacial instability under shear is mainly due to the first normal-stress difference appearing at the base state solutions, which is known as the Poynting effect in nonlinear solids [78, 64], and is also similar to the situation of two coupled viscoelastic liquids [80, 11]. When surface tension is incorporated into the model, it changes the short-wave instability in thin films to be finite-wavelength. Later Gkanis & Kumar [34] investigated how the flow field and combined pressure gradient impact stability of a neo-Hookean solid.

Although such elastohydrodynamic instability has been studied for simple neo-Hookean solids, in practice soft materials often exhibit more complicated constitutive behaviors than hyperelasticity. Especially for gel-like (e.g., hydrogel) materials that are typically composed of a large amount of solvent such as water and long chain polymers which can form a complex network by chemical crosslinkers such as covalent bond, or physical crosslinkers such as ionic bond or van der waals

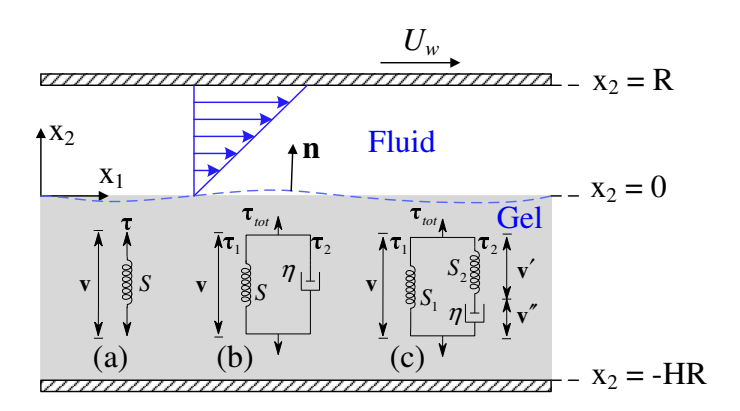


Figure 2.1: Schematic for a Couette flow past a gel film. Nonlinear solid models: (a) neo-Hookean, (b) Kelvin-Voigt, (c) Zener.

interaction. The combined effects of elasticity, viscosity, and surface tension may generate new dynamic behaviors of the material [53], as well as some intriguing interfacial instability phenomena [68, 10, 102].

Here we study stability of an incompressible, impermeable gel film when subjected to a Newtonian Couette flow; see schematic in figure 2.1. We employ an Eulerian representation in both fluid and solid phases, and solve for the velocity, pressure and stress fields simultaneously. Compared to the previous works [51, 33, 34], we examine the contributions from both the viscous effect and the nonlinear elasticity to the fluid/solid interface instability, especially for the thin films where material nonlinearity is manifested.

2.1 Mathematical Model

2.1.1 Constitutive equations

We first derive equivalent "differential" models for the evolution equations of solid stress in an Eulerian frame. In this way, the governing equations in two phases are consistently defined in terms of velocity, pressure and stress [27, 28, 29]. In characterizing material constitutive relations, virtual models of springs and dashpots are often employed to describe the contributions from the elastic and viscous effects, respectively. Different combinations of springs and dashpots can effectively represent complex viscoelastic behaviors as highlighted by the schematics for the three models

(a-c) as shown in figure 2.1. The constitutive relation for the simplest nonlinear hyperelastic solid, i.e., neo-Hookean solid, can be characterized by a linear stress-strain relation

$$\tau_{nh} = S(\boldsymbol{B} - \boldsymbol{I}) \tag{2.1}$$

in a spring, where τ_{nh} is the elastic stress tensor, S is the shear modulus, and

$$\mathbf{B} = \mathbf{F} \cdot \mathbf{F}^T \tag{2.2}$$

is the Finger tensor where F (or index form $F_{ij} = \partial x_i/\partial X_j$) is the deformation gradient tensor serving as a mapping from the initial (X) to the current (x) reference frame. It is straightforward to show that the rate of change of the Finger tensor satisfies

$$\dot{\mathbf{B}} - \mathbf{L} \cdot \mathbf{B} - \mathbf{B} \cdot \mathbf{L}^T = \mathbf{0},\tag{2.3}$$

where

$$\mathbf{L} = \dot{\mathbf{F}} \cdot \mathbf{F}^{-1} = (\nabla \mathbf{v})^T \tag{2.4}$$

(here $L_{i,j} = \partial v_j/\partial x_i$) and dot represents the material time derivative $\dot{B}_{ij} = \partial B_{ij}/\partial t + v_k B_{ij,k}$ [45]. Then the differential form of the neo-Hookean model can be written as [28]:

neo-Hookean:
$$\tau_{nh}^{\nabla} = \dot{\tau}_{nh} - \mathbf{L} \cdot \tau_{nh} - \tau_{nh} \cdot \mathbf{L}^{T} = S(\nabla \mathbf{v} + (\nabla \mathbf{v})^{T}),$$
 (2.5)

where

$$\overset{\nabla}{\tau} = \dot{\tau} - \mathbf{L} \cdot \tau - \tau \cdot \mathbf{L}^T \tag{2.6}$$

is the so called upper-convected time derivative.

To proceed, the simplest viscoelastic solid, a Kelvin-Voigt solid, can be characterized by connecting a spring with a dashpot in parallel. When deformed, each element exerts stress (τ) and undergoes deformation rate (ν) accordingly. The total stress of the element is hence defined by

$$\tau_{tot} = \tau_1 + \tau_2,\tag{2.7}$$

where τ_1 and τ_2 are the stresses in the respective branches. By defining $\tau_1 = \tau_{nh}$ from (2.5) and the viscous stress as

$$\tau_2 = \eta(\nabla v + (\nabla v)^T) \tag{2.8}$$

(η is a solid viscosity), we derive a two-equation model for a Kelvin-Voigt material:

Kelvin-Voigt:
$$\tau_{tot} = \tau_1 + \eta(\nabla v + (\nabla v)^T), \quad \overset{\nabla}{\tau_1} = S(\nabla v + (\nabla v)^T).$$
 (2.9)

However, this model is known to produce reasonable values of creep but incorrectly predicts the behavior of stress relaxation [63], which can be improved by adding a second neo-Hookean spring element (with modulus S_2) in series with the dashpot to provide a Zener model. Note that on the right branch, we need to consider individual velocities associated with the spring v' and the dashpot v'', which are related to the total velocity v through

$$v = v' + v''. \tag{2.10}$$

Therefore, the neo-Hookean stress in the right branch (spring 2) now satisfies

$$\overset{\nabla}{\tau_2} = S_2(\nabla \mathbf{v'} + \nabla \mathbf{v'}^T); \tag{2.11}$$

the viscous stress becomes

$$\tau_2 = \eta(\nabla \mathbf{v''} + \nabla \mathbf{v''}^T). \tag{2.12}$$

Again, by making use of the fact that $\tau_{tot} = \tau_1 + \tau_2$, after some algebra we derived the governing equations for the total stress (τ_{tot}) and the neo-Hookean (τ_1) stress on the left branch (spring 1) in the Zener model:

Zener:
$$\tau_{tot} + \lambda_1 \tau_{tot}^{\nabla} = \tau_1 + \lambda_2 (\nabla v + \nabla v^T), \quad \tau_1^{\nabla} = S_1 (\nabla v + \nabla v^T), \quad (2.13)$$

where $\lambda_1 = \frac{\eta}{S_2}$ and $\lambda_2 = \frac{\eta}{S_2}(S_1 + S_2)$.

2.1.2 Universal Eulerian description

Consider an incompressible Newtonian fluid past a gel film as shown in figure 2.1 with material constitutive relations constructed in Section 2.1.1. The fluid layer with thickness R is bounded by the solid at the bottom and a rigid wall on the top moving with a constant velocity U_w . The solid gel with thickness HR is fixed on a rigid plate. Following Kumaran $et\ al$. [51] and Gkanis &

Kumar [33], we use R as the length scale, neo-Hookean modulus S_1 as the pressure/stress scale, μ_f/S_1 as the time scale, and RS_1/μ_f as the velocity scale. The Reynolds number is then defined by $Re = \rho_f S_1 R^2/\mu_f^2$. We ignore the inertia effect (Re \ll 1), and assume the fluid flow is governed by the Stokes equation. The dimensionless governing equations can be written as:

$$\nabla \cdot \mathbf{v}_f = 0, \quad -\nabla p_f + \nabla^2 \mathbf{v}_f = \mathbf{0}, \tag{2.14}$$

where p_f and v_f are the pressure and the velocity field in the fluid, respectively. The solid is assumed to be incompressible. The conservation of mass and momentum equations are written in the Eulerian frame as:

$$\nabla \cdot \mathbf{v}_{s} = 0, \quad -\nabla p_{s} + \nabla \cdot \tau_{s} = \mathbf{0}, \tag{2.15}$$

where v_s and p_s are the dimensionless solid velocity and pressure, respectively. And τ_s is a total stress tensor. The constitutive equations for the Zener model become

$$\tau_s + \hat{\lambda}_1 \overset{\nabla}{\tau_s} = \tau_{nh} + \hat{\lambda}_2 (\nabla v_s + \nabla v_s^T), \quad \overset{\nabla}{\tau_{nh}} = \nabla v_s + \nabla v_s^T, \tag{2.16}$$

where $\hat{\lambda}_1 = \frac{S_1}{S_2} \frac{\eta_s}{\mu_f}$ and $\hat{\lambda}_2 = \left(\frac{S_1 + S_2}{S_2}\right) \frac{\eta_s}{\mu_f}$ respectively represent the relaxation and viscous effects, and τ_{nh} represents the dimensionless neo-Hookean stress. Note that $\hat{\lambda}_1$ and $\hat{\lambda}_2$ are related to each other by $\hat{\lambda}_2 = \hat{\lambda}_1 + \eta_s/\mu_f$, and hence $\hat{\lambda}_1 < \hat{\lambda}_2$. Furthermore, in the limit $\hat{\lambda}_1 \to \hat{\lambda}_2 = \lambda$, it is easy to show that the above equations reduce to

$$\lambda(\tau_s - \tau_{nh})^{\nabla} + (\tau_s - \tau_{nh}) = \mathbf{0}, \tag{2.17}$$

or in the Lagrangian frame,

$$\lambda \frac{d}{dt} \left[\mathbf{F}^{-1} \cdot (\tau_s - \tau_{nh}) \cdot \mathbf{F}^{-T} \right] + \left[\mathbf{F}^{-1} \cdot (\tau_s - \tau_{nh}) \cdot \mathbf{F}^{-T} \right] = \mathbf{0}. \tag{2.18}$$

When there is no pre-stress applied on the gel, it is trivial to show that $\tau_s = \tau_{nh}$, i.e., reduction from the full Zener model to the neo-Hookean model. Therefore, the neo-Hookean model ($\hat{\lambda}_1 = \hat{\lambda}_2 = 0$) and the Kelvin-Voigt model ($\hat{\lambda}_1 = 0$, $\hat{\lambda}_2 \neq 0$) appear to be the two asymptotic limits of the Zener model.

To supplement the governing equations with boundary conditions, we assume periodicity in x_1 -direction, and apply no-slip conditions on the top (moving) and bottom (stationary) rigid walls. The dimensionless wall velocity is $\mathbf{v}_f = G\hat{\mathbf{e}}_1$ at $x_2 = 1$, where $G = \mu_f U_w/RS_1$ characterises the strength of the applied shear flow field on the solid. At the fluid/solid interface, the velocity and traction are continuous:

$$\mathbf{v}_f = \mathbf{v}_s, \quad \sigma_f \cdot \mathbf{n} + T \kappa \mathbf{n} = \sigma_s \cdot \mathbf{n},$$
 (2.19)

where n is the normal vector to the interface, T is the dimensionless surface tension scaled by S_1R and κ is the curvature of the interface scaled by R^{-1} . The Eulerian models derived above are equivalent to the conventional Lagrangian models which typically solve for the displacement field, and simplify the mathematical treatment of the fluid-solid coupling at the interface to permit a more straightforward implementation of the velocity and traction continuity conditions [27].

2.2 Linear Stability Analysis

2.2.1 Base state

To perform a linear stability analysis, we need to derive the base-state solutions when the interface is flat. The steady-state velocity solution in the fluid is simply a planar Couette flow $\mathbf{v}_f = (v_1, v_2) = (Gx_2, 0)$, and the fluid stress is given by

$$\sigma_f = -p_f \mathbf{I} + \tau_f = \begin{pmatrix} -p_f & G \\ G & -p_f \end{pmatrix}. \tag{2.20}$$

In the solid, the base-state solutions can be derived by solving the initial transient dynamics during which a fully developed shear flow start exerting on the gel. For the neo-Hookean model ($\tau_s = \tau_{nh}$), the (symmetric) total stress tensor in the solid is defined as

$$\sigma_s = -p_s \mathbf{I} + \tau_{nh} = \begin{pmatrix} -p_s + \tau_{11}^{nh} & \tau_{12}^{nh} \\ \tau_{12}^{nh} & -p_s + \tau_{22}^{nh} \end{pmatrix}. \tag{2.21}$$

It is also reasonable to assume that during the initial transient, the induced velocity field is unidirectional, i.e., $\partial/\partial x_1 = 0$ and $v_s = (v_1(x_2), 0)$. Then the constitutive equations in (2.16) reduce

to

$$\frac{\partial \tau_{11}^{nh}}{\partial t} = 2\tau_{12}^{nh} \frac{\partial v_1}{\partial x_2}, \quad \frac{\partial \tau_{12}^{nh}}{\partial t} = \frac{\partial v_1}{\partial x_2}, \quad \frac{\partial \tau_{22}^{nh}}{\partial t} = 0. \tag{2.22}$$

When there is no pre-stress in the solid, i.e. $\tau_{ij}^{nh} = 0$ at t = 0, it is apparent that $\tau_{22}^{nh} = 0$. Next, integrating both sides of the remaining two stress equations leads to

$$\tau_{12}^{nh} = \int_0^t \frac{\partial v_1}{\partial x_2} dt = \frac{\partial u_1}{\partial x_2} = G, \quad \tau_{11}^{nh} = 2 \int_0^t \tau_{12}^{nh} \frac{\partial v_1}{\partial x_2} dt = \int_0^t \frac{\partial \left(\tau_{12}^{nh}\right)^2}{\partial t} dt = G^2. \tag{2.23}$$

where $u_1 = \int_0^t v_1 dt$ is the displacement. Thus the total stress tensor at equilibrium reads

$$\tau_{nh} = \begin{pmatrix} \tau_{11}^{nh} & \tau_{12}^{nh} \\ \tau_{12}^{nh} & \tau_{22}^{nh} \end{pmatrix} = \begin{pmatrix} G^2 & G \\ G & 0 \end{pmatrix}. \tag{2.24}$$

In the Kelvin-Voigt model and the Zener model, since $v_s = \mathbf{0}$ at equilibrium, equation (2.24) also serves as the base-state solution for the three solid models. Therefore, the base-state total stress can be written as

$$\sigma_s = -p_s \mathbf{I} + \tau_s = \begin{pmatrix} -p_s + G^2 & G \\ G & -p_s \end{pmatrix}. \tag{2.25}$$

Note that a first normal stress difference appears, i.e., $\tau_{11}^s - \tau_{22}^s = G^2$. At the flat interface (i.e., n = (0,1)), equations (2.19) reduce to $\sigma_f \cdot n = \sigma_s \cdot n$ and $p_f = p_s$.

2.2.2 Normal modes and interfacial conditions

A standard linear stability analysis is employed to study the growth of disturbances [9]. All physical disturbance variables f' can be expanded with respect to normal modes

$$f'(x_1, x_2, t) = \tilde{f}(x_2) \exp(ikx_1 + \alpha t), \tag{2.26}$$

where \tilde{f} is the complex-valued amplitude functions, k is the wavenumber, and α is the complex-valued growth rate. The governing equations in (2.14)-(2.16) are linearized, and then transformed into the Fourier space for the disturbances of $(\tilde{\mathbf{v}}_f, \tilde{p}_f)$ in fluid and $(\tilde{\mathbf{v}}_s, \tilde{p}_s, \tilde{\tau}_s, \tilde{\tau}_{nh})$ in solid. After

some algebra, we are able to derive two fourth-order ordinary differential equations for the vertical velocity components \tilde{v}_2^f and \tilde{v}_2^s which admit the following general solutions:

$$\tilde{v}_2^f = A_1 \exp(kx_2) + A_2 \exp(-kx_2) + A_3 x_2 \exp(kx_2) + A_4 x_2 \exp(-kx_2), \tag{2.27}$$

$$\tilde{v}_2^s = B_1 \exp(kx_2) + B_2 \exp(-kx_2) + B_3 \exp(\xi_1 x_2) + B_4 \exp(\xi_2 x_2), \tag{2.28}$$

where

$$\xi_{1,2} = \frac{-\mathrm{i}Gk\left(1 + \alpha\hat{\lambda}_1\right) \pm k\sqrt{-G^2\alpha\left(1 + \alpha\hat{\lambda}_1\right)\left(\hat{\lambda}_1 - \hat{\lambda}_2\right) + \left(1 + \alpha\hat{\lambda}_2\right)^2}}{1 + \alpha\hat{\lambda}_2},\tag{2.29}$$

 A_i and B_i (i=1,2,3,4) are eight unknown coefficients, four of which can be eliminated by boundary conditions at the two walls. For the neo-Hookean solid, we obtain $\xi_{1,2} = (-iG \pm 1) k$ independent of α , and again, recover the solutions obtained by Gkanis & Kumar [33].

The two solutions above are coupled through the kinematic condition

$$\frac{\partial \delta}{\partial t} + v_1 \frac{\partial \delta}{\partial x_1} = v_2, \tag{2.30}$$

imposed at the perturbed interface $x_2 = \delta(x_1)$ where $|\delta| \ll 1$. It can be further linearized as $\frac{\partial \delta}{\partial t} = v_2'$ around the flat plane at $x_2 = 0$, and v_2' is the fluid (or solid) velocity disturbance. The velocity and traction continuity conditions lead to

$$v_1'^f + G\delta = v_1'^s, (2.31)$$

$$v_2^{\prime f} = v_2^{\prime s}, (2.32)$$

$$\frac{\partial v_1'^f}{\partial x_2} + \frac{\partial v_2'^f}{\partial x_1} + G^2 \frac{\partial \delta}{\partial x_1} = \tau_{12}', \tag{2.33}$$

$$-p_f' + 2\frac{\partial v_2'^f}{\partial x_2} + T\frac{\partial^2 \delta}{\partial x_1^2} = -p_s' + \tau_{22}'. \tag{2.34}$$

The first normal stress difference from the base state (G^2) now appears at the left-hand-side of (2.33). The above equations are transformed using the normal modes to the Fourier space where we solve the growth rate α numerically for given values of $H, k, T, G, \hat{\lambda}_1$, and $\hat{\lambda}_2$.

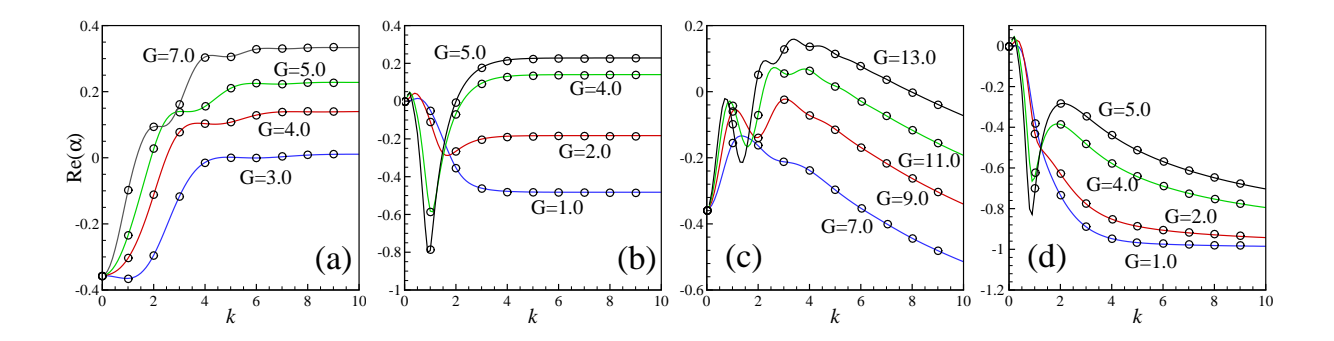


Figure 2.2: The growth rate $Re(\alpha)$ as a function of k for the neo-Hookean solid: (a) H = 0.4, T = 0; (b) H = 4.0, T = 0; (c) H = 0.4, T = 10; (d) H = 4.0, T = 10. The open circles are the results obtained by Gkanis & Kumar [33].

2.3 Results

2.3.1 Growth Rate

In figure 2.2, we show the real part of the growth rate of disturbance, $Re(\alpha)$, by varying thickness ratio (H), surface tension (T), and applied shear strength (G). When there is no surface tension at the interface (T=0), for a thin solid (H=0.4, panel(a)), $Re(\alpha)$ reaches a plateau at high wavenumber asymptotically, indicating a short wave instability. For a relatively thick film (H=4.0, panel(b)), the maximum growth rate occurs at a finite k, hence indicating a finite-wavelength instability. Panels(c) and (d) show $Re(\alpha)$ as a function of k when surface tension is included, and chosen as T=10. In both cases, the surface tension can effectively eliminate instability growth at high wavenumber. The obtained growth rates of the neo-Hookean model are identical to those obtained by Gkanis & Kumar [33].

Although the instabilities in panels(b)-(d) all appear to be finite-wavelength, their profiles are very different, leading to distinctive features shown later in the corresponding marginal-stability curves. In panel(b) where T=0, while instability is induced at finite k and then more and more enhanced as the applied fluid shear G increases, the short-wave feature still remains as $Re(\alpha)$ saturates at large k. In panels(c) and (d) when $T \neq 0$, there are typically two separated regimes of peaks visible: One occurs at small k, and the other occurs at relatively large k. It is seen that

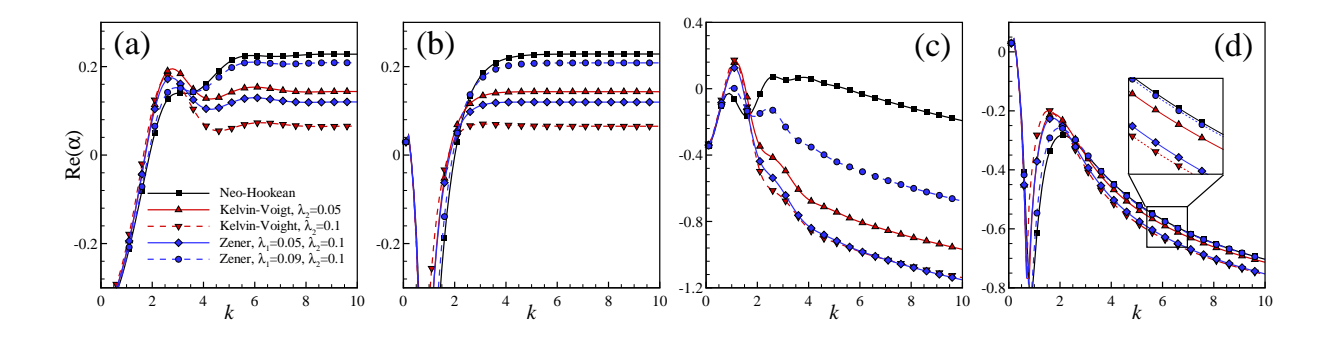


Figure 2.3: Comparison of the growth rate $Re(\alpha)$ as a function of k for the neo-Hookean, Kelvin-Voigt, and Zener solids: (a) H = 0.4, T = 0, G = 5; (b) H = 4.0, T = 0, G = 5; (c) H = 0.4, T = 10, G = 11; (d) H = 4.0, T = 10, G = 5.

with surface tension, the disturbance grows much faster at finite/large k regimes as G increases. Conversely, for thick films, instabilities appear to be more strengthened at small k.

Next, we consider the two viscoelastic models and make comparisons with the neo-Hookean model. The five cases presented in figure 2.3 follow a progression from the basic neo-Hookean model (black) to the Kelvin-Voigt model (red), and then to a full Zener model (blue). In the Kelvin-Voigt model where $\hat{\lambda}_1 = 0$ and $\hat{\lambda}_2 \neq 0$, again, we find that increasing the effective solid viscosity (i.e., increasing $\hat{\lambda}_2$) suppresses instability at large k in both thin and thick gels, which makes the finite-wavelength instabilities dominate. On the other hand, in panels(a,c) we also observe that the instabilities are enhanced at finite wavenumbers to form local maximum for thin gels.

To examine the relaxation effect in the Zener model, we fix $\hat{\lambda}_2 = 0.1$ and vary the dimensionless relaxation time $\hat{\lambda}_1$. We observe that increasing $\hat{\lambda}_1$ shifts $\text{Re}(\alpha)$ upwards. As $\hat{\lambda}_1$ approaches $\hat{\lambda}_2$, this effect becomes increasingly pronounced and the curve gradually returns to that of the neo-Hookean model, consistent with the analytical predictions as $\hat{\lambda}_1 \to \hat{\lambda}_2$ in Section 2.1.2.

2.3.2 Mechanism

As noted by Gkanis & Kumar [33, 34], the interfacial instability in the neo-Hookean solid is due to the coupling of the first normal stress difference and the surface fluctuation δ appearing in the interfacial condition. Here we adopt their explanation by considering a sinusoidal surface

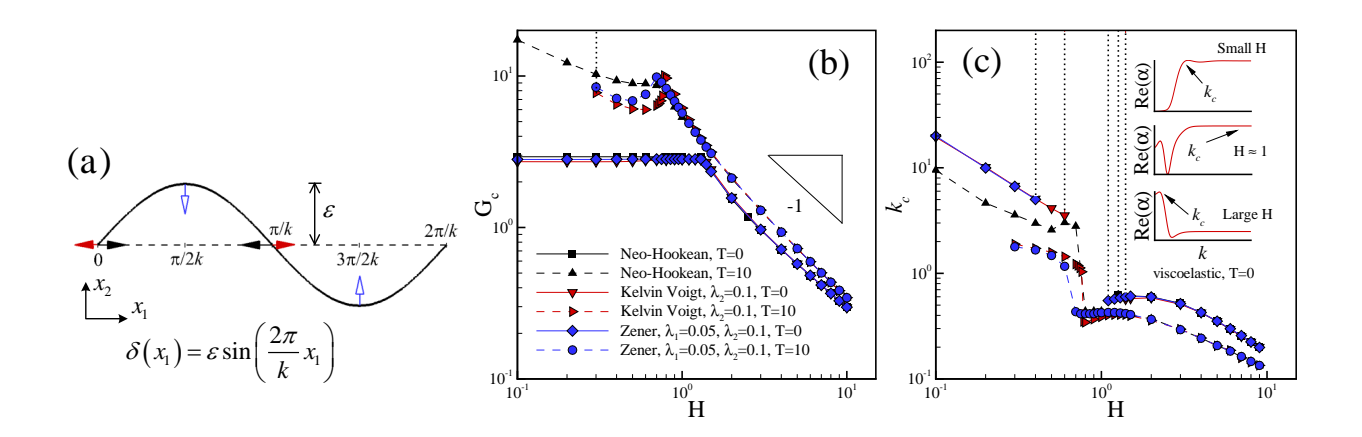


Figure 2.4: (a) Schematic for a sinusoidal surface perturbation. The contributions of the first normal-stress difference and the solid viscous effect are marked by the black and red solid arrows, respectively. The open arrows represent the stabilizing effect due to surface tension. (b,c): Critical values of the imposed strain G_c and the critical wavenumber k_c as a function of H. The black dotted lines are drawn at the locations where either G_c or k_c tends to infinity. Inset in (c): Growth-rate curves near $H \approx 1$ where short-wave instabilities recur.

perturbation $\delta = \varepsilon \sin\left(\frac{2\pi}{k}x_1\right)$ as shown in the schematic in figure 2.4(a). The traction continuity condition in (2.33) essentially suggests the coupling term $G^2\delta_{x_1}$ has a 90° phase lag compared to velocity (and shape δ) fluctuations in (2.31), which tends to compress the wave crests and extend the valleys (marked by the black solid arrows), and hence destabilize the interface.

To understand the solid viscous effects in the Kelvin-Voigt model, we rewrite the shear stress component in equation (2.33) in the Fourier space as:

$$\tilde{\tau}_{12}^{elast} - \tilde{\tau}_{12}^{f} = G^{2} \tilde{\delta}_{x_{1}} - \tilde{\tau}_{12}^{vis} = \left[G^{2} - \alpha \hat{\lambda}_{2} \left(\frac{D^{2}}{k^{2}} + 1 \right) \right] \tilde{\delta}_{x_{1}}. \tag{2.35}$$

In the above we split the solid stress τ_s into the contributions from the hyperelastic (due to the neo-Hookean elasticity, and denoted by "elast") and viscous (due to the viscous term in the Kelvin-Voigt model, and denoted by "vis") effects. It is clearly seen that on the right-hand-side, as $k \to \infty$ the viscous term provides an asymptotic limit $-\alpha \hat{\lambda}_2$ acting against the first coupling term due to the normal stress difference. As illustrated by the red arrows in figure 2.4(a), this relaxes the pinching effect at large k to stabilize the surface though its behavior at small k is somewhat complex. A similar argument can be made based on the traction balance in the normal direction when examining

the surface tension effect. Following the same procedure we rewrite equation (2.34) as

$$\tilde{\sigma}_{22}^{elast} - \tilde{\sigma}_{22}^{f} = T\tilde{\delta}_{x_1x_1} - \tilde{\sigma}_{22}^{vis} = \left(T + 2\alpha\hat{\lambda}_2 \frac{D}{k^2}\right)\tilde{\delta}_{x_1x_1}. \tag{2.36}$$

The second derivative on δ results in a 180° phase shift so there is a normal force acting to restore the perturbed interface. Note that the right-hand-side of (2.36) can be written as $\left(-k^2T - 2\alpha\hat{\lambda}_2D\right)\tilde{\delta}$, suggesting that the contribution from the surface tension is scaled by k^2 , and hence the inclusion of surface tension causes a significant damping effect to suppress disturbance growth, especially at large k [51, 33].

2.3.3 Marginal Instability

We show the marginal stability curves for the critical shear stress G_c (figure 2.4(b)) and the corresponding critical wavenumber k_c (figure 2.4(c)) as functions of the film thickness ratio H. One obvious observation is that as H becomes large, all the models produce almost the same results as the linear elastic model [51] due to smaller deformation. We also observe that the marginal stability curves of the Zener model again vary between those of the neo-Hookean model and the Kelvin-Voigt model.

In panel(b) when surface tension is lacking, the three models in fact predict very similar values of G_c , suggesting that adding viscous effects to the solid does not necessarily stabilize the interface. In contrast, the finite-wavelength instabilities observed in figure 2.3(a) and (b) for the Kelvin-Voigt model may even cause a slight reduction in G_c , making the interface even more unstable under shear. The critical stresses for thin films are found to be around 2.93 while vary inversely with H for thick films, with transitions occurring for films with finite thickness ($H \approx 1$).

Adding surface tension effectively stabilizes the interface for all values of H, and yields finite-wavelength instabilities. Compared to the neo-Hookean model, the solid viscous effects significantly change the critical values for thin films, leading to yet more complex behaviors. When H is sufficiently small, we first identify a narrow regime where the system is stable to the fluid shear, i.e., $G_c \to \infty$ (marked by black dotted lines). At relatively large H, finite-wavelength instabili-

ties appear, and predict lower critical values than the neo-Hookean case. As H further increases close to the transition regime, G_c rises again in both the Kelvin-Voigt and Zener models, up to maximum values around H=0.7. Such non-monotonic behaviors are due to the amplification (suppression) of instability in the viscoelastic films at small (large) k as discussed in figure 2.3(c), which correspondingly picks relatively low (high) critical values of G_c for thin (thick) films.

While the G_c-H curves are very similar, the marginal curves of k_c in panel(c) exhibit distinctive features between the three models at T=0. At small thickness, the finite-wavelength instabilities in the two viscoelastic models are visible by the critical values of k_c beyond the stable regime; while $k_c \to \infty$ for the neo-Hookean solid due to its short-wave nature. Interestingly, we observe that in both the Kelvin-Voigt and Zener models, discontinuities of k_c occur near the transition regimes when $H \approx 0.7$, in accordance with the peaks in panel(b). As illustrated by the growth-rate curves in the inset of panel(c), in the transition regimes, increasing film thickness H drives a secondary finite-wavelength instability arising at small wavenumber. As the growth-rate maximum shifts from large towards small k, short-wave instabilities may recur, and hence k_c saturates at infinity, resembling those observed in the thin neo-Hookean films in figure 2.2. Moreover, inclusion of surface tension effectively reduces k_c as shown in the lower branch of marginal curves in panel(c). Also a stable regime at small H is identified for viscoelastic gels in accordance with panel(b) where G_c tends to infinity, and then finite-wavelength instabilities dominate as H increases.

2.4 Concluding Remarks

In this work, we investigate the interfacial stability of a soft gel film when subjected to a Newtonian Couette flow at zero Reynolds number. We have constructed three differential models for the solid stress including the neo-Hookean, Kelvin-Voigt, and Zener models, and solve for the velocity, pressure and stress fields in both fluid and solid phases simultaneously in the Eulerian frame. We have performed linear stability analysis to study the interfacial instability by exploring the parameter spaces, and compared the critical behaviors of the three solid models. We focus our attention in the thin-film regime where the material nonlinearity is pronounced; while for

sufficiently thick films, all the models produce very similar results as those predicted by linear models due to small deformation. We find the interfacial instability is driven by the first-normal stress difference in the base-state solution in the solid phase. Compared with the neo-Hookean model, inclusion of solid viscous effects leads to finite-wavelength instabilities in both thin and thick films, although we still observe short-wave instabilities recur in a narrow transition regime at finite film thickness. When surface tension is included, the fluid/solid interface becomes more stable, and finite-wavelength instabilities are found to dominate in all models. In addition, for viscoelastic gels we have observed stable regimes for sufficiently thin films, as well as intriguing non-monotonic features on the marginal stability curves near the transition regimes where the film thickness is finite.

It is interesting to observe that when surface tension is negligible, the critical values of the applied shear strength ($G_c \approx 2.93$) seem to be well-characterized by the neo-Hookean model, i.e., material's hyperelasticity. Further analysis reveals that the results obtained above can be directly extended to more general hyperelastic Mooney-Rivlin model which is used for constitutive relations in a wide range of materials. Recall the constitutive equation for a Mooney-Rivlin solid is given as

$$\tau_s = g_1 \mathbf{B} + g_2 \mathbf{B}^{-1}, \tag{2.37}$$

where g_1 and g_2 are scalar functions of the invariants of \mathbf{B} [59]. Thus the neo-Hookean model is a special case of the Mooney-Rivlin model by choosing $g_1 = 1$ and $g_2 = 0$. It is easy to show that \mathbf{B}^{-1} satisfies a lower-convected derivative:

$$\dot{\mathbf{B}}^{-1} + \mathbf{L}^T \mathbf{B}^{-1} + \mathbf{B}^{-1} \mathbf{L} = \mathbf{0}$$
 (2.38)

[45]. Following the same procedure in Section 2.2, we find that a lower-convected model for the elastic stress $\tau_s \propto I - B^{-1}$ yields the base-state solutions

$$\sigma_s = \begin{pmatrix} -p_s & G \\ G & -p_s - G^2 \end{pmatrix}$$
 (2.39)

and

$$p_f = p_s + G^2, (2.40)$$

which lead to identical stability analysis results as the neo-Hookean model where $\tau_S \propto B - I$. Hence the Mooney-Rivlin model will generate the same results as the neo-Hookean model as well. With this study, it is straightforward to construct more elaborated solid models (e.g., poroelasticity), and apply similar methodologies to investigate their stabilities when coupled with fluid flows. It is also desired to perform direct simulations to resolve new physics and phenomena associated with nonlinear deformations in fluid/elastic-structure interactions.

CHAPTER 3

A FLUID–STRUCTURE INTERACTION STUDY OF SOFT ROBOTIC SWIMMER USING A FICTITIOUS DOMAIN/ACTIVE-STRAIN METHOD

In the past decades, numerous computational methods have been developed to simulate interactions between fluid and moving elastic objects. One example is the so-called boundary conforming method, such as the Arbitrary Lagrangian-Eulerian (ALE) finite element method [40, 27] and the space-time finite element method [62]. In these methods, the governing equations of both the fluid and solid phases are solved on one set of mesh that is adapted to the deforming solid objects or geometric boundaries. Although the sharp-interface methods can accurately resolve the complex geometries of moving boundaries, the computation cost is high, especially in 3D. This is because for the strongly coupled fluid-elastic system, additional subiterations between the fluid and solid solvers are necessary in order to achieve better convergence [46, 92]. Moreover, frequent re-meshing might be necessary in order to follow boundary movement. When the moving-mesh technique is employed (e.g., ALE method), the associated mesh velocities have to be solved as additional unknowns together with the variables in the fluid and solid phases [40, 27]. In addition, unstructured meshes (e.g., triangular, quadrilateral, etc.) are often employed in these methods, which adds complexities in parallelization.

Instead of employing body-fitted meshes, the so-called Cartesian grid methods typically use either separate or non-boundary fitted meshes. This approach simplifies the initial mesh generation and avoids the need for moving and/or adaptive meshing to resolve the changing interface which reduces the overall cost and complexity. For example, the immersed boundary method employs overlaid Eulerian and Lagrangian meshes to solve fluid/elastic structure interactions: The Navier-Stokes (N-S) equations are solved on a fixed Eulerian mesh; while the embedded boundaries are tracked by a set of freely moving Lagrangian points. To account for the no-slip conditions at fluid-solid interfaces, appropriate forcing density terms are added to the N-S equations by using proper interpolations between the solution variables at the fixed grid points in the vicinity of the

moving boundary and the nearest Lagrangian points [49, 77, 67, 66, 6, 94]. Instead of solving the N-S equations in the fluid phase, both the particle-based methods (e.g., Smoothed Particle Hydrodynamics (SPH) method [3]) and the kinetic methods (e.g., Lattice Boltzmann method (LBM) [37, 13, 30, 41, 42]) can be flexibly combined with the immersed boundary method to handle complex geometries, and has become more and more popular in dealing with fluid-structure interactions (FSI).

Inspired by the recent experimental designs [70, 74], in this chapter we numerically study the swimming motion of soft robotic swimmers that perform large reversible elastic deformations driven by the imposed actuation. We assume that the elastic material is hyper-elastic, and can be described by the neo-Hookean constitutive relation that permits finite/large nonlinear deformations. To model the muscle-like behaviors, we adopt an active strain model to distribute contracting strains on soft elastica, which is then coupled with the fictitious domain (FD) method [104, 105] to resolve the FSIs. The central idea of the active strain model is based on the multiplicative decomposition where the (total) deformation gradient tensor is split into two parts that represent the sequential contributions from the imposed contractions and the elastic response of the material [54, 55]. It is different from the so-called active stress approaches where an additional stress term (different from applied mechanical stress) is introduced into the material model [2]. By appropriately applying contracting strains on elastic plates of different (e.g., square, circular, or bell-like) shapes and rigidities, we show that soft robot prototypes of simple geometries can effectively perform undulatory or jet-propulsion swimming motions.

3.1 Mathematical Model and Numerical Method

3.1.1 Hill's Muscle Model

The three element Hill's muscle model is the standard basis for modeling the mechanical behavior of skeletal muscle [39, 61]. In its original form it is a 1D model composed of two nonlinear springs and a contractile element. The contractile element (CE) is arranged in series with one spring and both of which are in parallel with another spring. Generally speaking, the series spring (SE) models

the elastic behavior of the active components of the muscle while the parallel spring models the passive elastic behavior, even while the contractile element is inactive. The contractile element is the active part of the muscle that contracts while activated and typically is freely extensible while not.

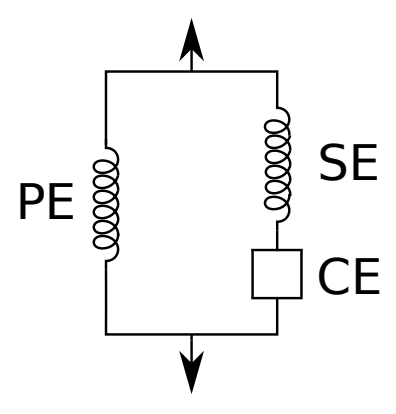


Figure 3.1: Schematic of the 1D three element Hill's muscle model. It is composed of a contractile element (CE) in series with a nonlinear spring (SE) which are both in parallel with another nonlinear spring (PE).

Many variations exist and for our study we find that a two element model, excluding the parallel spring element, can model the types of active materials that we are investigating. These materials tend to be uniform in nature so we expect the elastic behavior to be reasonably defined by a single element. As opposed to biological muscle which may be composed of many smaller structures and materials.

3.1.2 Active Strain Method

To begin with, we seek mathematical models that describe the nonlinear mechanics of soft actuating material. Generally speaking, there are typically two different ways of modelling soft actuating material or so-called artificial muscle. One way is decomposing the total deformation of the material into two parts: elastic deformation caused by mechanical stress and active deformation/strain caused by other stimuli such as light, electric field, thermal field etc. For example, deformation of hydrogel can be decomposed to the elastic part and swelling part [14]; deformation of liquid crystal elastomer can also be decomposed to the elastic strain and stimuli-induced strain. In experiments, active strain

can be easily measured. Without any mechanical load, deformation of a free-standing soft material can be measured as a function of the intensity of external stimuli [95]. Here we employ an active strain approach which applies principal contractions in a manner similar to artificial muscle. To apply actuation the deformation gradient tensor \mathbf{F} is decomposed into an active deformation tensor \mathbf{F}_a and an elastic deformation tensor \mathbf{F}_e following multiplicative decomposition [54, 55] such that

$$\mathbf{F} = \mathbf{F}_e \cdot \mathbf{F}_a. \tag{3.1}$$

Here \mathbf{F}_a is effectively an arbitrary function applied to the reference configuration that can be designed in terms of the desired location, direction, sign and strength. For incompressible solids that are considered here, we apply an incompressible restriction on actuation such that $det(\mathbf{F}) = 1$. For simplicity \mathbf{F}_a can be defined in the principal coordinates and transformed to the desired orientation by a standard solid body rotation coordinate transformation. For an artificial muscle that contracts uniaxially when activated, we define $\mathbf{F}_a = \text{diag}[\lambda_1, \lambda_2, \lambda_3]$ where $\lambda_1 < 1$ represents a principal stretch, and $\lambda_2 = \lambda_3 = \sqrt{\lambda_1^{-1}} > 1$ are the correspondingly strains in the other two directions. With total \mathbf{F} being mapped appropriately, the resultant elastic stress can be calculated through the constitutive relation $\tau = \tau(\mathbf{F}_e) = \tau\left(\mathbf{F} \cdot \mathbf{F}_a^{-1}\right)$ for various different kinds of materials (hyperelastic, viscoelastic, composite, etc.). In this study, we assume the active strain tensor to be either a constant or time-dependent. Nevertheless, it is important to mention that the active strain of real muscle can also depend on its loading condition. Therefore, to better characterize the behaviors of artificial muscles (e.g., electroactive polymer or liquid crystal elastomer) under actuation, systematic experimental measurements are required to obtain the relationship between the active strain tensor and the imposed loading conditions.

Alternatively, another widely used approach is the active stress method where the total stress is decomposed into a mechanical part and an active part, and both of which can induce deformation. For instance, Maxwell stress is usually introduced in the constitutive models of dielectric elastomer [91]. In many cases, the above two methods are mathematically identical, due to the fact that the active deformation introduced here is a first order approximation of nonlinear elasticity, and is independent of mechanical stress. There are also other approaches to implement (soft) actuation

without using stress or strain decompositions. For example, to mimic swimming motions of slender flexible swimmers such as sperms or nematodes using the immersed boundary method, active forces are directly added to the right-hand-side of the N-S equation by taking the variational derivative of the discrete elastic energy that is constructed based on the targeted local stretches and curvatures [25, 93].

3.1.3 Distributed Lagrange Multiplier/Fictitious Domain Method (DLM/FD)

3.1.3.1 Formulation

To resolve the FSI of soft robotic swimmers, we implement the above active strain model in a fictitious domain (FD) method proposed by Yu [104], who extended the FD formulation of Glowinski *et al.* [35] for the rigid particles to the case of flexible bodies. The key idea of the FD method is that the interior of the solid is assumed to be filled with a fictitious fluid that is constrained to move at the same velocity with the solid by a pseudo body force (i.e. Lagrange multiplier). The advantage of the FD method is that the flow fields can be solved efficiently with a fixed Cartesian grid. The reader is referred to [104] for the details on the derivation of the FD formulation and the numerical schemes.

In the following, we briefly introduce the formulation and the numerical schemes of the FD method. Suppose that a deformable body of density ρ_s is immersed in the incompressible Newtonian fluid of viscosity μ and density ρ_f . Let Ω denote the entire computational domain containing both solid and fluid domains, and P(t) represent the solid domain. It is noted that tracking swimming objects in the fixed coordinates requires using a very large computational domain, which makes computation very expensive especially in 3D. Alternatively, here we employ an instantaneous inertial frame Ω that co-moves with the swimmer at a certain reference speed U [56]. Then the dimensionless FD governing equations in weak form for the incompressible Newtonian fluid in the co-moving relative references as

$$\int_{\Omega} \left(\frac{\partial \mathbf{u}_f}{\partial t} + \hat{\mathbf{u}}_f \cdot \nabla \mathbf{u}_f \right) \cdot \mathbf{v}_f d\mathbf{x} + \int_{\Omega} \left(-p\mathbf{I} + \frac{1}{\text{Re}} (\nabla \mathbf{u}_f)^T \right) : \nabla \mathbf{v}_f d\mathbf{x} = \int_P \lambda \cdot \mathbf{v}_f d\mathbf{x}, \tag{3.2}$$

$$\int_{\Omega} q \nabla \cdot \mathbf{u}_f d\mathbf{x} = \mathbf{0},\tag{3.3}$$

where $\hat{\mathbf{u}}_f = \mathbf{u}_f - \mathbf{U}$. The dimensionless governing equations for neo-Hookean solid material $(\tau = G(\mathbf{B} - \mathbf{I}))$ are solved in the absolute references as

$$\int_{P} \left[(\rho_{r} - 1) \left(\frac{d\mathbf{u}_{s}}{dt} - Fr \frac{\mathbf{g}}{g} \right) \right] \cdot \mathbf{v}_{s} d\mathbf{x} + \int_{P} (\nabla \mathbf{v}_{s})^{T} : \left[\lambda_{0} \ln J \mathbf{I} + G(\mathbf{B} - \mathbf{I}) \right] d\mathbf{x} - \int_{P} (\nabla \mathbf{v}_{s})^{T} : \left(-p \mathbf{I} + \frac{1}{\text{Re}} \left[\nabla \mathbf{u}_{f} + (\nabla \mathbf{u}_{f})^{T} \right] \right) d\mathbf{x} = - \int_{P} \lambda \cdot \mathbf{v}_{s} d\mathbf{x}, \tag{3.4}$$

$$\int_{P} (\mathbf{u}_f - \mathbf{u}_s) \cdot \zeta d\mathbf{x} = \mathbf{0} \tag{3.5}$$

Equations (4.3)-(4.6) represent the fluid momentum equation, the fluid continuity equation, the solid momentum equation, and the velocity constraint in the solid domain, respectively. In these equations, \mathbf{u}_f is the fluid velocity, \mathbf{u}_s the solid velocity, p the fluid pressure, and λ the pseudo bodyforce (i.e., the Lagrange multiplier). \mathbf{v}_f , \mathbf{v}_s , q and ζ are the corresponding variations, respectively. For the original FD method for the passive deformation model, $\mathbf{B} = \mathbf{F} \cdot \mathbf{F}^T$ is the left Cauchy-Green deformation tensor, here \mathbf{F} being the deformation gradient tensor defined as: $\mathbf{F} = \partial \mathbf{x}/\partial \mathbf{X}$, in which \mathbf{x} and \mathbf{X} are the solid current and reference configurations, respectively. J is the determinant of \mathbf{F} , and J = 1 for the incompressible solid. In contrast, for the active strain model studied,

$$\mathbf{B} = \mathbf{F}_e \cdot \mathbf{F}_e^T = (\mathbf{F} \cdot \mathbf{F}_a^{-1}) \cdot (\mathbf{F} \cdot \mathbf{F}_a^{-1})^T, \tag{3.6}$$

where \mathbf{F}_e is the elastic deformation tensor which causes the elastic stress, and \mathbf{F}_a is an input deformation tensor without generating elastic stress. Also \mathbf{g} denotes the gravitational acceleration. The following characteristic scales are used for the non-dimensionlization scheme: L_c for length, U_c for velocity, L_c/U_c for time, $\rho_f U_c^2$ for pressure p, and $\rho_f U_c^2/L_c$ for Lagrange multiplier λ . The following dimensionless control parameters are also introduced:

Density ratio :
$$\rho_r = \frac{\rho_s}{\rho_f}$$

Material parameters : $\lambda_0 = \frac{\overline{\lambda_0}}{\rho_f U_c^2}$, $G = \frac{\overline{G}}{\rho_f U_c^2}$

Reynolds number : $\text{Re} = \frac{\rho_f U_c L_c}{\mu}$

Froude number : $Fr = \frac{gL_c}{U^2}$ (3.7)

where g is the gravity constant, $\overline{\lambda}_0$ is related to the compressibility property of the material and \overline{G} represents the shear modulus. It should be mentioned that for robotic swimmers, the characteristic velocity is defined as $U_c = f_c L_c$ where a reference actuation frequency is chosen as $f_c = 1Hz$. In addition, in order to enforce the incompressibility constraint of the solid material, i.e., J = 1, we impose a penalty function-like approximation by setting a large enough value for λ_0 ($10^4 \sim 10^5$).

3.1.3.2 Numerical scheme

The problem (4.3)-(4.6) is decomposed into fluid, solid and Lagrange-multiplier sub-problems in a partitioned coupling manner as follows [104]:

1. Fluid sub-problem (for \mathbf{u}_f^* and p)

$$\int_{\Omega} \left(\frac{\mathbf{u}_{f}^{*} - \mathbf{u}_{f}^{n}}{\Delta t} + \frac{1}{2} (3\hat{\mathbf{u}}_{f}^{n} \cdot \nabla \mathbf{u}_{f}^{n} - \hat{\mathbf{u}}_{f}^{n-1} \cdot \nabla \mathbf{u}_{f}^{n-1}) \right) \cdot \mathbf{v}_{f} d\mathbf{x}
+ \int_{\Omega} \left(-p\mathbf{I} + \frac{(\nabla \mathbf{u}_{f}^{*})^{T} + (\nabla \mathbf{u}_{f}^{n})^{T}}{2\text{Re}} \right) : \nabla \mathbf{v}_{f} d\mathbf{x} = \int_{P^{n}} \lambda^{n} \cdot \mathbf{v}_{f} d\mathbf{x}^{n},$$
(3.8)

$$\int_{\Omega} q \nabla \cdot \mathbf{u}_f^* d\mathbf{x} = \mathbf{0}. \tag{3.9}$$

where the vector Lagrange multiplier λ serves as a pseudo body force, and needs to be interpolated from the Lagrangian mesh via a Dirac delta function δ via:

$$\lambda^{n}(\mathbf{x}) = \int_{P^{n}} \lambda^{n}(\mathbf{X}) \delta(\mathbf{x} - \mathbf{X}) d\mathbf{X}.$$
 (3.10)

In the above the Eulerian and the Lagrangian mesh are denoted by \mathbf{x} and \mathbf{X} , respectively. We approximate the delta function as a tri-linear function to transfer the quantities between the unstructured Lagrangian mesh and the uniform Eulerian mesh (with grid size $\Delta x = \Delta y = \Delta z$) [77]

$$\delta(\mathbf{x} - \mathbf{X}) = \frac{1}{\Delta x^3} \phi(\frac{x - X}{\Delta x}) \phi(\frac{y - Y}{\Delta x}) \phi(\frac{z - Z}{\Delta x}). \tag{3.11}$$

$$\phi(r) = \begin{cases} 1 - |r| & |r| \le 1 \\ 0 & |r| > 1 \end{cases}$$
 (3.12)

This sub-problem is essentially the solution of the N-S equation. An efficient finite-difference-based projection method on a homogeneous half-staggered grid is employed [107]. All spatial derivatives are discretized with the second-order central difference scheme. Here we choose the reference speed U as the swimmer's COM speed at previous time step, and the computational domain position x is updated at the end of the fluid sub-problem step as

$$\mathbf{x}^{n+1} = \mathbf{x}^n + \mathbf{U}\Delta t. \tag{3.13}$$

2. Solid sub-problem (for \mathbf{x}^{n+1})

$$\int_{P_o} \frac{\rho_r \mathbf{x}^{n+1}}{\Delta t^2} \cdot \mathbf{v}_s d\mathbf{X} + \int_{P_0} (\nabla_0 \mathbf{v}_s)^T : \left[\lambda_0 \ln J \mathbf{F}^{-1} + G(\mathbf{F}_a^{-1}(\mathbf{F}_a^{-1})^T \mathbf{F}^T - \mathbf{F}^{-1}) \right]^{n+1} d\mathbf{X}$$

$$= \int_{P_0} \left[\frac{\rho_r \mathbf{x}^n}{\Delta t^2} + \frac{\mathbf{u}_f^*(\mathbf{x}^n)}{\Delta t} + (\rho_r - 1) \left(\frac{\mathbf{x}^n - \mathbf{x}^{n-1}}{\Delta t^2} + Fr \frac{\mathbf{g}}{g} \right) \right] \cdot \mathbf{v}_s d\mathbf{X}$$

$$+ \int_{P_0} (\nabla_0 \mathbf{v}_s)^T : \left[(\mathbf{F}^n)^{-1} \cdot \sigma_f^*(\mathbf{x}^n) \right] d\mathbf{X} - \int_{P^n} \lambda^n \cdot \mathbf{v}_s d\mathbf{x}^n, \tag{3.14}$$

where $\sigma_f^*(\mathbf{x}^n)$ denotes the viscous stress of the fictitious fluid inside the solid domain. The velocity field \mathbf{u}_f^* is interpolated from the Eulerian mesh via

$$\mathbf{u}_f^*(\mathbf{X}) = \int_{\Omega} \mathbf{u}_f^*(\mathbf{x}) \delta(\mathbf{x} - \mathbf{X}) d\mathbf{x}. \tag{3.15}$$

This sub-problem has been re-formulated to enhance the computational robustness at $\rho_r = 1$ without sacrificing accuracy [104]. A Lagrangian finite element method is used for the solution of this problem. We use the eight-node brick element (i.e., tri-linear interpolant) for the spatial discretization of the solid configuration and the Lagrange multiplier. In equation 3.14, the penalty function term (involving the material expansion modulus) is integrated using Gaussian rule with only one Gaussian point, and all other terms except the Lagrange multiplier term are integrated with 8 Gaussian points $(2 \times 2 \times 2)$. The Lagrange multiplier term is integrated using the trapezoidal rule. The resulting non-linear algebraic equations are solved with Newton iterations and the linearized equations in each iteration are solved with the conjugate gradient iterative method. Note that \mathbf{F}_a is a function of the reference configuration and time, and is independent of the current configuration, thus it is not more difficult to derive the Jacobian matrix for the active strain model compared to the original passive deformation model.

3. Lagrange multiplier sub-problem (for \mathbf{u}_f^{n+1} and λ^{n+1})

$$\int_{\Omega} \left(\frac{\mathbf{u}_f^{n+1} - \mathbf{u}_f^*}{\Delta t} \right) \cdot \mathbf{v}_f d\mathbf{x} = \int_{P^n} \left(\lambda^{n+1} - \lambda^n \right) \cdot \mathbf{v}_f d\mathbf{x}^n, \tag{3.16}$$

$$\int_{P^n} \left(\mathbf{u}_f^{n+1} - \frac{\mathbf{x}^{n+1} - \mathbf{x}^n}{\Delta t} \right) \cdot \zeta d\mathbf{x}^n = \mathbf{0}. \tag{3.17}$$

This sub-problem is solved with the direct-forcing scheme [107, 106], instead of the original Uzawa iterations [104]. It has been shown that two schemes produced the same results [106].

3.1.3.3 Validation

Considering that no benchmark problem for the active strain model is available and the original FD method for the passive deformation model has not been validated with quantitative comparisons, we verify the FD method with two benchmark problems: i) flow-induced vibration of a flexible 2D beam that is attached to the downstream side of a stationary cylinder, and ii) flow-induced flapping motion of a 3D flag.

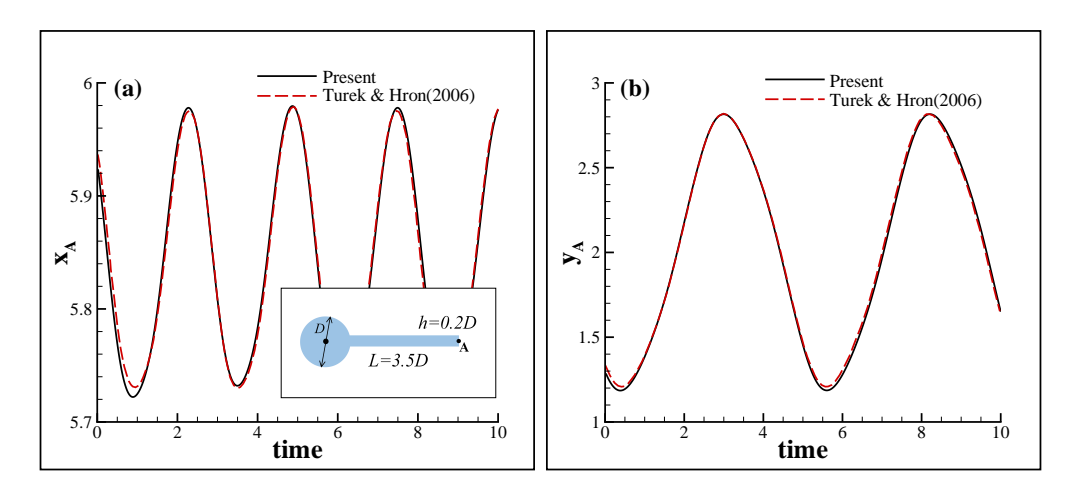


Figure 3.2: Time evolution of the displacements in both x- and y-directions of the central point on the plate trailing edge (point A, see inset of (a)) of a thin flexible plate in uniform flow.

We first consider the case of a 2D flow past a flexible beam that is attached to a rigid cylinder; see inset in Fig. 3.2(a). The cylinder has a diameter D, and the attached beam has a length L=3.5D and a thickness h=0.2D. The fluid domain is $L_x \times L_y=11D\times 4.1D$ We impose are no-slip conditions on the top and bottom, and a far-field condition (i.e., $\partial \mathbf{u}/\partial x=\partial p/\partial x=0$) on the right boundaries of the computational domain. On the left boundary, we specify a parabolic velocity profile with an average velocity U_0 as: $U(y)=6U_0y(L_y-y)/L_y^2$. In this case, we choose R=100 by choosing the velocity scale $U_c=U_0$. For elastic material, its rigidity is chosen as $E^*=E/(\rho_f U_0^2)=1400$. The density ratio between the solid and the fluid phase is chosen as $\rho_s/\rho_f=10$. The fluid mesh is discretized into uniform grids in both directions with a resolution of 1024×256 , while the solid domain is discretized into brick elements with a resolution of 210×12 . The time step is chosen as $\Delta t=0.002$. The time-varying displacements in both directions of the central point on the free end of the beam (point A) is shown in Fig. 3.2, and is in an excellent agreement with the previous studies. The amplitudes of the y-coordinate of the free end, the Strouhal number and the average drag coefficient $(C_d=\langle F_x\rangle/\left(\frac{1}{2}\rho_f U_0^2D\right))$ are also summarized in Table 1.

We then consider the second case of a 3D flexible plate of size (L, h, W) = (1, 0.01, 1) in a uniform flow whose leading edge is clamped (h is the plate thickness). The computational domain is rectangular, and its streamwise, transverse and spanwise directions are denoted by X, Y, and

Table 3.1: The amplitude of the central point on the free end and the Strouhal number and the average drag coefficient for a flexible beam

Works	Amplitude	Strouhal number	Drag coefficient
Turek and Hron (2006) [97]	0.83	0.19	4.13
Tian <i>et al.</i> (2014) [94]	0.78	0.19	4.11
Present	0.81	0.19	4.10

Z, respectively. Currently the domain size is chosen as $(L_x, L_y, L_z) = (8L, 8L, 2L)$ based on the plate length L. The uniform velocity U_0 is imposed on the inlet, top and bottom boundaries, respectively. The far-field and periodic conditions are imposed on the outlet and the spanwise direction, respectively. The fluid mesh resolution is $512 \times 512 \times 128$, the number of the solid elements is $80 \times 4 \times 80$, and the time step is $\Delta t = 0.001$. Here we choose Re to be 200, the mass ratio $\rho_s h/(\rho_f L)$ to be 1.0, the dimensionless bending rigidity $Eh^3/[12(1-\nu_s^2)\rho_f U_0^2 L^3]$ to be 0.0001. The Young's modulus is computed correspondingly for the given plate size and the Poisson's ratio $(\nu_s = 0.4)$, and then the shear and volume moduli can be obtained via the relationships $G = E/[2(1 + \nu_s)]$ and $\lambda_0 = E/[3(1 - 2\nu_s)]$. Again, in Fig. 3.3 and Table 2, our results of both tip displacement and time-averaged drag coefficients show good agreements with the previous studies by Huang and Sung [43], and by Tian et al. [94]. In addition, we have examined the impacts of different interpolating functions on numerical accuracy by choosing either the tri-linear or the smoothed 2-point function [103],

$$\phi(r) = \begin{cases} 3/4 - r^2 & |r| \le 0.5 \\ 9/8 - 3|r|/2 + r^2/2 & 0.5 < |r| \le 1.5, \\ 0 & 1.5 < |r| \end{cases}$$
(3.18)

and found that they indeed yield very similar results.

3.2 Results and Discussion

Note that slender biological swimmers (e.g., fish and jellyfish) not only adopt some unique shapes to enhance thrust generation but also distribute muscle inhomogeneously across their thin

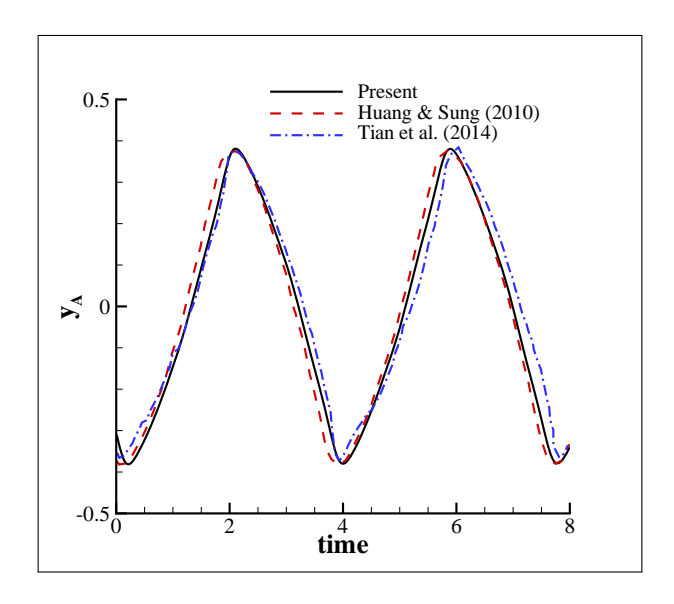


Figure 3.3: Time evolution of the transverse displacement of the central point on the plate trailing edge of a thin flexible plate in uniform flow.

Table 3.2: The amplitude of the central point on the plate trailing edge and the Strouhal number and the average drag coefficient for a flag flapping in uniform flow.

Works	Amplitude	Strouhal number	Drag coefficient
Huang and Sung (2010) [43]	0.780	0.260	
Tian et al. (2014) [94]	0.806	0.266	0.543
Present(tri-linear function)	0.762	0.266	0.579
Present(smoothed 2-point function)	0.760	0.260	0.586

body to facilitate generation of desired deformation. Therefore, in order for soft robots to achieve effective swimming motions, it is critical to design appropriate swimming strategies (i.e. swimming gaits) by taking into account their geometrical characteristics, material properties, and deformation generation due to the applied active strains. In the following, we show a few successful designs of soft robotic swimmer prototypes that undergo undulatory swimming and jet propulsion by applying active (contracting) strains on different locations of thin elastic plates with different shapes. To seek certain optimized swimming strategies, we systematically explore the parameter spaces by performing direct simulations to resolve the nonlinear fluid/elastic-structure interactions at the moderate Reynolds numbers regime where both the viscous and the inertia forces are important. In all simulations, we fix the density ratio $\rho_r = 1$ for light-weight structures in both 2D and 3D.

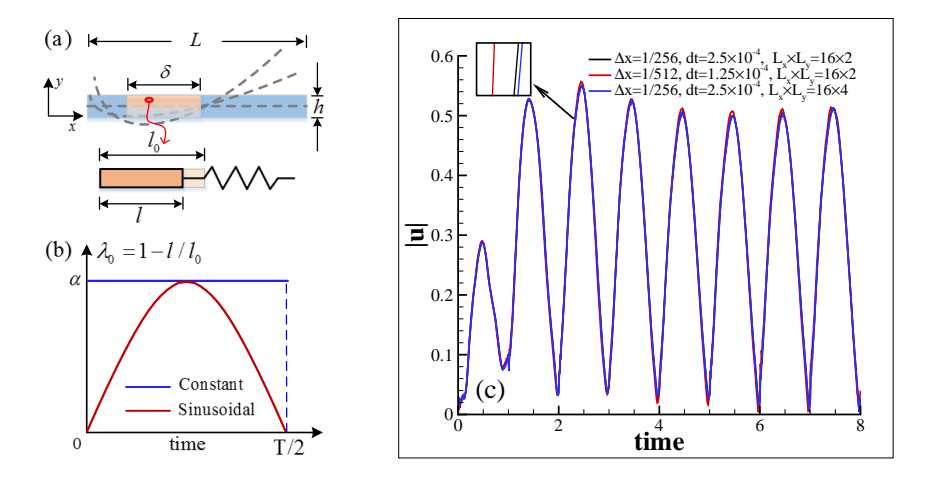


Figure 3.4: (a) Schematic of a 2D beam under contracting actuation. The active segment is highlighted in orange. The microscopic mechanical model of the active contraction is illustrated by the zoom-in schematic on bottom. (b) Either a constant (i.e., a step-like) or a sinusoidal contraction is applied during the first half period $0 \le t < T/2$ on the two surfaces alternatively. Then the actuation is turned off for the second half $T/2 \le t < T$. (c) Convergence study for the 2D beam under a sinusoidal actuation by varying domain size, mesh resolution, and time step. The other parameters are Re = 500, G = 1000, $\delta = 0.4$, $\alpha = 0.15$, and T = 2.

3.2.1 Two-Dimensional Case

We begin by manipulating a 2D beam of length L=1 and a uniform thickness h=0.03 as shown in Fig. 4.1(a). Here we consider undulation swimming motion for slender biological swimmers that perform forward locomotion by generating wavy deformations to produce thrust force. As suggested by the simulation results that use the immersed boundary method [36, 98], following the classical Hill muscle model by distributing three-element spring units on the top and bottom surfaces can effectively generate oscillating-switching bending deformations which resemble undulatory swimming motions. Without using complicated models to mimic the biological tissues' mechanical properties (e.g., viscoelasticity, electrophysiology effects [100]), we assume the soft active material is hyperelastic which, at the microscopic level, is driven by a contracting element with a length l and an initial length l_0 , yielding an effective contractile strain $\lambda_a = \frac{l}{l_0} = 1 - \lambda_0$ locally. It connects with a neo-Hookean spring that generate elastic stresses in response to the active input of the contraction field which, in 2D, is simply chosen as a homogeneous field $\mathbf{F}_a = \operatorname{diag}\left(\lambda_a, \lambda_a^{-1}\right)$ applied on the

active segment δ .

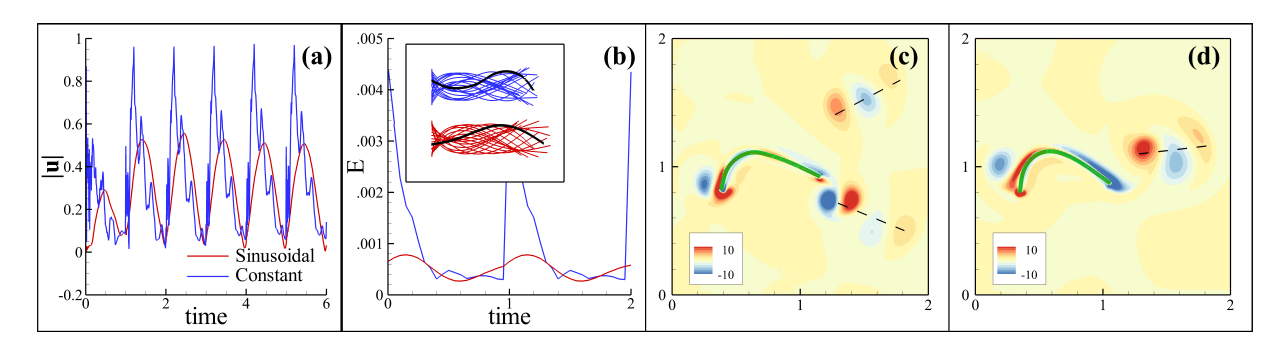


Figure 3.5: Swimming motions of a 2D elastic beam under the constant and sinusoidal actuation when fixing Re = 500 and T = 2.0. (a) Instantaneous velocity as a function time. (b) Strain energy E as a function of time. Inset in (b): Envelope trajectories of the plate midline during one actuation period. Snapshots of the corresponding vorticity fields are shown in panels (c) (constant) and (d) (sinusoidal).

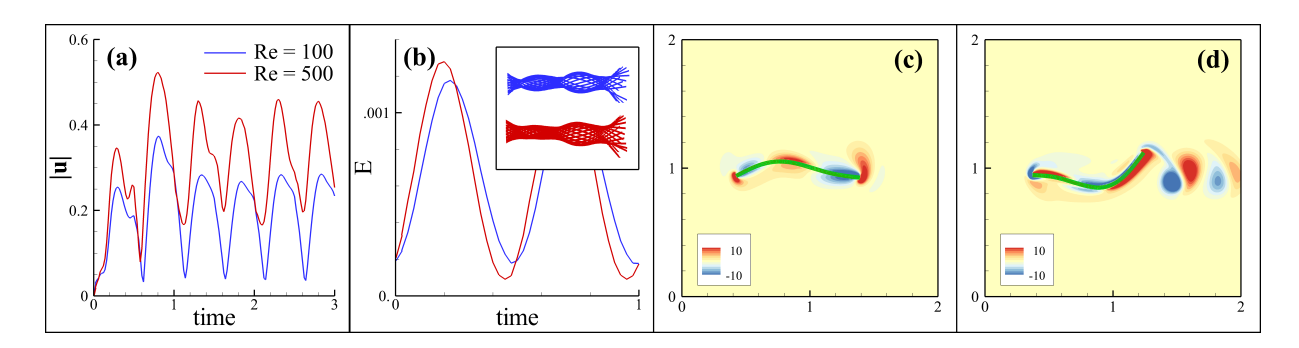


Figure 3.6: Comparisons of the free swimming motion of a 2D elastic beam at Re = 100 and Re = 500 when fixing T = 1.0 for sinusoidal actuation following Eq. (3.20). (a) Instantaneous velocities as a function time. (b) Mean elastic energy densities e as a function of time. Inset in (b): Envelope trajectories of the plate midline during one actuation period. Snapshots of the corresponding vorticity fields are shown in panels (c) at Re = 100 and (d) at Re = 500, respectively.

We follow the geometry adopted by Hamlet $et\ al.$ [36] by choosing the first 10% of body length from the left to be passive, and then connecting an active section of length δ . To activate the beam, as shown in panel(b), we apply the constant $(\lambda_a \sim 1-\alpha)$ or time-dependent (e.g., sinusoidal $\lambda_a \sim 1-\alpha \sin\left(\frac{2\pi}{T}t\right)$) contractile strain field alternatively on the both sides within a time period T. Here α is an amplitude which characterizes the contraction strength. In the meantime, the maximum strain is imposed on the surface with an exponential decay in the thickness direction.

Mathematically, it is convenient to define λ_a for a constant actuation as

$$\lambda_{a} = \begin{cases} 1 - \alpha \exp\left(-\frac{h - y}{d_{0}}\right), & 0 \le t \le T/2\\ 1 - \alpha \exp\left(-\frac{y}{d_{0}}\right), & T/2 < t \le T. \end{cases}$$
(3.19)

Or,

$$\lambda_{a} = \begin{cases} 1 - \alpha \sin(\frac{2\pi t}{T}) \exp\left(-\frac{h - y}{d_{0}}\right), & 0 \le t \le T/2, \\ 1 - \alpha \sin(\frac{2\pi t}{T}) \exp\left(-\frac{y}{d_{0}}\right), & T/2 < t \le T \end{cases}$$
(3.20)

for a sinusoidal actuation. In the above, d_0 controls the steepness of the decay, and is chosen as h/3 in all simulations in both 2D and 3D. Typical resultant bending deformations are illustrated in Fig. 4.1(a) by a few snapshots of the midline position (grey dashed lines). As shown in Fig. 4.1(c), we have performed a convergence study for the swimming beam under a sinusoidal actuation by varying domain size, mesh resolution, and time step. In the following simulations, we have chosen the Eulerian domain to be $L_x \times L_y = 16 \times 2$, which is uniformly partitioned in the x - y plane with the grid size $\Delta x = 1/256$. The solid domain is partitioned by using rectangular brick elements with the resolution 160×8 so that the area ratio of the Eulerian element to the Lagrangian element is about 1.5 [104].

In Fig. 4.3, we compare the swimming motions due to different actuation methods (also see movie S1) when choosing Re = 500, G = 1000, $\delta = 0.4$, $\alpha = 0.15$, and T = 2. We choose the computation mesh Panel(a) shows the magnitude of the instantaneous velocity, i.e., $|\mathbf{u}|$, of the center-of-mass (COM) positions. The spikes suggest sudden changes in the swimming speed due to the way that the actuation abruptly switches between the constant actuation applied two surfaces, while the velocity varies smoothly when the two sides are under a periodic sinusoidal actuation. When projecting the velocity on its swimming direction, the two actuation methods result in approximately the same time-averaged swimming speed $\langle U \rangle \approx 0.13$. In panel(b), we calculate the instantaneous elastic strain energy $E(t) = \int_P w dV$ where $w = \frac{1}{2}Gtr\left(\mathbf{F}_e \cdot \mathbf{F}_e^T - \mathbf{I}\right)$ is the energy density for incompressible materials in terms of the first invariant of the elastic stress tensor [71]. Apparently the sinusoidal actuation requires much gentler elastic deformations compared to the constant one. The snapshots in panels(c) and (d) highlight the drastic differences of the wake

structures generated the differing actuation schemes as characterized by the envelop trajectories of the midline (see Inset of panel(b)). As highlighted by the black solid lines in the inset of (b), the beam exhibits larger deformations under a constant actuation. A pair of vortices of opposite sign is generated during each tail upward/downward beating, leading to two vortex streets that are widely separated; see panel(c). In comparison, a sinusoidal actuation yields a smooth swimming motion, shedding vorticies to form a reverse von Kármán vortex street.

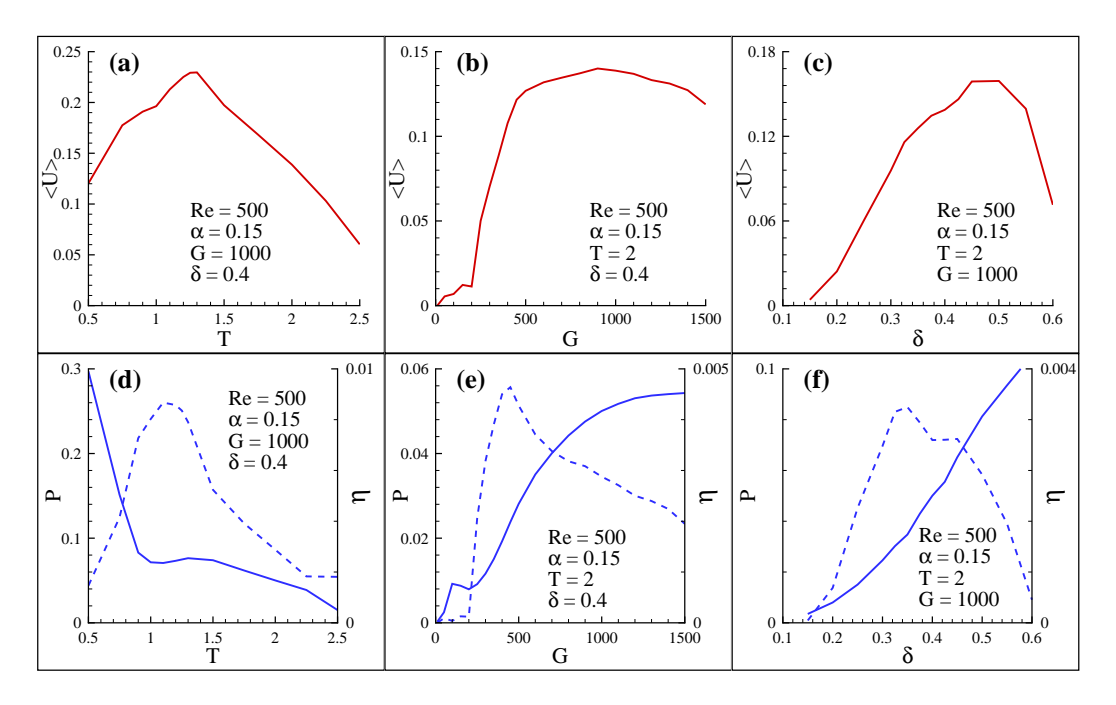


Figure 3.7: Measurements of the averaged swimming speed $\langle U \rangle$ in (a-c), and power P (solid blue lines) and efficiency η (dashed blue lines) in (d-f) of an swimming beam under a sinusoidal actuation following Eq. (3.20) when fixing Re = 500, α = 0.15, and varying T, G and δ , respectively.

Next, we examine the Reynolds number effect by simulating the swimming motions under a sinusoidal actuation when choosing computational parameters $\delta = 0.4$, $\alpha = 0.15$, T = 1, G = 1000 at Re = 100,500 respectively. As shown in Fig. 3.6(a), the swimming plate moves faster as inertia increases even if the elastic deformations at the two Reynolds numbers are similar as shown in panel(b). Panel(c) suggests that at Re = 100, the viscous effect still dominates without significant flow separation and vorticity generation. The undulating deformation is useful to overcome the viscous effect by taking advantage of the anisotropic drag forces exerted upon the beam. As shown

in panel(d), apparently the inertial effect at Re = 500 enhances the momentum exchange to generate a reverse von Kármán vortex street, which effectively generates thrust forces to propel the swimmer.

After choosing a particular actuation method (e.g., sinusoidal), we may study the 2D undulating swimming motion by systematically exploring the parameter space of (Re, α , T, G, δ). Since simultaneously optimizing all these parameters can be very challenging, here we examine the differences of the 2D swimming motions by varying individual parameters. As shown in Fig. 3.7(a)-(c), we vary parameter T, G, or δ individually to seek the fastest moving speed $\langle U \rangle$ and maximum swimming efficiency. In panel(a), such motion occurs when $T \approx 1.3$ and the other parameters are fixed. Asymmetric and non-periodic undulations have been observed when actuation is either very fast (T < 0.5) or slow (T > 2.5), which barely generates a directional motion. In panel(b), when varying G only, the corresponding fastest swimming motion occurs at $G \approx 900$. Interestingly, we have observed that at small G (i.e., G < 200), while swimming slowly, the beam in fact can move back and forth as actuation switches sides during one period. When G becomes larger, the beam exhibits a directional motion with its COM velocity sharply increasing before saturating around U = 0.13 at G > 500. In panel(c), the maximum speed occurs when approximately half of the body is actuated. As δ goes beyond 0.6, we have again observed that non-periodic and asymmetric swimming motions.

In panels(d-f) we estimate the power done by the beam upon the fluid as [99]

$$P = \frac{1}{2} \frac{d}{dt} \int_{\Omega_f} |\mathbf{u}_f|^2 dV + \frac{2}{\text{Re}} \int_{\Omega_f} |\nabla \mathbf{u}_f|^2 dV, \tag{3.21}$$

based on which we define the swimming efficiency as

$$\eta = \frac{E_k}{E_f + E_k},\tag{3.22}$$

where $E_k = \frac{1}{2} M_f \langle U \rangle^2$ is the kinetic energy of the elastic beam, and $E_f = \int_0^T P dt$ represents the total energy delivered to the fluid due to the mechanical work performed by the swimming motion. We have found that P varies approximately monotonically with the varying parameters, leading to the maximum efficiencies around T = 1.1, G = 400 and $\delta = 0.3$, respectively.

3.2.2 Three-Dimensional Cases

3.2.2.1 Deformation Control

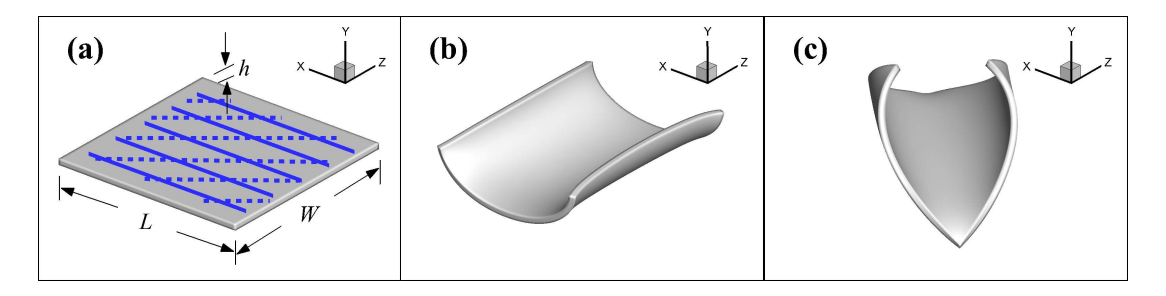


Figure 3.8: (a) Examples of different actuation patterns (horizontal vs. diagonal) on the top surface of a square plate, and the corresponding bending deformations in (b) and (c).

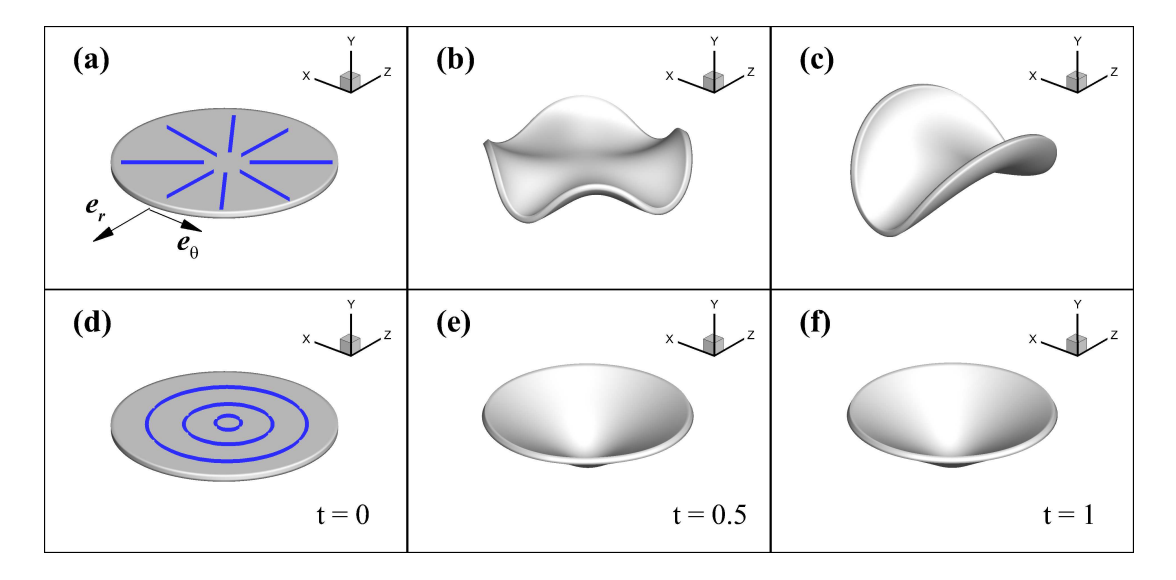


Figure 3.9: Snapshots of circular plate under (a-c) radial and (d-e) azimuthal actuation.

In 3D, the active strain field can be defined as $\mathbf{F}_a = \operatorname{diag}(\lambda_1, \lambda_2, \lambda_3)$, defined in the principal coordinates in the un-deformed configuration. We align $\lambda_1 = \lambda_a < 1$ with the local contracting direction while defining the remaining principal stretches as $\lambda_2 = \lambda_3 = \lambda_a^{-1/2}$. This assumes that the deformation is homogeneous in the directions of λ_2 and λ_3 . However, design and control of elastic deformations in 3D can prove to be much more complicated than in 2D, especially when dealing with complex geometries. As demonstrated in Fig. 3.8(a)-(c) for a rectangular plate,

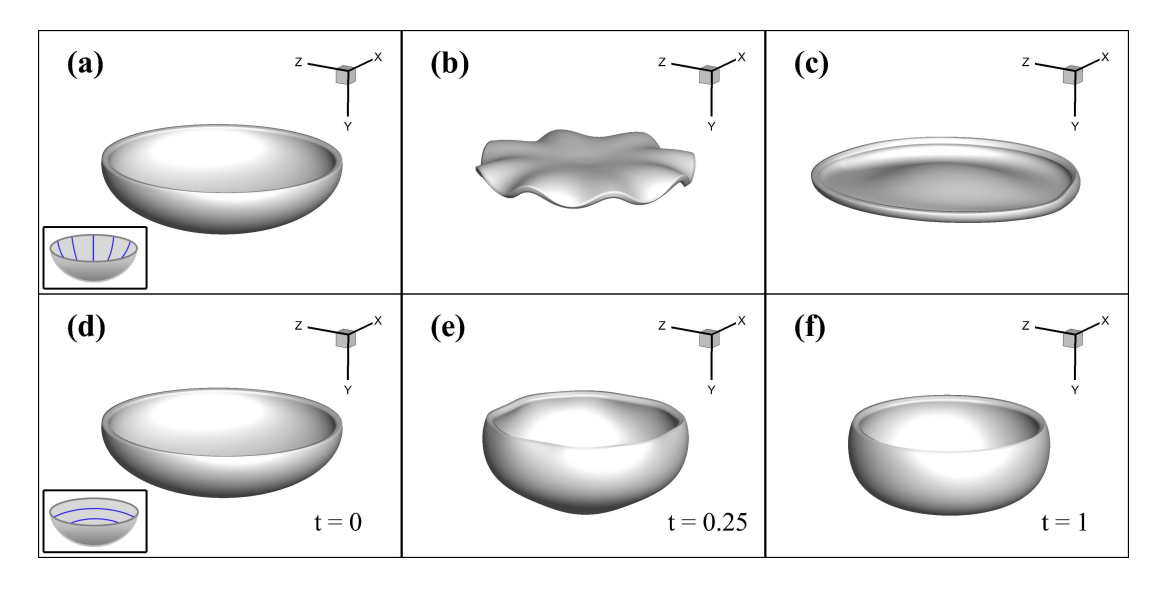


Figure 3.10: Snapshots of an oblate bell under (a-c) radial and (d-e) azimuthal actuation.

the resultant bending deformation can be adjusted by distributing the constant contracting field of λ_1 along arbitrary directions (e.g., horizontal in (b) and diagonal in (c)) in the un-deformed configuration.

Another example is shown in Fig. 3.9, where we change the plate shape from rectangular to circular, and apply isometric actuation in either radial or azimuthal direction. Apparently, when radially activated (i.e., $\lambda_a \mathbf{e}_r$, see panel(a)), the plate apparently experiences a two-step deformation during which an intermediate equilibrium shape occurs in panel(b) due to a wrinkling instability, and then relaxes and switches to become a steady-state saddle shape in panel(c). Active deformation involving complex transient dynamics like this is difficult to control, and hence the radial actuation is not preferred. On the other hand, when a constant contraction is applied in the azimuthal direction (i.e., $\lambda_a \mathbf{e}_\theta$, see panel(d)), the circular plate can generate stable reversible bending deformation as shown in panels(e,f). Similar actuation strategies may be used for other thin soft structures with azimuthal symmetry. As shown in Fig. 3.10, when a radial actuation is applied on the inner surface of an oblate bell (see panel(a)), an opposing expansion occurs in the azimuthal direction due to the material incompressibility, driving a transient wrinkling deformation (see panel(b)). Then the whole body relaxes to become a steady flattened disk as shown in panel(c). Alternatively, as shown

in Fig. 3.9(d-f), applying an azimuthal actuation results in efficient contraction of the entire-body, which, as shown below, can effectively be used to generate reversible contraction motions to power a jellyfish robotic swimmer.

3.2.2.2 Undulatory Swimming

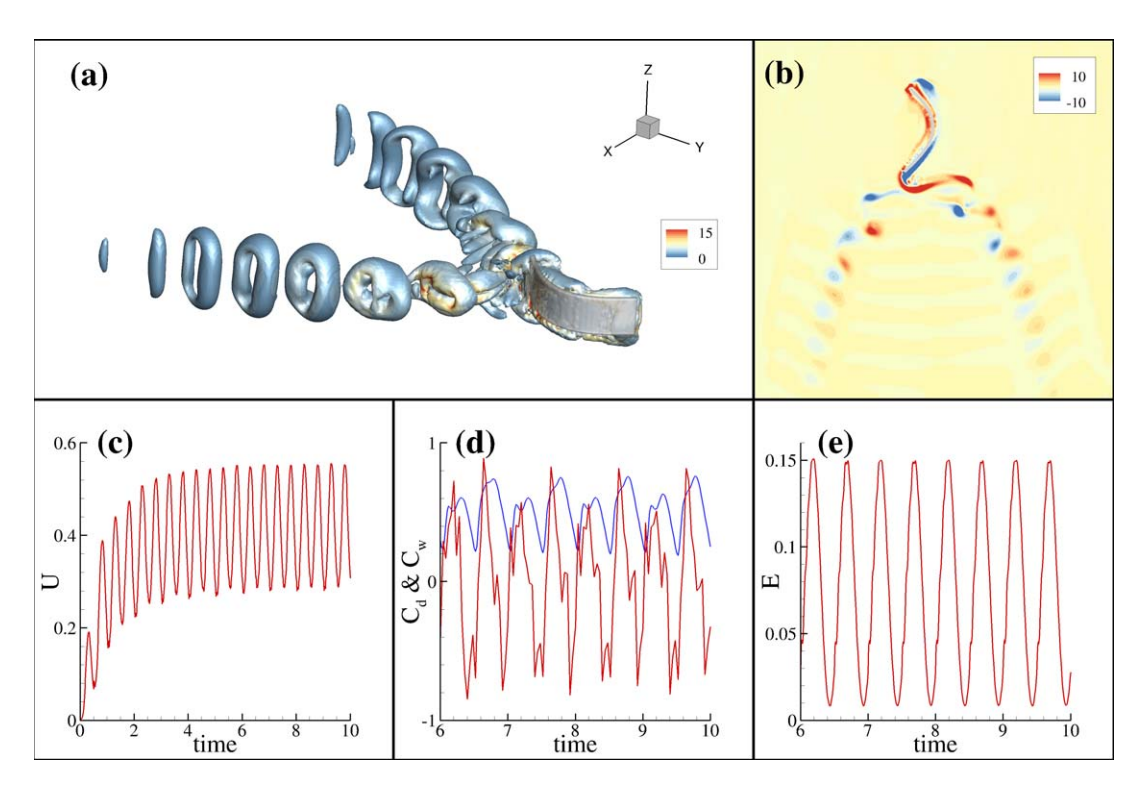


Figure 3.11: Snapshots of 3D vortex-core structures (a) and the projection of 2D vortices on the x-y plane (b) of an elastic plate that performs undulation under a sinusoidal actuation following Eq. (3.20). The computation parameters are chosen as $\alpha=0.2$, $\delta=0.5$, T=1.0, G=1000, and Re = 1000. (c) Instantaneous swimming velocity as a function of time. The color bar represents the magnitude of the 3D vorticity, i.e., $|\omega_f|$ (b) Drag coefficient $C_d = F_y/\left(\frac{1}{2}\langle U\rangle^2 A\right)$ (red line) and wake-induced force (i.e., Lamb vector) coefficient $C_w = -F_L/\left(\frac{1}{2}\langle U\rangle^2 A\right)$ (blue line) as functions of time. (e) Strain energy E as a function of time.

Similar to the 2D cases discussed in Section 3.2.1, we first examine the undulatory swimming motion of a 3D rectangular plate. Here we adopt the 2D shape in Fig. 4.1(a), and extrude the beam of length L and thickness h along its third dimension for a certain width W. In Fig. 3.11, we show a case of a swimming plate of size (L, h, W) = (1, 0.03, 0.25) that undergoes a quasi-steady

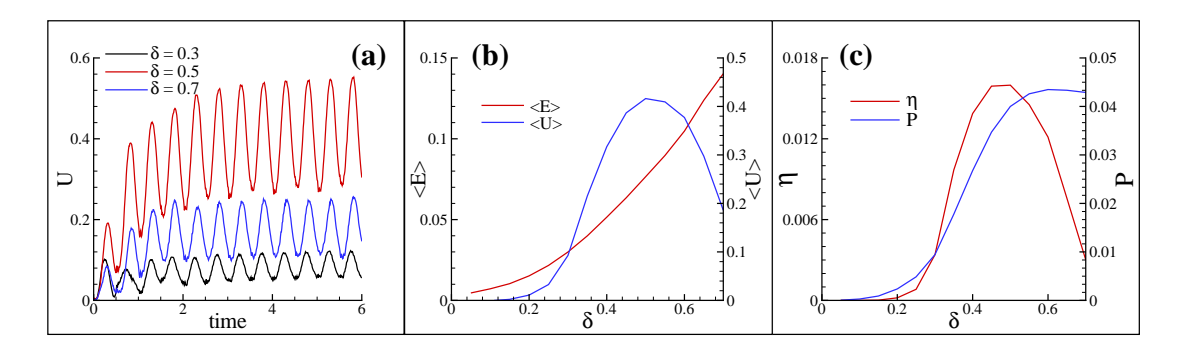


Figure 3.12: Simulation results of an undulating swimming motion by varying δ while fixing $\alpha=0.2, T=1.0, G=1000$ and Re = 1000. (a) Instantaneous swimming speed U at $\delta=0.3,0.5,0.7$, respectively. (b) Time-averaged swimming speed $\langle U \rangle$ and strain energy $\langle E \rangle$ as a function of δ for periodic locomotion. (c) Power P and efficiency η as a function of δ .

undulatory swimming motion, due to sinusoidal contractions (Eq. (3.20)) applied alternatingly on both sides. Again, a uniform mesh is used for the Eulerian domain $L_x \times L_y \times L_z = 2.8 \times 2.8 \times 0.7$ with the resolution $256 \times 256 \times 64$. The Lagrangian domain $L \times h \times W = 1 \times 0.03 \times 0.25$ is partitioned into brick elements with the solution $84 \times 3 \times 21$, leading to the volume ratio (i.e., Eularian vs. Lagrangian) about 1.0. The other computation parameters are chosen as T = 1.0, $\delta = 0.5$, G = 1000 and Re = 1000.

In Fig. 3.11(a), we visualize the 3D vortex structures by using the so-called λ_{ci} criterion [109, 12], together with the distribution of the vorticity component $\omega_z = \frac{\partial u}{\partial y} - \frac{\partial v}{\partial x}$ on a 2D cross-section on the (x-y) plane in panel (b). In contrast to the 2D case where the shedding vorticies form a reverse von Kármán vortex street, here flow separation generates two toroidal structures during each beating motion, leading to two arrays of vortex rings. Apparently, the dynamics quickly become periodic as shown by the COM velocity in panel(c), as well as the strain energy in panel(e), suggesting a quasisteady free swimming motion. In panel(d), we show the drag coefficient $C_d = F_y/\left(\frac{1}{2} \langle U \rangle^2 A\right)$ in the swimming (y) direction, as well as the wake-induced force coefficient $C_w = -F_L/\left(\frac{1}{2} \langle U \rangle^2 A\right)$, where A = LW measures the dimensionless area of plate. Here the drag force is defined by net force exerted on the deformable body. The wake-induced thrust force $\mathbf{F}_L = \int_{\Omega_C} \omega_f \times \mathbf{u}_f dV$ from the vortex structures behind the swimmer, where $\omega_f \times \mathbf{u}_f = \left(\nabla \times \mathbf{u}_f\right) \times \mathbf{u}_f$ is the so-called Lamb vector [101]. We have found that the time-averaged net force is approximately zero, i.e., $\langle C_d \rangle = 0$,

since the active strain inputs do not generate extra forces. The oscillations of the C_d – t curve are largely due to the abrupt switches of the actuation on the two sides. In contract, the vortex rings induce negative hydrodynamic forces that vary periodically in the y direction to push fluid backward, which hence contributes to the thrust force generation for the swimming plate.

In Fig. 3.12 we show an example of varying the active segment length δ using a sinusoidal actuation when choosing $\alpha=0.2$, T=1.0, G=1000, and Re=1000. According to the instantaneous swimming velocity U in panel(a), the plate typically starts a steady-steady navigation after performing 5-6 strokes, with a significant increase in the speed when δ goes beyond 0.3. In panel(b), it is observed that the time-averaged swimming speed U increases with δ , and reaches a maximum value when $\delta \approx 0.5$. The time-averaged strain energy $\langle E \rangle$ grows monotonically as δ increases, driven by more inputs from the contracting strain field through \mathbf{F}_a . In panel(c), compared to the 2D case where the swimming power P grows monotonically with δ , it approximately saturates around $\delta=0.6$, leading to the maximum efficiency at $\delta\approx0.5$.

3.2.2.3 Jet-propulsion Swimming

Next we examine jet-propulsion based swimming (e.g., jellyfish) that propels the swimmer by squirting out water from the muscular cavity through periodic contractions. We follow the design reported in previous studies [85, 38, 1, 73] to construct an oblate 3D bell with its initial shape a partial prolate ellipse which can be described as

$$\left(\frac{x}{R_1}\right)^2 + \left(\frac{y}{R_2}\right)^2 + \left(\frac{z}{R_3}\right)^2 = 1$$
 (3.23)

where $R_1 = R_3 = 0.5$ and $R_2 = 0.25$, with a thickness h = 0.03. As discussed in Section 4.2, in order to generate robust whole-body contractions for a thin circular or bell-like plate, it is preferred to apply an active strain field with the principal contraction occurring in the azimuthal direction to avoid complex transient dynamics and instabilities of thin structures. We employ the same strategy here to apply the active contractions on the outer region of the inner surface marked by the blue circles in the inset of Fig. 3.13(a). The active segment is taken approximately 1/3 of the total

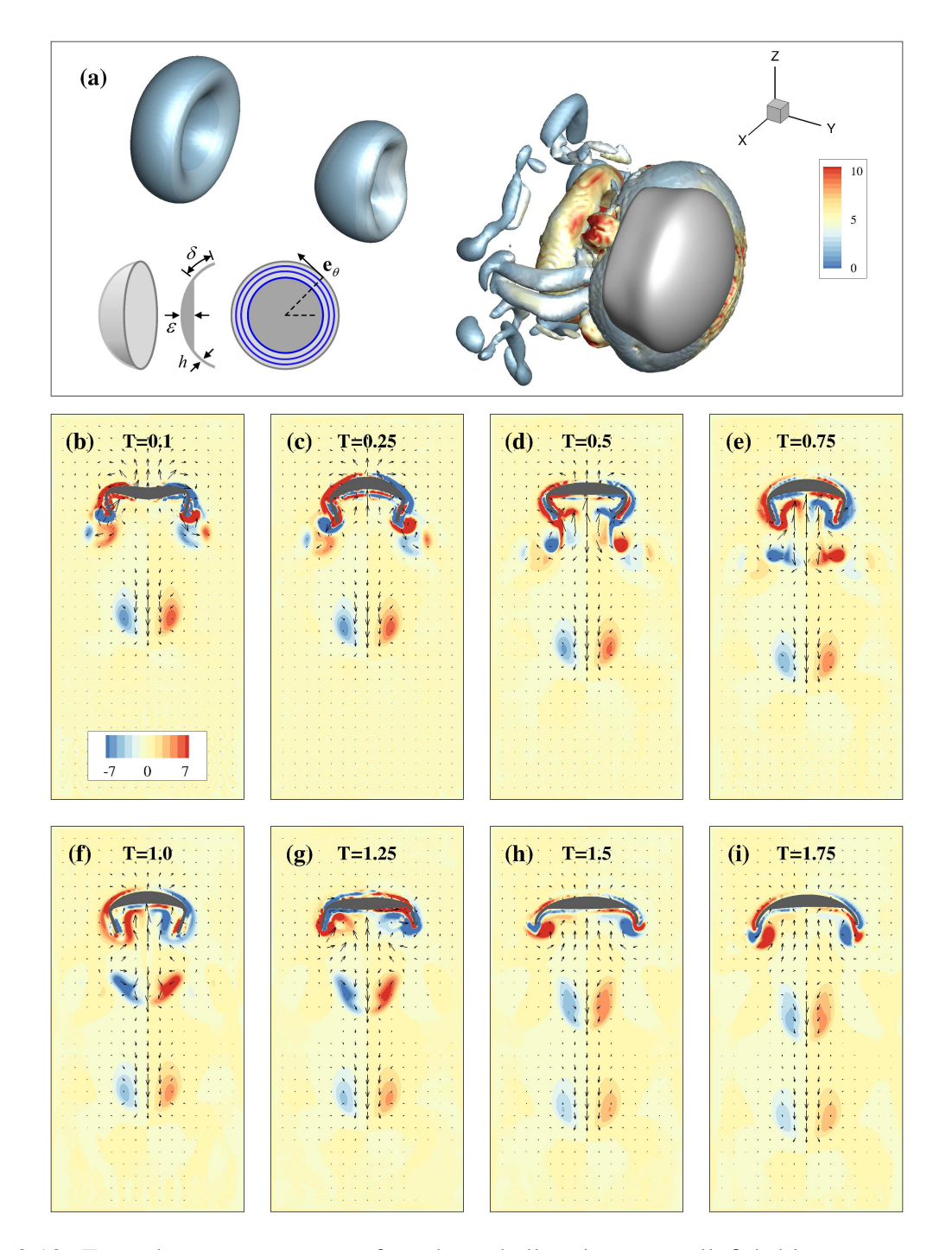


Figure 3.13: Typical vortex structures of an elastic bell undergoing jellyfish-like swimming in the moving coordinates, when choosing $\alpha=0.8$, T=2.0, G=100, R=500, $\varepsilon=0.1$, $\delta=0.21$, and h=0.03. (a) Vortex core overlaid on the solid mesh. The color bar represents the magnitude of the 3D vorticity, i.e., $|\omega_f|$. Inset: Schematic of the swimming elastic bell with a thickened top and azimuthal actuation. (b-i) In-plane fluid velocity vector field (u,v) overlaid on the colormap of vorticity on a 2D cross section plane during one period.

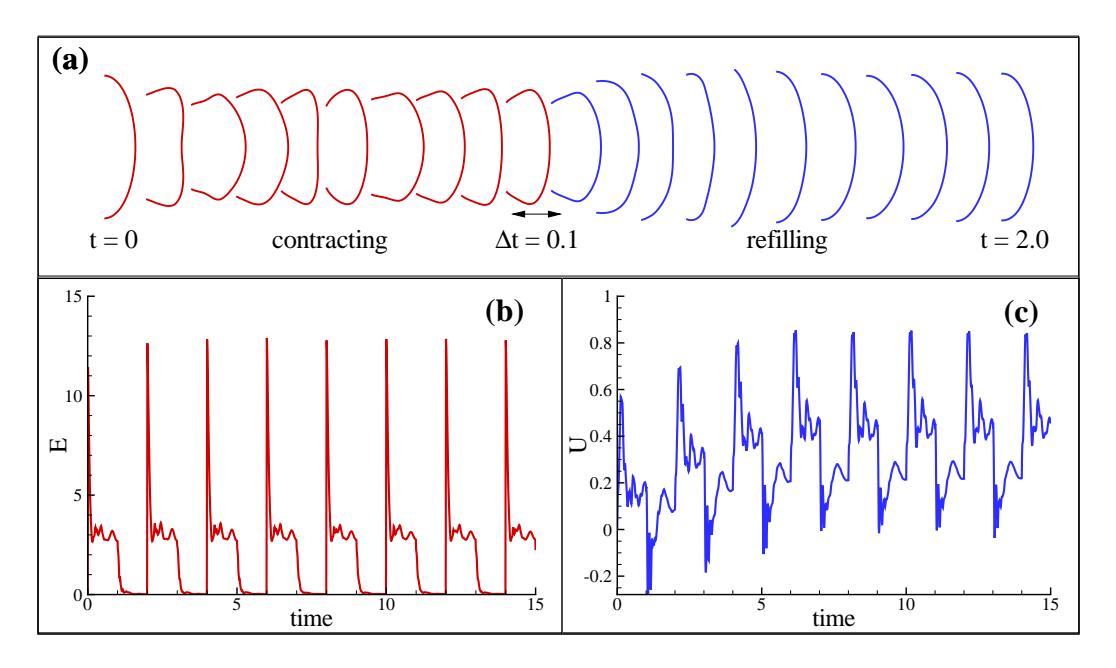


Figure 3.14: Highlights of bell's rowing motion accompanying whole-body vibrations through the kinematics of the bell arm during the contracting and refilling process (a). The instantaneous strain energy (b) and COM velocity(c) as function of time.

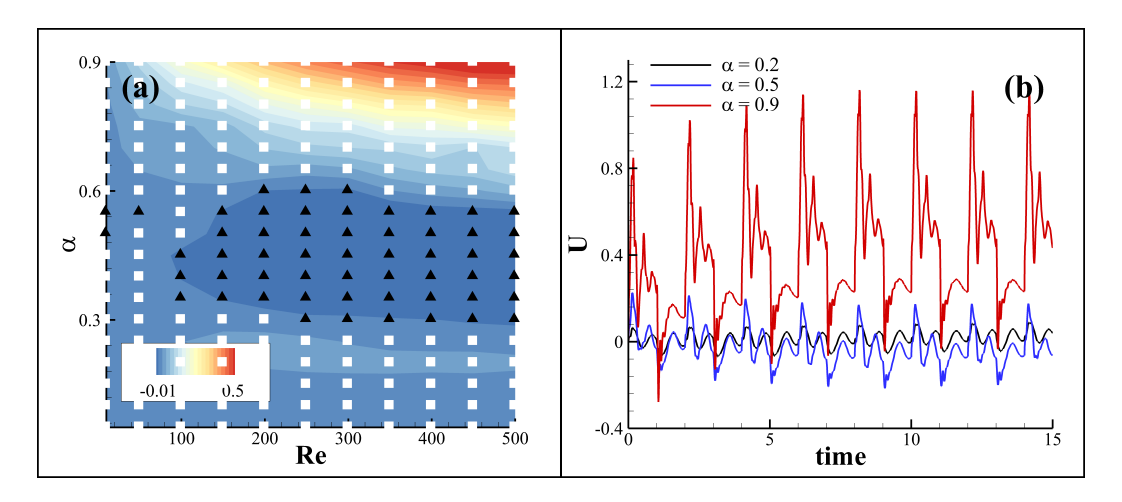


Figure 3.15: (a) Phase diagram of (α, Re) for a swimming bell undergoing jet-propulsion locomotion. The while and black symbols represent the forward and backward locomotion, respectively. The background color represents the time-averaged steady-state swimming velocity $\langle U \rangle$ at late times. (b) Typical instantaneous COM velocities when choosing $\alpha's$ in different regimes at Re = 250.

arm-length of the bell. In addition, we thicken the bell top (denoted by ε , and we fix $\varepsilon = 0.1$) in order to stabilize the elastic deformation [86, 75], which is important when both α and Re are large.

Here we employ a constant contraction following Eq. (3.19), instead of a gentle sinusoidal one which is not effective in generating rapid deformations as required by jet propulsion. Here we choose parameters based on the in vivo measurements of jellyfish tissue (e.g., mesoglea) [26]. By using the Young's modulus $\overline{G} \approx 100 Pa$ (the experimental data are approximately between 10 Pa and 100 Pa) as well as choosing the characteristic length $L_c \approx 1 cm$ [70] and velocity $U_c \approx 1 cm/s$, we choose the estimated the range of the dimensionless parameters as $G = 10 \sim 100$ and Re = $10 \sim 1000$. An example of bell swimming through jet-propulsion is shown in Fig. 3.13. The periodic axisymmetric contractions of the oblate elastic bell is reminiscent of the "rowing" motion of a jellyfish [16, 17, 18]. As shown in panel(a) for the 3D vortex cores overlaid on the solid mesh, after the initial transient, the elastic bell quickly starts to perform a stable forward swimming motion as the bell arm paddles, leaving behind toroidal vortices [19, 20, 73, 75]. The typical vortex dynamics during one period are illustrated in sequential snapshots of a 2D cross section shown in panels(b-i). In the power stroke corresponding to the first half-period (0 < t < T/2), see panels(b-e)), the applied active strains drive an inward contracting deformation. A shear-induced starting vortex is generated at the bell tip, interacting with the stopping vortex from the previous recovery stroke. After the starting vortex pair is separated from the bell arm, it is quickly advected with the jet flow due to the entrained fluid mass that is ejected downward (panels(c-e)). In the 2D plane, it is visualized as a vortex dipole. In the next half-period (T/2 < t < T), see panels(f-i)), turning off the active strains relaxes the elastic bell, driving a recovery stroke during which the fluid mass refills the bell. In the meantime, a stopping vortex with an opposite sign is generated and then adhered on the bell tip in the expansion process.

Details of the bell kinematics during one period is shown in Fig. 3.14. In panel(a), the sequential snapshots of the swimmer's contour are plotted. Note that while actively interacting with the fluid flows, imposing a large step-like contracting deformation of thin soft structures may easily trigger resonances during which the entire body oscillates quickly. For example, the bell top bounces back

and force during contraction (also see Fig. 3.13(b-e) as well as movie S2), and then overshoots the equilibrium position and swings back during relaxation. Such oscillatory behaviors can be quantitatively characterized by examining the variation of the total strain energy as a function of time in panel(b) where small amplitudes fluctuations are observed, immediately after the active strains being turned on and off. This is also reflected on the instantaneous average velocity in panel(c). As the bell starts to contract, its COM velocity quickly reaches a maximum, and then relaxes following the structural oscillations.

Systematically varying α and Re reveals various different regimes of jellyfish-like swimming motion as a result of the complex fluid-thin structure interactions. The dynamic behaviors are summarized in the phase diagram in Fig. 3.15(a) where the background colors represents the time-averaged COM velocities at steady state. As explained above, in the regime of large α and Re, the bell exhibits a fast forward swimming motion (see COM velocity marked by the red line in panel(b)), due to the strong positive feedbacks obtained from the fast fluid jet that carries fluid momentum backward. In the regime of smaller α and lower Re, however, while the bell arms are rowing, the locomotion is significantly weakened, largely due to the reduced amount of inputs from active contractions which hence leads to much weaker elastic deformations. Therefore, we find that the contracting deformation and the induced whole-body vibration are comparable. Their interplay eventually leads to complex arm kinematics as well as the momentum exchange between the fluid and the solid phase. Interestingly, we have observed that while swimming slowly (see the COM velocities marked by the blue and black colors in panel(b)), the bell can exhibit both forward (marked by solid squares) and backward (marked by black triangles, see movie S3) movement.

3.3 Concluding Remarks

In this work we have developed a FD-based computational framework to simulate swimming motion of soft robots by distributing active contracting stains on the elastic solid phase. The active strain model is based on the multiplicative decomposition of the deformation gradient tensor. As a first order approximation, the induced active deformation is independent of mechanical stress,

and can be easily measured experimentally by varying the external stimuli without imposing any mechanical load. From the biomimetic perspective, the active strain approach makes it straightforward to distribute active contractions in the muscle-fiber directions by following biological muscle architectures. Moreover, it is useful to take advantage of finite thickness of thin elastic structures by imposing an inhomogeneous contraction field to achieve desired elastic deformation.

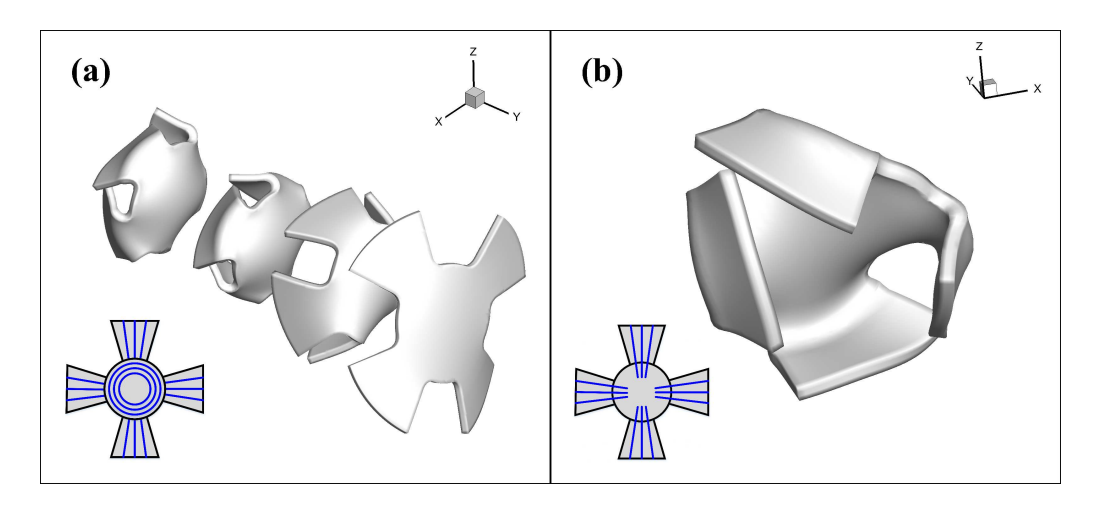


Figure 3.16: Comparison of the dynamics of soft robotic baby-jellyfish by distributing active contractions (marked by the blue lines) on (a) arms (i.e., radially) and partial of the circular disk (i.e., azimuthally), and (b) arms only. The four sequential snapshots in (a) highlight a stable directional locomotion in one actuation period. The snapshot in (b) shows an example of unstable asymmetric deformations without applying the azimuthal contraction in the disk to stabilize the structure.

Using the FD/active-strain method, we have been able to virtually design 2D/3D thin, light-weight soft robots with simple geometries (e.g., square, circle, bell) that perform undulation and jet-propulsion that are commonly employed by biological swimmers. It is also straightforward to activate soft swimmers of more complex geometries by distributing active strains with certain strength and direction on the desired locations. As shown in Fig. 3.16 and movie S4, we have followed the design by Nawroth *et al.* [70] to simulate a baby jellyfish (e.g. early-stage Ephyrae) that has a circular-disk body and multiple attached "arms". In particular, we have found that it is important to apply the active contracting stains to follow the muscle architecture observed in jellyfish. As shown in Fig. 3.16(a), we make the contractions occur in the radial direction to be aligned with the arms, together with a layer of contraction simultaneously imposed in the azimuthal

direction near the rim of the circular disk, which turns out to be critical in stabilizing the thinstructure deformation in forward swimming. A typical failure case is shown in Fig. 3.16(b) (also see movie S4) where only the radial contractions are applied. It is seen that the baby jellyfish cannot generate a clear directional locomotion due to very unstable deformations as shown by the snapshot. We have also tried varying the area covered by radial actuation but without success (not reported here).

While we only consider some relatively thin elastic structures in this paper, the FD/active strain model can be generally applied to manipulate elastic structures of arbitrary shapes and sizes. In particular, it is important to incorporate more elaborate constitutive models for viscoelastic or composite materials in order to mimic the behaviors of real biological tissues. Moreover, the active strain model can be flexibly implemented in other computational frameworks, either using boundary conforming methods or Cartesian grid methods, to handle coupling of soft actuation and the induced fluid motion. Last but not least, in order to optimize soft robotic systems with a large number of parameters (e.g., shape, stiffness, and actuation distribution) and possibly multiple design objectives (e.g., swimming speed, power, and efficiency), it is desirable to couple the existing CFD tools with multi-objective evolutionary algorithms and packages such as the Unified Non-dominated Sorting Genetic Algorithm (U-NSGA) II/III [22, 88, 21, 44]. The integrated framework like this will facilitate design of high-performance soft robotic machines for a wide range of applications in engineering and applied sciences.

CHAPTER 4

CFD-BASED MULTI-OBJECTIVE CONTROLLER OPTIMIZATION FOR SOFT ROBOTIC FISH WITH MUSCLE-LIKE ACTUATION

In this chapter, we develop a holistic computational framework for the design, control, and optimization of a soft robotic swimmer. With the aid of the high-fidelity FD/active-strain simulator, we implement feedback control strategies for the fully-coupled fluid/elasticity systems under actuation. Here we model the robotic fish as a 2D swimming elastic beam of a finite thickness, with contractive strains being imposed on two sides (with sharp decays in the thickness direction) periodically. When coupled with fluid flows, we demonstrate that the resultant undulatory free-swimming motions can be tuned by changing the active strain magnitude and frequency. Moreover, turning motions of the swimmer can be effectively accomplished by imposing asymmetric active strains on the two sides of the body. To achieve feedback control of the swimming motion, we couple the FD simulator with model-free proportional-integral-derivative (PID) control, which, arguably, is the most widely used feedback control scheme [82]. We seek optimal parameters of the PID controllers by using a genetic-algorithm-based multi-objective evolution method, U-NSGA-III [88], which produces a Pareto set of optimal solutions that clearly illustrate the tradeoffs among the objectives, with which the designer is able to make informed decisions.

To put the study in context, we consider a series of tasks where the soft swimmer tracks a moving target involving different trajectories and velocities, where a pair of PID controllers are used to adjust the amplitude and the bias of the active contractile strains imposed on the swimmer. The parameters of the PID controllers are optimized with three objectives: (1) tracking error, (2) cost of transport, and (3) the average elastic strain energy of the morphing body. In particular, the tracking error refers to the error between the swimmer position and the moving target position and is thus a metric on tracking performance, while the cost of transport represents a measure of locomotion efficiency. The elastic strain energy is also of importance because it is not only closely related to the required performance of the actuator, but also to the rate of fatigue failure to which

soft materials can be prone. The optimization is repeated at several Reynolds numbers for cases with different velocities and trajectories of a moving target. The resulting Pareto fronts of the multi-objective optimization problem reveal the correlations and trade-offs among the objectives and offer key insight into the design and control of soft swimmers. For example, the tracking error shows strong inverse correlation with the elastic energy. As another example, the optimized proportional gain parameters are also inversely related to the tracking error. Finally, the controller parameters produced via the proposed multi-objective optimization method demonstrate robustness across different conditions for the moving target and for the fluid environment.

4.1 Mathematical Model

In this section, we briefly review the major components of the FD/active strain method, which is the core of our CFD solver. The reader is referred to [58] for more details, especially on the derivation of the FD formulation and the numerical schemes. Mathematically, the solid deformation can be described by the deformation gradient tensor $\mathbf{F} = \partial \mathbf{x}/\partial \mathbf{X}$, which projects the current deformed state to the initial reference state. To capture the local actuation, we decompose the deformation gradient tensor \mathbf{F} into an active deformation tensor \mathbf{F}_a and an elastic deformation tensor \mathbf{F}_e following multiplicative decomposition [54, 55] such that

$$\mathbf{F} = \mathbf{F}_e \cdot \mathbf{F}_a. \tag{4.1}$$

Here \mathbf{F}_a is effectively an arbitrary function applied to the reference configuration that can be designed in terms of the desired location, direction, sign and strength. For incompressible solids that are considered here, we apply an incompressible restriction on actuation such that $det(\mathbf{F}) = 1$, where "det" represents the determinant. For simplicity, \mathbf{F}_a can be defined in the principal coordinates and transformed to the desired orientation by a standard rigid body rotation coordinate transformation. For an artificial muscle that contracts uniaxially when activated, we define $\mathbf{F}_a = \text{diag}[\lambda_1, \lambda_2, \lambda_3]$, where $\lambda_1 < 1$ represents a principal compression ratio, and $\lambda_2 = \lambda_3 = \sqrt{\lambda_1^{-1}} > 1$ are correspondingly the homogeneous deformation in the other two directions. With the total \mathbf{F} being mapped appropriately, the resultant elastic stress can be calculated through certain constitutive relation

 $\tau = \tau(\mathbf{F}_e) = \tau(\mathbf{F} \cdot \mathbf{F}_a^{-1})$ for various kinds of material (hyperelastic, viscoelastic, composite, etc.) conditions.

It is well understood that during an undulatory motion, fish use the anisotropic viscous drag force exerted in the longitudinal and transverse directions along the wavy body to create a net propulsive force [57]. As shown in Fig. 4.1(a), we adopt a simple 2D rectangular beam of length L and uniform thickness h to characterize the slender fish body shape. Without using complicated interconnected spring models to mimic the biological tissues' mechanical properties (e.g., the artificially coupled viscoelasticity and electrophysiology effects as what have been done by using the immersed boundary method [36, 98]), we assume that the soft active material is a continuous hyperelastic elastica which, at the microscopic level, is driven by a contracting element with an initial length l_0 , yielding an effective local contraction ratio $\lambda_a = \frac{l}{l_0} = 1 - \lambda_0$. At the microscopic scale, it connects with a neo-Hookean spring that generate elastic stresses in response to the active input of the contraction field. The latter, in 2D, is simply chosen as a homogeneous field $\mathbf{F}_a = \operatorname{diag}\left(\lambda_a, \lambda_a^{-1}\right)$ applied on the active segment.

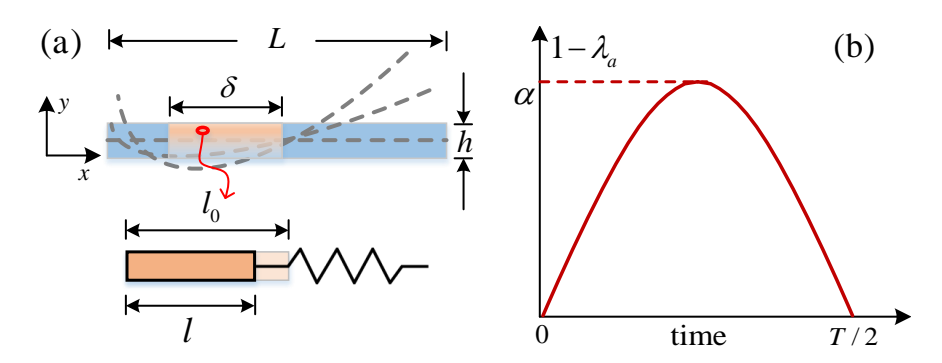


Figure 4.1: (a) Schematic of a 2D beam under contractile actuation (view from above). The active segment is of length δ . The microscopic mechanical model of the active contraction is illustrated by the zoom-in schematic on bottom. (b) Contractile actuation applied alternatively on the surfaces of two sides, which exponentially decays in the thickness (y) direction (not shown in the figure).

Here we follow the geometry adopted by Hamlet *et al.* [36] by choosing the first 10% of body length from the left to be passive, and then connecting an active section of length δ . To activate the beam, as shown in Fig. 4.1(b), we apply a constant ($\lambda_a \sim 1-\alpha$, for a fixed α) or time-dependent (e.g.,

sinusoidal, $\lambda_a \sim 1 - \alpha \sin\left(\frac{2\pi}{T}t\right)$) contractile strain field alternatively on both sides within a time period T. Here magnitude α characterizes the contraction strength. In the meantime, the maximum strain is imposed on the left (denoted by "L") or right (denoted by "R") side with an exponential decay in the thickness direction. Mathematically, it is convenient to define the sinusoidal actuation scheme as

$$\begin{cases} \lambda_a^L = 1 - \alpha \sin\left(\frac{2\pi t}{T}\right) \exp\left(-\frac{h-y}{d_0}\right), & t \in \left[0, \frac{T}{2}\right); \quad \lambda_a^L = 0, \quad t \in \left[\frac{T}{2}, T\right], \\ \lambda_a^R = 0, \quad t \in \left[0, \frac{T}{2}\right); \quad \lambda_a^R = 1 - \alpha \sin\left(\frac{2\pi t}{T}\right) \exp\left(-\frac{h-y}{d_0}\right), \quad t \in \left[\frac{T}{2}, T\right]. \end{cases}$$

$$(4.2)$$

In the above, d_0 controls the steepness of the decay, and is chosen as h/3 in all simulations in this work. Typical resultant bent shapes are illustrated in Fig. 4.1(a) by a few snapshots of the midline position (grey dashed lines). Therefore, continuously applying periodic contractions on both sides lead to an undulatory motion.

To resolve the FESI of soft robotic swimmers, we implement the above active strain model using a fictitious domain (FD) method [35, 104, 58]. The key idea of the FD method is that the interior of the solid is assumed to be filled with a fictitious fluid that is constrained to move at the same velocity with the solid by a pseudo body force (via a Lagrange multiplier). The advantage of the FD method is that the flow fields can be solved efficiently with a fixed Cartesian grid. Suppose that a deformable body of density ρ_s is immersed in the incompressible Newtonian fluid of viscosity μ and density ρ_f . Let Ω denote the entire computational domain containing both solid and fluid domains, and S(t) represent the solid domain. It is noted that tracking swimming objects in the fixed coordinates requires using a very large computational domain, which makes computation expensive. Alternatively, here we employ an instantaneous inertial frame Ω that co-moves with the swimmer at a certain reference speed U [56]. Then the dimensionless FD governing equations in the weak form become

$$\int_{\Omega} \left(\frac{\partial \mathbf{u}_f}{\partial t} + \hat{\mathbf{u}}_f \cdot \nabla \mathbf{u}_f \right) \cdot \mathbf{v}_f d\mathbf{x} + \int_{\Omega} \left(-p\mathbf{I} + \frac{1}{\text{Re}} (\nabla \mathbf{u}_f)^T \right) : \nabla \mathbf{v}_f d\mathbf{x} = \int_{S} \lambda \cdot \mathbf{v}_f d\mathbf{x}, \tag{4.3}$$

$$\int_{\Omega} q \nabla \cdot \mathbf{u}_f d\mathbf{x} = \mathbf{0},\tag{4.4}$$

where $\hat{\mathbf{u}}_f = \mathbf{u}_f - \mathbf{U}$. The dimensionless governing equations for neo-Hookean solid material $(\tau = G(\mathbf{B} - \mathbf{I}))$ are solved in the absolute references as

$$\int_{S} \left[(\rho_{r} - 1) \left(\frac{d\mathbf{u}_{s}}{dt} - Fr \frac{\mathbf{g}}{g} \right) \right] \cdot \mathbf{v}_{s} d\mathbf{x} + \int_{S} (\nabla \mathbf{v}_{s})^{T} : \left[\lambda_{0} \ln J \mathbf{I} + G(\mathbf{B} - \mathbf{I}) \right] d\mathbf{x} - \int_{S} (\nabla \mathbf{v}_{s})^{T} : \left(-p \mathbf{I} + \frac{1}{\text{Re}} \left[\nabla \mathbf{u}_{f} + (\nabla \mathbf{u}_{f})^{T} \right] \right) d\mathbf{x} = - \int_{S} \lambda \cdot \mathbf{v}_{s} d\mathbf{x}, \tag{4.5}$$

$$\int_{S} (\mathbf{u}_f - \mathbf{u}_s) \cdot \zeta d\mathbf{x} = \mathbf{0} \tag{4.6}$$

Equations (4.3)-(4.6) represent the fluid momentum equation, the fluid continuity equation, the solid momentum equation, and the velocity constraint in the solid domain, respectively. In these equations, \mathbf{u}_f is the fluid velocity, \mathbf{u}_s the solid velocity, p the fluid pressure, and λ the pseudo body-force (i.e., the Lagrange multiplier). The variables \mathbf{v}_f , \mathbf{v}_s , q and ζ are the corresponding variations, respectively. For the original FD method for the passive deformation model, $\mathbf{B} = \mathbf{F} \cdot \mathbf{F}^T$ is the left Cauchy-Green deformation tensor, here F being the deformation gradient tensor defined as: $\mathbf{F} = \partial \mathbf{x}/\partial \mathbf{X}$, in which \mathbf{x} and \mathbf{X} are the current and reference configurations of the solid, respectively. J is the determinant of \mathbf{F} , and J=1 for the incompressible solid. In contrast, for the active strain model studied, $\mathbf{B} = \mathbf{F}_e \cdot \mathbf{F}_e^T = (\mathbf{F} \cdot \mathbf{F}_a^{-1}) \cdot (\mathbf{F} \cdot \mathbf{F}_a^{-1})^T$, where \mathbf{F}_e is the elastic deformation tensor which causes the elastic stress, and \mathbf{F}_a is an input deformation tensor without generating elastic stress. In addition, g denotes the gravitational acceleration. The following characteristic scales are used for the non-dimensionlization scheme: L_c for length, U_c for velocity, L_c/U_c for time, $\rho_f U_c^2$ for pressure p, and $\rho_f U_c^2/L_c$ for Lagrange multiplier λ . The following dimensionless control parameters are also introduced: density ratio $\rho_r = \frac{\rho_s}{\rho_f}$, material parameters $\lambda_0 = \frac{\lambda_0}{\rho_f U_c^2}$ and $G = \frac{\overline{G}}{\rho_F U_c^2}$, Reynolds number $\text{Re} = \frac{\rho_f U_c L_c}{\mu}$, Froude number $Fr = \frac{gL_c}{U_c^2}$. Here $\overline{\lambda}_0$ is related to the compressibility property of the material and \overline{G} represents the shear modulus. It should be mentioned that for soft swimmers, the characteristic velocity is defined as $U_c = f_c L_c$ for a given reference actuation frequency f_c . In addition, in order to enforce the incompressibility constraint of the solid material, i.e., J = 1, we adopt a penalty function-like approximation by setting a large enough value for λ_0 (10⁴ ~ 10⁵).

4.2 Controller Design and Optimization

4.2.1 Control Scheme

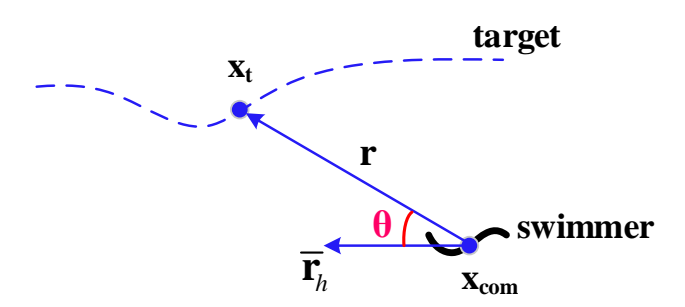


Figure 4.2: Schematic illustrating the control scheme based on the translational and rotational motion of a soft swimmer in relation to a moving target \mathbf{x}_t .

The primary goal for our control scheme is to make the soft swimmer effectively follow a moving target point. Such situations could arise in applications such as schooling (i.e., leader-follower configuration) or simply following a pre-determined desired trajectory. By its 2D nature our soft swimmer (elastic beam) is limited to forward swimming and turning, based on which we propose the following actuation scheme:

$$\alpha_R(t) = \alpha_0(t) + \frac{\beta(t)}{2}, \quad \alpha_L(t) = \alpha_0(t) - \frac{\beta(t)}{2}. \tag{4.7}$$

Here α_R and α_L correspond to the peak actuation strength in the right and left muscles, respectively, viewed in the body frame of the beam oriented from the tail toward the head. This differs from previous descriptions where both sides used a single value of constant α . Here α_0 is the mean contraction strength, which is assumed to be limited to the range $0 \le \alpha_0 \le \alpha_{max}$.

Turning can be achieved by biasing the contraction strength between the two actuated sides. The soft swimmer tends to turn in the direction of the stronger actuation, providing a means to control the beam's heading while swimming. Testing showed that this mechanism allows the beam to turn even while it is at rest with an averaged swimming speed of zero. The bias that leads to turning is denoted by β and is limited to the range $-\beta_{max} \le \beta \le \beta_{max}$. Based on the signs in (4.7), a positive value of β causes the beam to turn to the right and vice versa. Note that α_R and α_L are

limited to the same range as α_0 due to the physical constraints of the actuator, but the presence of β has the potential to push their values outside of this envelope. To prevent this while still achieving the desired bias, the portion of the bias outside the envelope is shifted to the opposite side. For example, if $\alpha_R = \alpha_0 + \frac{\beta}{2} \ge \alpha_{max}$, then $\alpha_R = \alpha_{max}$ and $\alpha_L = \alpha_{max} - \beta$. This is sufficient assuming that $\beta_{max} \le \alpha_{max}$ and in practice we typically set $\beta_{max} = \frac{1}{2}\alpha_{max}$.

To complete the control scheme it is necessary to connect our control variables, α_0 and β , to the physical state of the swimmer. We elect to use proportional-integral-derivative (PID) controllers as they have been widely used across disciplines. A general PID controller takes the following form:

$$f(t) = k_p e(t) + k_i \int_0^t e(t')dt' + k_d \frac{de(t)}{dt}$$
 (4.8)

where f(t) is the control variable, e(t) is the error corresponding to the difference between the target and current state, and the constants k_p , k_i , k_d are tuning parameters. The actuation strength α_0 is calculated based on the error in position, which is defined as:

$$e_1(t) = |\mathbf{r}| \operatorname{sgn}(\mathbf{r} \cdot \mathbf{v}). \tag{4.9}$$

In the above, the vector \mathbf{v} represents the moving target's velocity, and $\mathbf{r} = \mathbf{x}_t - \mathbf{x}_{com}$ connects the swimmer's center of mass (CoM) to the target position with its magnitude determining the magnitude of error (see schematic in Fig. 4.2). On its own this error magnitude would lead to the error being always positive which can potentially promote overshoot and lead the integral term to blow up. To prevent this we determine the sign of the error by $\mathrm{sgn}(\mathbf{r} \cdot \mathbf{v})$ (here "·" represents the vector inner product). If the target is moving away from the swimmer, $\mathbf{r} \cdot \mathbf{v}$ will be positive driving the swimmer to accelerate. Conversely, if the target is moving toward the swimmer, $\mathbf{r} \cdot \mathbf{v}$ will be negative causing the swimmer to slow down and potentially stop. If the controller returns a value that is out of bounds, the control variable is set to the respective bound and integration is stopped to prevent windup of the integral term. The overall result is a follower type scheme where the swimmer tends to remain behind the target and overshoot behavior is suppressed.

Special attention must be given to the derivative term due to the noise in the error. This is a common problem in PID controllers as noise can produce large and drastically varying values of

the derivative that can lead to undesirable behavior. The undulatory motion of the swimmer leads to a significant amount of sway which appears in the error as an oscillation driven at the forcing frequency. We filter out this oscillation by calculating the derivative based on the moving-average of the error, with the window size for averaging equal to that of the period of the forcing, T, as shown in (4.10). In particular, the following algorithm is used to approximate the derivative term:

$$\frac{de_1(t)}{dt} \approx \frac{\bar{e}_1(t) - \bar{e}_1(t - \Delta t)}{\Delta t}, \quad \bar{e}_1(t) = \frac{1}{T} \int_{t-T}^t e_1(t') dt'$$
 (4.10)

Directional control is achieved by determining β via a separate PID controller, where the error is based on the angle between the target vector, \mathbf{r} , and the swimmer's time-averaged heading vector, $\mathbf{\bar{r}}_h$. Due to the highly flexible nature of the swimmer, it is difficult to clearly define a body frame. As such we choose to define our orientation in terms of a chord line running from the tail to the head of the swimmer, \mathbf{r}_h . The large-amplitude motion of the head and tail means that this vector will vary significantly across a full swimming stroke, limiting its value as an instantaneous measure. However, time-averaging like that done in (4.10) provides a stable measure of the swimmer's heading. In sum, the bias control is based on the error $e_2(t) = \theta$, the angle between the vectors \mathbf{r} and $\mathbf{\bar{r}}_h = \frac{1}{T} \int_{t-T}^{t} \mathbf{r}_h(t') dt'$. Here $\mathbf{r}_h = \mathbf{x}_{head} - \mathbf{x}_{tail}$ represents the instantaneous direction vector that connects the head and tail. From the definition, since $\mathbf{\bar{r}}_h$ is already smoothed by the averaging, no special treatment is necessary for the derivative term.

4.2.2 Multi-Objective Optimization

Multi-objective optimization makes it possible to view the landscape of potentially optimal configurations. This allows for better understanding of the trade-offs between various objectives, leading to smarter design decisions. For example, in a swimmer a small decrease in speed may lead to sharp increase in efficiency or vice versa. The possibility of such a trade-off would not be apparent using single objective methods. The results of multi-objective optimization appear as a Pareto front, which is a surface in the objective space containing all solutions where each solution cannot be further improved in one objective without negatively affecting another objective(s).

Our work is focused on employing high-fidelity FSI simulations to investigate soft swimming mechanisms. This limits the use of reduced-order models, making evolutionary methods the most promising option for optimization.

Locomotion traditionally lends itself to two major design objectives, swimming speed and efficiency. However, our fully coupled model allows us to consider other important design criteria such as those related to the actuation of the swimmer. Soft materials tend to have limited lifecycles and can experience premature fatigue failure compared to traditional actuators, if cyclic loading conditions are not accounted for. Thus the design of such soft swimmer robots may best be done with the consideration of 3 or more objectives.

We elect to optimize the soft swimmer by employing a multi-objective evolutionary method, specifically the U-NSGA-III method as developed by Seada and Deb [88]. NSGA-III [21] is a recent extension of the widely used NSGA-II [22] that incorporates the idea of predefined reference vectors, increasing the possible number of objectives from 2 to 3+. The weakness of NSGA-III is that this change also makes it ineffective in the case of 2 or fewer objectives, meaning it is not a replacement for NSGA-II but instead a complementary method. U-NSGA-III solves this problem by extending NSGA-III in such a way that one or two-objective optimization becomes possible, making it a well rounded method capable of any number of objectives.

The soft swimmer is driven by two PID controllers with three tuning parameters each, leading to a total of six parameters. We optimize these parameters in terms of three objectives: combined average error (\bar{e}) , cost of transport (C_{ot}) , and average strain energy (\bar{E}) , which are elaborated below. The combined average error is the sum of the individually averaged errors as

$$\bar{e} = |\bar{e}_1| + |\bar{e}_2| \tag{4.11}$$

in which we track the entire evolution history during time t via $|\bar{e}_i| = \frac{1}{t} \int_0^t |e_i(t)| dt$, i = 1, 2. This provides a measure of tracking performance. The energy efficiency of the swimmer is evaluated through the measure of cost of transport,

$$C_{ot} = \frac{E_f}{d},\tag{4.12}$$

Table 4.1: Summary of the variables (PID tuning parameters) and objectives considered in the optimization.

Variables	Objectives
k _{p,position}	$ar{e}$
$k_{i,position}$	C_{ot}
$k_{d,position}$	$ar{E}$
$k_{p,heading}$	
k _{i,heading}	
k _{d,heading}	

where $E_f = \int_0^t Pdt$ is the total energy imparted to the fluid calculated by integrating the imparted power P, and $d = \int_0^t |\overline{\langle \mathbf{u}(t')\rangle}| dt'$ is the path length determined from the averaged motion of the center of mass, in which we define $\overline{\langle \mathbf{u}\rangle} = \frac{1}{T} \int_{t-T}^t \langle \mathbf{u}(t')\rangle \, dt'$ and $\langle \mathbf{u}\rangle = \frac{1}{V} \int \mathbf{u} \, dV$ (here we calculate the integral for the solid velocity \mathbf{u} in the Lagrangian domain of size V, and $\langle \rangle$ denotes a spatial average). Finally, the average total elastic strain energy is defined as

$$\bar{E} = \frac{1}{t} \int_0^t E(t')dt',$$
 (4.13)

where we define $E = \int G(\operatorname{tr}(\mathbf{B}) - 2) \, dV$ for an incompressible neo-Hookean material [5]. This relates the force and energy requirements of the actuators as well as the potential for fatigue due to cyclic loading.

4.3 Results and Discussion

4.3.1 Undulatory Swimming

We have observed that after the initial transient, the soft swimmer quickly reaches a quasi-steady forward swimming with periodic undulatory body motion. In Fig. 4.3(a), we show a typical flow map of the swimmer when choosing Re = 500, G = 1000, $\delta = 0.4$, T = 2, and symmetric actuation at $\alpha = 0.15$ (namely, $\alpha_0 = 0.15$, $\beta = 0$ in Eq.(4.7)). A pair of vortices of opposite signs is generated during each tail upward/downward beating, leading to a reverse von Kármán vortex street. In Fig. 4.3(b), we show that the beam midline deformation extracted from the simulation during

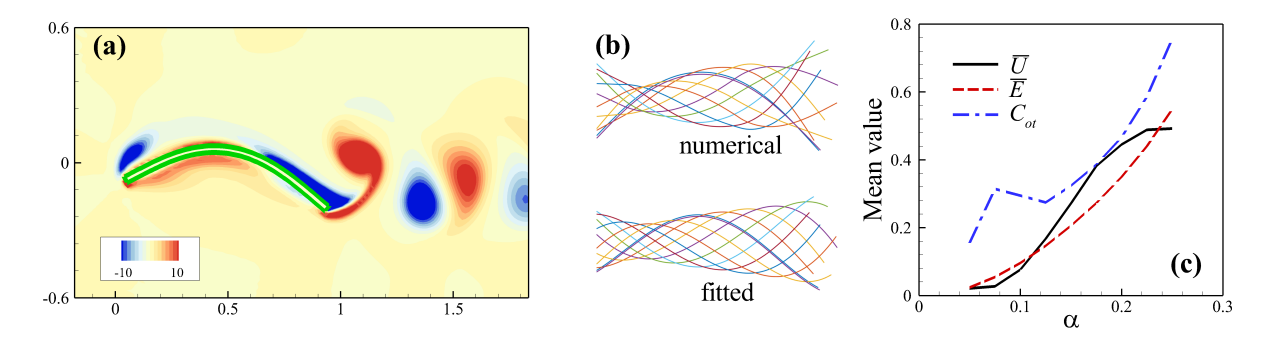


Figure 4.3: Free-swimming of a 2D elastic beam at Re = 500 and T = 2.0. (a) Instantaneous snapshot of vorticity field. (b) Envelope trajectories of the beam midline during one actuation period: (top) numerical results; (bottom) fitted results by Eq. (4.14). (c) Mean values of \overline{U} , \overline{E} , and C_{ot} as function of contraction strength α .

each time period (top), which can be approximately fitted by a weighted sine function (bottom):

$$\kappa(x,t) = (ax^2 + bx + c)\sin[2\pi(kx + \omega t) + \phi]. \tag{4.14}$$

In this case, we obtain the coefficients a=-1.27, b=0.92, c=0.07, k=0.4, $\omega=1.0$, and $\phi=0.5$. Upon comparison, there is good match between the simulation result and the fitted model in the middle section while the front and tail sections show slight discrepancies. Overall, we see that our simple three-parameter (α_0, β, T) actuation scheme with muscle contraction is capable of reproducing various types of traveling-wave-like swimming gaits that typically require a larger parameter space.

For the forward swimming cases ($\beta=0$), we have evaluated the mean values of swimming speed \overline{U} , elastic energy \overline{E} , and cost of transport C_{ot} as a function of the amplitude α_0 of muscle contraction when fixing Re = 500 and T=2. As shown in Fig. 4.3(c), the system exhibits largely monotonic behaviors for the three examined variables when the actuation strength α is selected between 0.05 and 0.25, with an exception for C_{ot} , which shows a local peak around $\alpha=0.08$. For very small values of α (α < 0.05), the soft swimmer does not show significant directional motion; when α > 0.25, we find that the average swimming speed (and hence also C_{ot}) decreases as α increases, suggesting that large body deformation does not necessarily lead to efficient swimming. In this study, we focus on the monotonic regime to facilitate controller design.

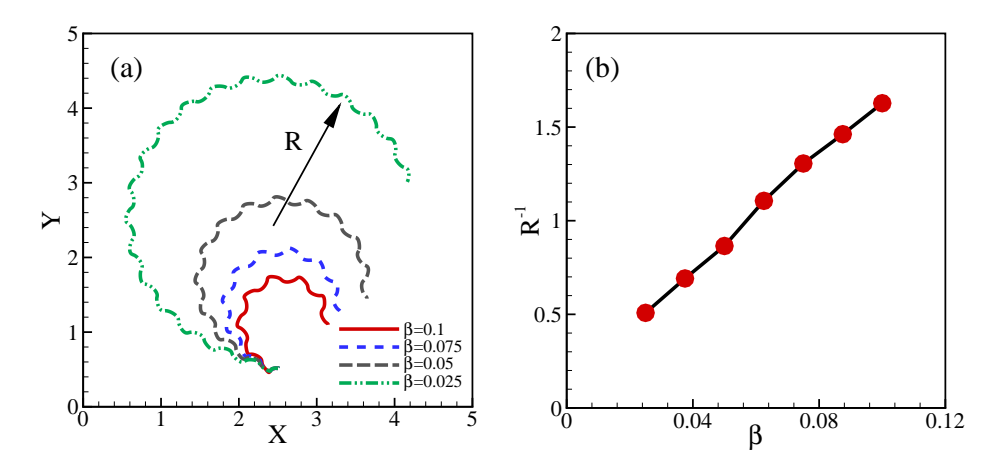


Figure 4.4: Simulation results for the soft swimmer at $\alpha_0 = 0.2$, Re = 500, and G = 1000: (a) Center of mass (CoM) paths at different values of β ; (b) Turning curvature R^{-1} as a function of β .

As discussed previously, specifying the empirical traveling-wave form of Eq. (4.14) only applies to the scenario of forward swimming. To achieve more elaborate maneuvering such as turning, we introduce a bias when applying contractions on the two sides of the swimming body. In Fig. 4.4, we demonstrate the effectiveness of the actuation scheme for turning with fixed actuation strength α_0 ($\alpha_0 = 0.2$) but increasing β . In Fig. 4.4(a), the swimmer's instantaneous CoM positions clearly show that it approximately follows a circular trajectory, the radius of which decreases (tighter turn) as the bias value β increases. Interestingly, the results in Fig. 4.4(b) suggest an almost linear relation between the bias value of β and the trajectory curvature R^{-1} (reciprocal of the radius).

4.3.2 Optimization and Analysis

4.3.2.1 Trajectory Comparison

To make sure the controller is effective, we optimize it by accounting for different scenarios of the moving target's characteristic velocity and the Reynolds number Re as defined at the end of Section 4.1. Note that we define Reynolds number in terms of the actuation frequency, not a physical velocity, so by varying Re we are implying a change in the fluid properties, namely the viscosity. In these studies we employ two different types of target trajectories, a straight path as characterized in Eq. (4.15) and a sinusoidal path as expressed in Eq. (4.16). The swimmer starts from at rest facing

along the x axis. We describe the straight trajectory of the target with a constant velocity v as

$$\mathbf{x}_{t} = \begin{cases} x_{t} = vt + x(0) \\ y_{t} = y(0) \end{cases}$$
 (4.15)

For the sinusoidal trajectory, the moving target has a constant velocity in the *x* direction, while its *y* position follows a sinusoidal function of time:

$$\mathbf{x}_t = \begin{cases} x_t = vt + x(0) \\ y_t = A\sin\omega t + y(0) \end{cases}$$
 (4.16)

Here we fix the amplitude, A=2, and angular frequency, $\omega=0.05\pi$. The inclusion of sinusoidal motion means that the swimmer has to constantly adjust its velocity and direction, which demonstrates its ability to follow complex paths. All cases are run with a maximum (dimensionless) simulation time of t=80, and as a precaution, the forward velocity controller is not activated until t=2 and the heading controller is not activated until t=4. Before these times, $\alpha_0=\alpha_{max}$ and $\beta=0$. The idea is to allow a smooth start and prevent potentially large values of β from negatively affecting the starting behavior of the swimmer, by first allowing it to achieve a significant forward velocity. However, testing has shown both restrictions to be unnecessary if β_{max} is sufficiently smaller than α_{max} .

In Fig. 4.5, we show the performance of a soft swimmer when subjected to different PID controllers by comparing its CoM trajectories with the specified straight (panel(a)) and sinusoidal (panel(b)) paths (black lines). Here we select two optimal solutions, corresponding to the case of lowest error \bar{e} ($min(\bar{e})$) and the case of a moderate error ($\bar{e} = 4.5$) but lowest elastic energy ($min(\bar{E})$) at Re = 500. For the minimum error examples in both panels, the swimmer quickly converges to the target point's position and is able to follow it closely. Note that the target is a moving point and not simply a designated path, meaning that a close match to the target trajectory implies the swimmer must be matching both the desired heading and velocity. Variation in the velocity can be discerned by observing the variation in the wavelength of the undulatory oscillations in the CoM trajectory. For a fixed driving frequency, the swimmer's velocity will correspond to the wavelength

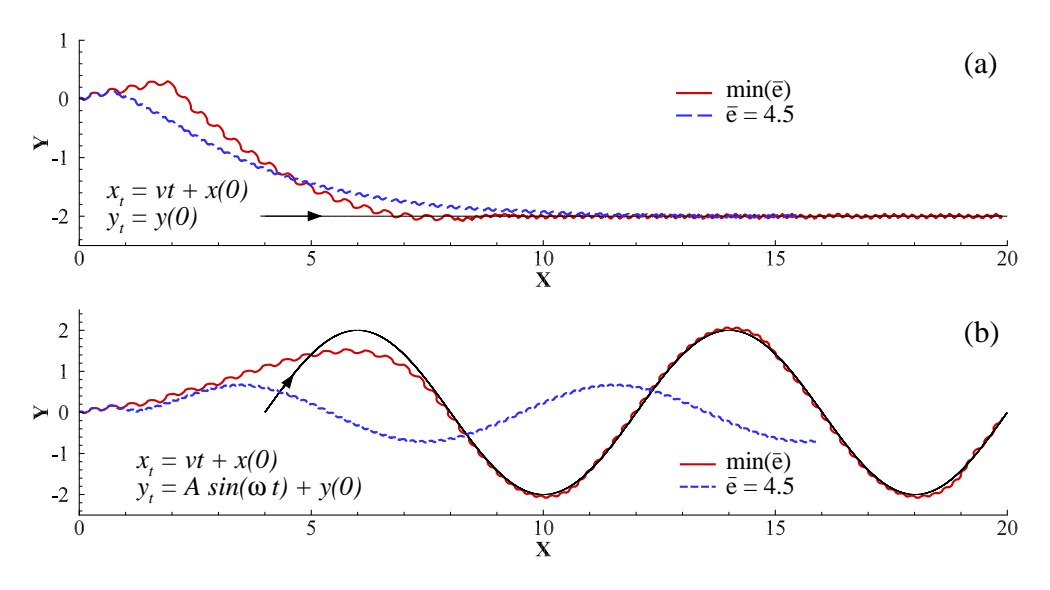


Figure 4.5: CoM trajectories of a soft swimmer tracking a moving target that is moving along both the (a) straight and (b) sinusoidal paths (black lines), when the swimmer is subjected to the PID control. The (red) and (blue) lines correspond to the controllers that have the lowest and a moderate error \bar{e} (but lowest elastic energy \bar{E}), respectively. The black arrows mark the target's moving directions.

of this oscillation. At the start the wavelength is long as the swimmer attempts to reach the target as quickly as possible. The wavelength then shortens as the swimmer approaches the target and matches its velocity. In the sinusoidal case, the wavelength is shorter near the peaks and longer in between corresponding to the velocity of the sine function which varies by the cosine. In contrast, for the moderate error case, we see that the swimmer appears to lag behind, and eventually fails to catch up to the target, although the small amplitudes (relative to the best \bar{e} cases) indicates lower contractile strengths which implies less deformation of the body and thus lower elastic strain energy.

4.3.2.2 Pareto Fronts of Optimized Solutions

Here we show global views of the obtained optimal solutions. Figure 4.6 compares the resulting Pareto fronts (a set of nondominated optimal solutions if no objective can be improved without sacrificing at least one other objective) in the space of objectives when the target velocity v takes different values while the Reynolds number Re is kept at 500, for the cases of straight trajectory ((a)-(d)) and sinusoidal trajectory ((e)-(h)), respectively. The obtained optimal solutions for these two

different paths are approximately allocated in the same regimes, exhibiting very similar patterns. Figure 4.7 shows the results when the Reynolds number is varied while the velocity is fixed at 0.2. All datasets shown correspond to a total of 50 generations of evolution with a child population of 64. The swimmer's body is neutrally buoyant with $\delta=0.5$ and non-dimensional parameters G=1000 and $\lambda_0=10^4$. It is worthwhile to mention that some portions of the objective space, and the individual solutions (PID parameters) that fall within, may be undesirable. For example, there are scenarios when the swimmer is barely moving and possibly not swimming at all. This "trivial" state can be interpreted using the three objectives, where the ideal optimal value of strain energy, $\bar{E}=0$, coincides with the trivial case of zero actuation, $\alpha_R=\alpha_L=0$. From the optimizer's prospective, this is a valid solution because our objective functions do not in any way represent this as a negative behavior. The objective functions could possibly be modified to avoid this trivial solution by adding a penalty function or cutoff, but such changes are undesirable since they could potentially add constraints or biases on the optimizer in unpredictable ways. Thus we stick to the original form of objective functions and remove trivial solutions in the end as part of the final decision-making process.

A 2D view of the Pareto front on the projected (\bar{E}, \bar{e}) plane can clearly reveal the effect of varying v on the resulting optimal solutions, as seen in Fig. 4.6(c) and (g). The distributions are clearly separate with the profile shifting up and right as v increases, both as expected, since increasing v indicates the increase in tracking difficulty and the requirement of higher actuation output. In comparison, the effect on C_{ot} as seen in Figs. 4.6 (b), (d), (f), and (h) appears to be minimal with the profiles being nearly independent of v.

Varying Re proves to have a significantly different effect with dependency apparent primarily in C_{ot} and \bar{E} as can be seen in Fig. 4.7. From Figs. 4.7(b), (d), (f), and (h), we see that as Re increases, C_{ot} drops. From Figs. 4.7(c) and (g), the elastic strain energy also drops with increasing Re. As Re increases the viscous forces acting on the swimmer decrease, leading to both a lower C_{ot} and actuation strength required to drive the swimmer. In all cases, for the regions where the error \bar{e} is low, there is an inverse relationship between C_{ot} and the error. The error proves

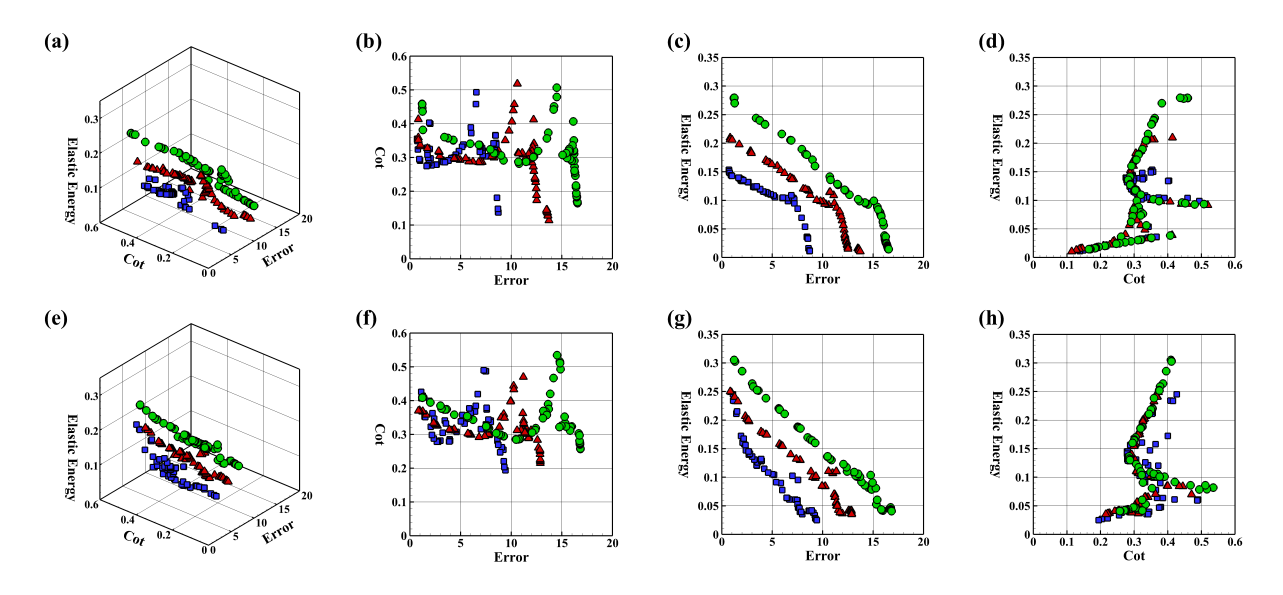


Figure 4.6: Pareto fronts in the space of tracking error (\bar{e}) , cost of transport (C_{ot}) , and elastic strain energy (\bar{E}) for various target speeds v with Re = 500. Blue-square: v = 0.1. Red-triangle: v = 0.2. Green-circle: v = 0.3. Straight path: (a-d). Sinusoidal path: (e-h). The leftmost panels (a) and (e) are 3D views of the objective spaces. The panels to their right are 2D projections of the respective distribution that visualize the trends between each pair of objectives. (b) and (f): \bar{e} vs C_{ot} . (c) and (g): \bar{e} vs \bar{E} . (d) and (h): C_{ot} vs \bar{E} .

to be mainly dominated by the positional error, e_1 , which in turn is logically inversely related to the swimmer's velocity. From this we can conclude that C_{ot} increases with increasing swimmer velocity as expected due to fluid drag.

4.3.2.3 Objective Correlations and Parameter Trends

In Fig. 4.8 we further compare the Pearson correlation coefficients of the objectives for each data set. The most apparent result is that in all cases the coefficient relating \bar{e} and \bar{E} is approximately equal to -1. This means that they are correlated strongly with an inversely proportional relationship, which is confirmed by observing panels (c) and (g) in Figs. 4.6 and 4.7 where the population in each dataset has a highly linear distribution. Physically this indicates that lower error requires stronger actuation. The strength of this correlation also implies that these objectives are not independent in our system. For example, it is not possible to find an optimal solution that decreases both \bar{e} and \bar{E} simultaneously.

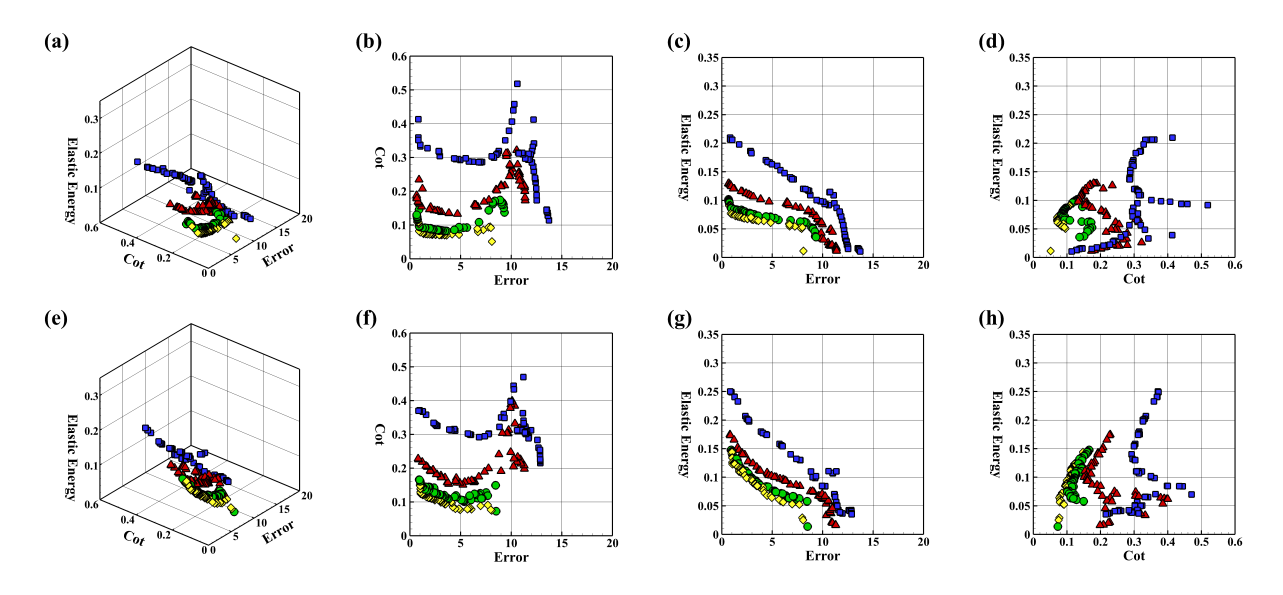


Figure 4.7: Pareto fronts in the space of tracking error (\bar{e}) , cost of transport (C_{ot}) , and elastic strain energy (\bar{E}) for various Re with v=0.2. Blue-square: Re = 500. Red-triangle: Re = 1000. Green-circle: Re = 1500. Yellow-diamond: Re = 2000. Straight path: (a-d). Sinusoidal path: (e-h). The leftmost panels (a) and (e) are 3D views of the objective spaces. The panels to their right are 2D projections of the respective distribution that visualize the trends between each pair of objectives. (b) and (f): \bar{e} vs C_{ot} . (c) and (g): \bar{e} vs \bar{E} . (d) and (h): C_{ot} vs \bar{E} .

The Pearson coefficients relating \bar{e} to C_{ot} as well as relating C_{ot} to \bar{E} do not show similarly clear patterns. Qualitatively, in the regions of lower \bar{e} there appear to be noticeable and consistent trends; however, when viewed as a whole, these fall apart. Thus without defining a criterion to trim the data set, a solid conclusion cannot be made. Interestingly it can be noted that coefficients relating \bar{e} to C_{ot} and those relating C_{ot} to \bar{E} appear to be equal in magnitude and inverted in sign. This can be explained by the objectives in each dataset falling roughly in a plane such that the distribution seen in panels (b) and (f) (corresponding to \bar{e} to C_{ot}) is the mirror of that seen in panels (d) and(h) (corresponding to C_{ot} to \bar{E}).

Furthermore, we seek more quantitative understandings of how the controller parameters vary when moving through the objective space. Considering the fact that the mapping between the objective and parameter space is neither necessarily smooth nor continuous, we emphasize that regions or even individuals in the Pareto optimal objective space must be "classified" into different groups that needs to be treated separately. For our study there is an obvious choice for classification,

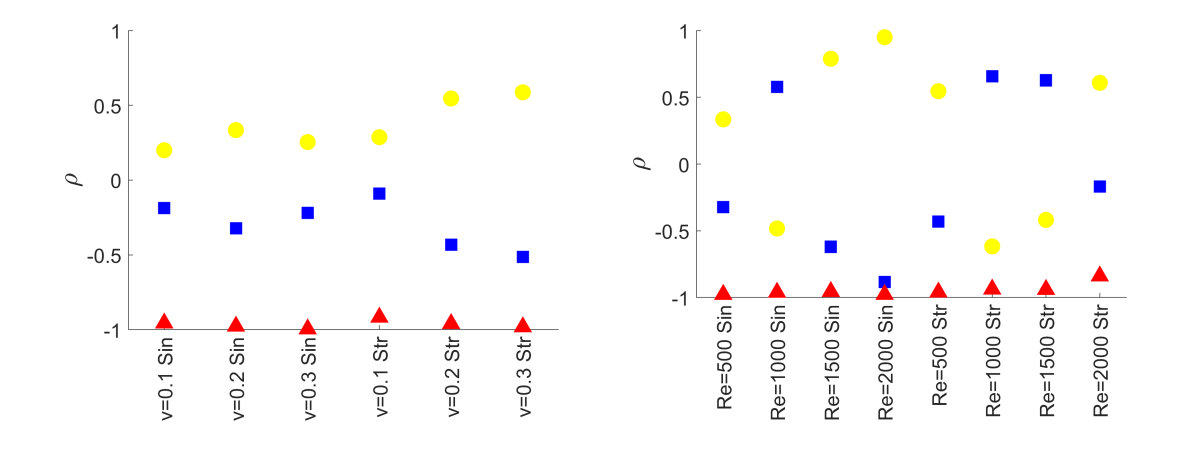


Figure 4.8: Comparison of the Pearson correlation coefficients (ρ) of the objectives for varying v (left) and varying Re (right). Blue-square = \bar{e} to C_{ot} . Red-triangle = \bar{e} to \bar{E} . Yellow-circle = C_{ot} to \bar{E} .

swimmers versus non-swimmers. As noted previously, there are effectively trivial solutions when \bar{E} is near zero and the error is correspondingly high. This occurs when the the contraction strength is sufficiently small such that the soft swimmer barely moves. By excluding these high error individuals (above roughly half the maximum error), we are left with parameter regions that may exhibit qualitatively clear trends in the objective space.

Fig. 4.9 shows the trends of $k_{p,position}$ versus error for all cases used in the optimization study at different values of v and Re. When near the minimum error, $k_{p,position}$ appears to reach maximum values, which corresponds to the optimal solutions near the upper bound of contraction strength α_0 . For fairly large error values, $k_{p,position}$ becomes negligible, corresponding to those trivial solutions with low \bar{E} . From the PID controller formulation in Eq. (4.8), $\alpha_0 \propto k_{p,position}e_1$, suggesting that when α_0 is properly bounded, larger controller gain $k_{p,position}$ results in reduced error.

Besides the $k_{p,position}$ – error relations, however, we did not find other clear trends when we sweep through the parameter space and connect the tuning parameters to the objectives. The data appear to be highly noisy, which is primarily due to the stochastic nature of evolutionary methods. We have observed that often times, they are able to converge rapidly to a certain optimum region, and then slowly approach the optimal solution(s) within via a stochastic search. Nevertheless, when comparing the obtained optimal tuning parameters for different target path (i.e., straight vs.

sinusoidal) as well as across Reynolds numbers (e.g., see Fig. 4.9), we have found that their values all fall into approximately the same ranges, indicating that these solutions indeed characterize the global optima. In other words, the proposed optimization approach seems to have produced PID controllers with near-optimal behavior across varying target behaviors and fluid environments.

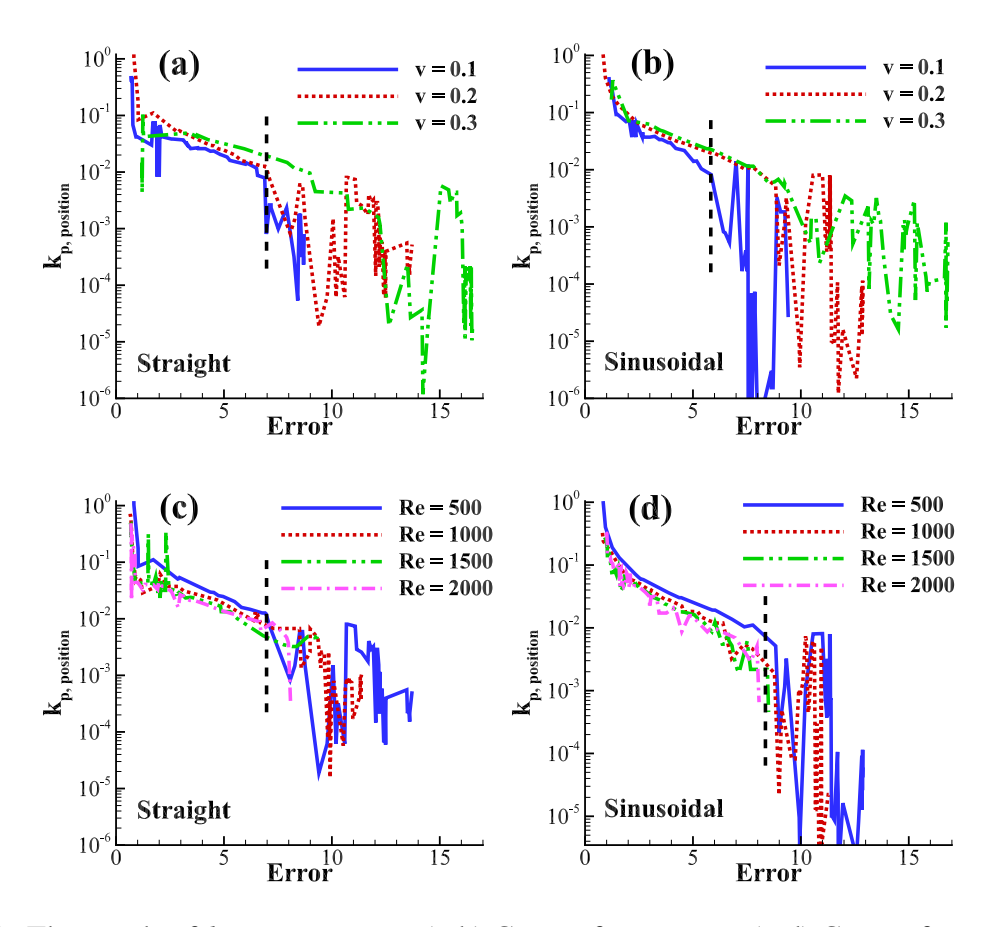


Figure 4.9: The trends of $k_{p,position}$ vs. \bar{e} . (a-b) Cases of varying v. (c-d) Cases of varying Re. (Left) panels are from the straight path and (right) from the sinusoidal path. The black dashed lines delineate the borders between the meaningful and trivial solutions.

4.4 Concluding Remarks

In this work we presented a new computational framework for optimizing feedback control of soft robotic fish enabled by muscle-like actuation. A novel fictitious domain/active-strain method [58] was employed to handle the resultant fluid-structure interaction when local contractile active strains – emulating muscle actuation – are imposed on the soft swimmer. In particular, using a 2D

elastic beam with finite width as a model for the soft swimmer, we demonstrated versatile swimming motions (forward swimming and turning at different velocities and radii, for example) by varying the strength and bias of the active strains imposed on both sides of the swimmer. Two PID controllers are adopted for adjusting the actuation strength (α_0) and bias (β), respectively, for the swimmer to track a moving target. With this setup, multi-objective optimization of the controller parameters was conducted using the U-NSGA-III algorithm, where three objectives were considered, including the tracking error, cost of transport, and elastic strain energy. The PID controller parameters were optimized using a series of moving target trajectories, involving different speeds and Reynolds numbers for two types of paths (straight and sinusoidal). By analyzing the resulting Pareto fronts, the study revealed the trends of how the obtained values of objectives are influenced by the target trajectory conditions. It also showed the correlation and trade-offs among the objectives under feedback control, as well as how the optimized controller parameters are related to the objectives and trajectory conditions. Overall, this work has shown the feasibility of using high-fidelity CFD to design and optimize feedback control for soft robotic fish subject to multiple, potentially conflicting objectives.

There are a few directions for future work. First, we will consider the extension of the presented framework to the case where the soft swimmer has a 3D geometry and a more general form of distributed actuation. Second, while PID controllers were used as an example of model-free controller in this work, we plan to exploit the computation data and system ID techniques to obtain the dynamic model of a soft swimmer, based on which model-based controllers (such as linear quadratic regulator (LQR) and model-predictive control [8]) will be developed and evaluated. Ultimately, it is our plan to experimentally validate the modeling, control, and optimization methods with a soft robotic fish prototype actuated by smart materials (e.g., shape memory alloys or dielectric elastomer actuators).

CHAPTER 5

FUTURE WORK

5.1 Body Shape Optimization for Muscle Driven Undulatory Swimming

In Chapter 4 we demonstrate the effectiveness of coupling our simulation techniques to multiobjective evolutionary optimizers for design purposes. The question now is how far can we push the envelope and how many factors can be included in an optimization. Most existing studies are limited to single objective methods and/or simplified swimmer models. To build off of these studies we attempt a multi-objective optimization of the body shape of a soft, artificial muscle driven swimmer using our high fidelity simulation method. Body shape is of course important from a hydrodynamic perspective but also because it directly influences the gait of soft swimmers. How well or even if a soft robot can swim depends on the mechanical response of the body which is determined by it's shape and actuation scheme. So to start we elect to optimize the body of a 2D robotic fish with a simple actuation scheme similar to that used previous in the plate fish.

Three objectives were chosen to optimize: swimming speed (max), swimming efficiency (max), and average elastic energy (min). The swimming speed is a self explanatory measure of the effectiveness of the swimmer. The swimming efficiency is defined by the ratio of the kinetic energy to the energy transferred to the fluid over a given period. This provides a measure of how well the swimmer translates expended energy into useful locomotion. Lastly, the average elastic energy of the body relates to the strength of the required actuators (muscles), overall energy expenditure, and material fatigue.

To vary the shape, the swimmers body is defined via multiple points connected by an interpolating Catmull-Rom spline with bilateral symmetry. Fig. 5.1 shows a randomly sampled swimmer from an initial population. Actuation is limited to an active region of fixed length and strength, the position of which is also evolved. As in the plate fish, the actuation is approximated to be at the surface via exponential decay into the body. The local depth and direction of the actuation at a

point inside the body is determined from the linear surface mesh.

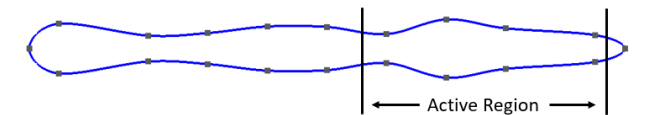


Figure 5.1: An example of a randomly generated swimmer body. The blue line is the body surface and the dots are interpolation points for the Catmull-Rom spline. Muscle actuation is limited to within the active region.

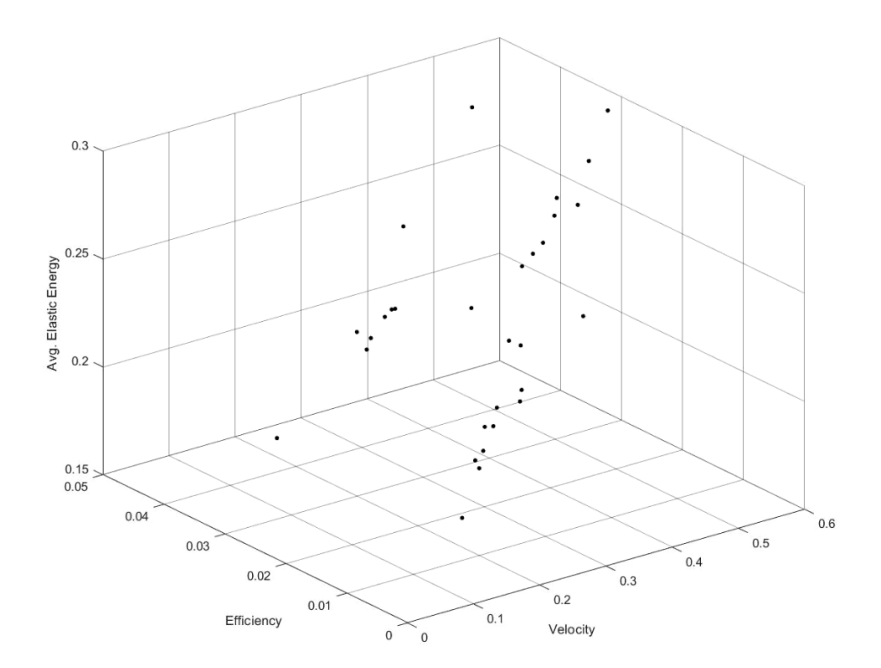


Figure 5.2: Sample objective space population distribution for generation 100 of a variable body shape optimization.

Fig. 5.2 shows a sample population from a variable body shape optimization as was just defined. By nature it is difficult to visualize the objective space of problems with 3 or more objectives in a 2D format. Here the surface correlating to the population is concave into the image. When fully converged, each individual represents a potentially optimal configuration. Convergence is difficult to define and usually involves simply running the optimization until the population sufficiently settles. This does not guarantee that the true Pareto front has been found but for complex systems even a partial optimization can be useful when the alternative is often none at all. Fig. 5.3 is an attempt

at visualizing the convergence by focusing only on the extremes, the best value present for each objective in a given population. This ignores the intermediate individuals meaning convergence here does not indicate overall convergence. However, since overall convergence does require the extremes to be converged it provides a necessary but not sufficient convergence condition.

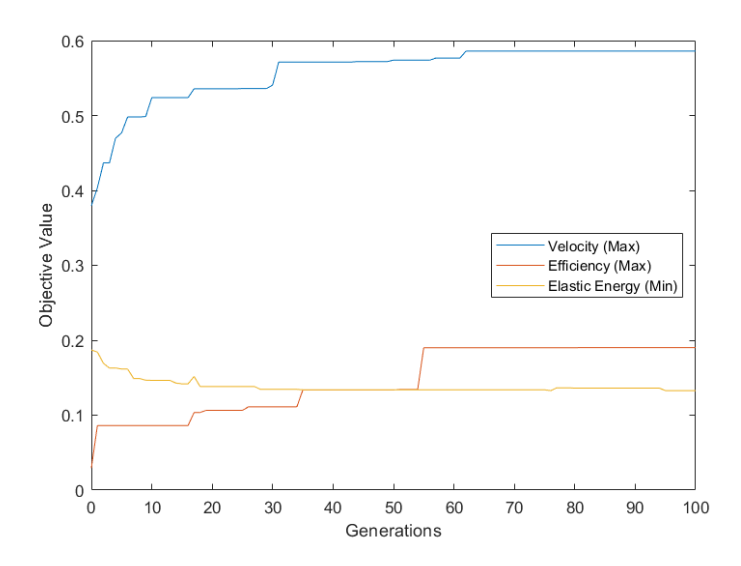


Figure 5.3: Sample convergence history of the extreme (most optimal) values for each objective in a variable body shape optimization.

The stair step pattern in the convergence history is characteristic of evolutionary optimization. Each jump corresponds to a random variation that lead to positive change. Plateaus occur where the variations produce nonviable or negative change. As the generation count increases the plateaus tend to grow longer since the more converged the solution is, the more likely a random variation will be harmful. Thus demonstrating how evolutionary methods can quickly find the general location of an optimum but converge to an exact value slowly. The significant changes in the objective values from beginning to end seemed to indicate that the optimization was able to progress meaningfully.

Fig. 5.4 shows the individuals corresponding to the extreme objective values sampled at progressive generations. Analyzing the final generation (gen. 100) it is apparent that the fastest (a) and lowest average elastic energy (c) individuals have evolved toward a slender body reminiscent of an eel or tadpole with a streamlined and highly flexible body. The fastest individual resembles the plate fish except with a pronounced head that we hypothesize reduces head motion which is a

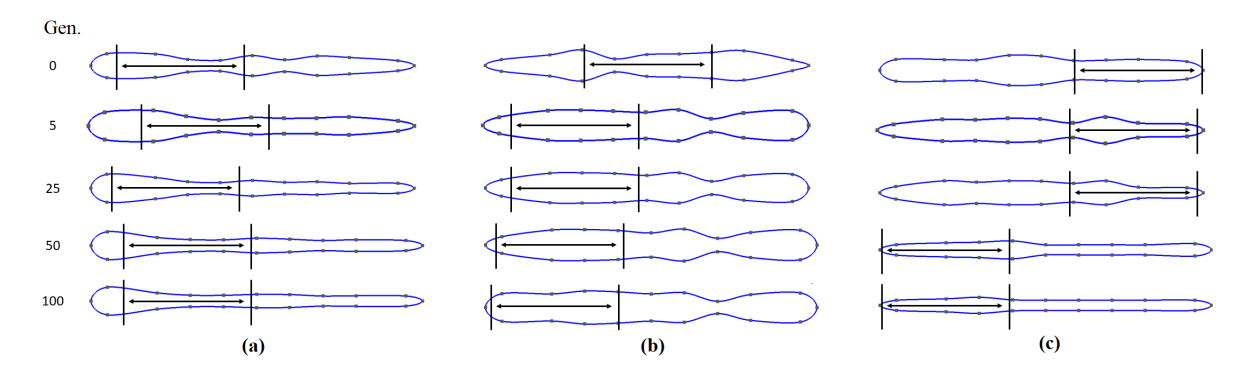


Figure 5.4: Sample configurations over progressive generations: (a) fastest swimming speed, (b) highest swimming efficiency, and (c) lowest average elastic energy.

major source of drag. In the case of elastic energy, a slender body reduces the bending stiffness of the body and thus the elastic energy stored in the body for a given deformation. The high efficiency individual is the exception with a thick body that seems to limit the amplitude of the propulsive paddling motion. The exact advantage is not clear but the less chaotic motion of the body may reduce the presence of drag generating fluid structures such as leading edge vortices.

The current trajectory for work in this area is focused on enabling and optimizing more complicated actuation schemes. The simplicity of the actuation scheme allowed us to qualitatively verify the effectiveness of the optimization by repeatedly producing the tadpole shape that we see in nature and with similar performance to our undulating plate. Ideally, we would like to simultaneously optimize the body shape along with a complex, full body actuation scheme akin to existing studies [99]. The major issue with evolving the actuation pattern is that for the case of elastic energy, and to some degree efficiency, the optimizer will tend toward the trivial solutions where the actuation strength is near zero everywhere, such that the swimmer is effectively turned off. These swimmers clearly do not achieve any useful swimming velocity which defeats the overall purpose of the study. Thus a major goal is to find a way to promote a minimum level of swimming speed that neither overly suppresses exploration nor requires modification of the evolutionary algorithms.

CHAPTER 6

CONCLUSIONS

We set out on this project with the intent to develop a computational framework that would help drive the growth of soft robotics research and technology in ways existing simulations and experiments could not yet achieve. Previously existing and commonly used simulation techniques for FSI generally contain some form of limitation that prevents them from capturing the full, rich physics of swimming soft robots. Often times these limitations stem from assumptions and reduced models that greatly simplify the problem at the cost of an acceptable loss of physical accuracy and generality for their originally intended purposes. For muscle driven, fully soft, swimming robots the list of valid assumptions becomes much smaller and so to achieve a viable level of physical accuracy we are forced to look to more complete, more general, and more expensive methods.

In this work we presented a holistic computational framework for the design and optimization of soft robotic fish powered by artificial muscle along with complementary investigations of phenomena related to fluid/elastic-structure interaction. The active strain method when coupled with the distributed Lagrange multiplier/fictitious domain method allows for high fidelity, fully coupled simulations of soft robots that employ muscle driven undulating, jetting, and paddling propulsion. By coupling these simulations with a multi-objective evolutionary optimization method we demonstrated that it is possible to design and optimize maneuverable, feedback controlled muscle driven soft swimming robots. We have also investigated the effect of solid viscoelasticity on the behavior of instabilities at a fluid-solid interface and noted key regions where the effects are most pronounced.

We believe we have achieved our original goal and hope that this work can useful in promoting the field of fully soft swimming robots by providing tools and insights that can be used to investigate designs and materials that are still maturing, too expensive, or too complex for large scale studies. We believe it also has the potential to act as a reference for developing new reduced order and machine learning based models where experimental data is currently of limited supply.

BIBLIOGRAPHY

BIBLIOGRAPHY

- [1] S. Alben, L. Miller, and J. Peng. Efficient kinematics for jet-propelled swimming. *J. Fluid Mech.*, 733:100, 2013.
- [2] D. Ambrosi and S. Pezzuto. Active stress vs. active strain in mechanobiology: constitutive issues. *Journal of Elasticity*, 107(2):199–212, 2012.
- [3] C. Antoci, M. Gallati, and S. Sibilla. Numerical simulation of fluid–structure interaction by sph. *Comput. Struct.*, 85:879–890, 2007.
- [4] N. W. Bartlett, M. T. Tolley, J. T. Overvelde, J. C. Weaver, B. Mosadegh, K. Bertoldi, G. M. Whitesides, and R. J. Wood. A 3D-printed, functionally graded soft robot powered by combustion. *Science*, 349:161–165, 2015.
- [5] T. Belytschko, W. K. Liu, B. Moran, and K. Elkhodary. *Nonlinear Finite Elements for Continua and Structures*. John Wiley & Sons, 2013.
- [6] R. Bhardwaj and R. Mittal. Benchmarking a coupled immersed-boundary-finite-element solver for large-scale flow-induced deformation. *AIAA Journal*, 50:1638–1642, 2011.
- [7] J. C. Case, E. L. White, and R. K. Kramer. Sensor enabled closed-loop bending control of soft beams. *Smart Materials and Structures*, 25(4):045018, 2016.
- [8] M. Castano and X. Tan. Model predictive control-based path following for tail-actuated robotic fish. *Journal of Dynamic Systems, Measurement and Control*, 141(7):071012, 2019.
- [9] S. Chandrasekhar. *Hydrodynamic and Hydromagnetic Stability*. Oxford University Press, 1961.
- [10] D. Chen, S. Cai, Z. Suo, and R. Hayward. Surface energy as a barrier to creasing of elastomer films: an elastic analogy to classical nucleation. *Phys. Rev. Lett.*, 109(3):038001, 2012.
- [11] K. Chen. Elastic instability of the interface in couette flow of viscoelastic liquids. *J. Non-Newtonian Fluid Mech*, 40:261–267, 1991.
- [12] Q. Chen, Q. Zhong, M. Qi, and X. Wang. Comparison of vortex identification criteria for planar velocity fields in wall turbulence. *Physics of Fluids*, 27(8):085101, 2015.
- [13] S. Chen and G. Doolen. Lattice boltzmann method for fluid flows. *Annu. Rev. Fluid Mech.*, 30:329, 1998.

- [14] S. Chester and L. Anand. A coupled theory of fluid permeation and large deformations for elastomeric materials. *Journal of the Mechanics and Physics of Solids*, 58:1879–1906, 2010.
- [15] C. Christianson, N. N. Goldberg, D. D. Deheyn, S. Cai, and M. T. Tolley. Translucent soft robots driven by frameless fluid electrode dielectric elastomer actuators. *Science Robotics*, 3(17):eaat1893, 2018.
- [16] S. Colin and J. Costello. Morphology, swimming performance and propulsive mode of six co-occurring hydromedusae. *J. Exp. Biol.*, 205:427, 2002.
- [17] S. Colin, J. Costello, and E. Klos. *IN* SITU swimming and feeding behavior of eight co-occurring hydromedusae. *Mar. Ecol. Prog. Ser.*, 253:305, 2003.
- [18] J. Costello, S. Colin, and J. Dabiri. Medusan morphospace: phylogenetic constraints, biomechanical solutions, and ecological consequences. *Invertebr. Biol.*, 127:265, 2008.
- [19] J. Dabiri, S. Colin, J. Costello, and M. Gharib. Flow patterns generated by oblate medusan jellyfish: field measurements and laboratory analyses. *J. Exp. Biol.*, 208:1257, 2005.
- [20] J. Dabiri, S. Colin, K. Katija, and J. Costello. A wake-based correlate of swimming performance and foraging behavior in seven co-occurring jellyfish species. *J. Exp. Biol.*, 213:1217, 2010.
- [21] K. Deb and H. Jain. An evolutionary many-objective optimization algorithm using reference-point-based nondominated sorting approach, Part I: solving problems with box constraints. *IEEE Transactions on Evolutionary Computation*, 18:577–601, 2014.
- [22] K. Deb, A. Pratap, S. Agarwal, and T. Meyarivan. A fast and elitist multiobjective genetic algorithm: nsga-ii. *IEEE Transactions on Evolutionary Computation*, 6:182–197, 2002.
- [23] D. Drotman, S. Jadhav, M. Karimi, P. Dezonia, and M. T. Tolley. 3D printed soft actuators for a legged robot capable of navigating unstructured terrain. In *2017 IEEE International Conference on Robotics and Automation (ICRA)*, pages 5532–5538. IEEE, 2017.
- [24] F. Fang, K. Ho, L. Ristroph, and M. Shelley. A computational model of the flight dynamics and aerodynamics of a jellyfish-like flying machine. *J. Fluid Mech.*, 819:621, 2017.
- [25] L. Fauci and A. McDonald. Sperm motility in the presence of boundaries. *Bulletin of Mathematical Biology*, 57:670–699, 1995.
- [26] C. Gambini, B. Abou, A. Ponton, and A. J. M. Cornelissen. Micro- and macrorheology of jellyfish extracellular matrix. *Biophys. J.*, 102:1–9, 2012.

- [27] T. Gao and H. H. Hu. Deformation of elastic particles in viscous shear flow. *J. Comput. Phys.*, 228:2132–2151, 2009.
- [28] T. Gao, H. H. Hu, and P. Ponte Castañeda. Rheology of a suspension of elastic particles in a viscous shear flow. *J. Fluid Mech.*, 687:209–237, 2011.
- [29] T. Gao, H. H. Hu, and P. Ponte Castañeda. Shape dynamics and rheology of soft elastic particles in a shear flow. *Phys. Rev. Lett.*, 108:058302, 2012.
- [30] T. Gao, Y. Tseng, and X. Lu. An improved hybrid cartesian/immersed boundary method for fluid-solid flows. *Int. J. Numer. Meth. Fluids*, 55:1189–1211, 2007.
- [31] M. Gazzola, A. A. Tchieu, D. Alexeev, A. de Brauer, and P. Koumoutsakos. Learning to school in the presence of hydrodynamic interactions. *Journal of Fluid Mechanics*, 789:726–749, 2016.
- [32] M. Gazzola, W. M. Van Rees, and P. Koumoutsakos. C-start: optimal start of larval fish. *Journal of Fluid Mechanics*, 698:5–18, 2012.
- [33] V. Gkanis and S. Kumar. Instability of creeping couette flow past a neo-hookean solid. *Phys. Fluids*, 15:2864–2471, 2003.
- [34] V. Gkanis and S. Kumar. Stability of pressure-driven creeping flows in channels lined with a nonlinear elastic solid. *J. Fluid Mech.*, 524:357–375, 2005.
- [35] R. Glowinski, T.-W. Pan, T. I. Hesla, and D. D. Joseph. A distributed lagrange multiplier/fictitious domain method for particulate flows. *International Journal of Multiphase Flow*, 25:755–794, 1999.
- [36] C. Hamlet, L. J. Fauci, and E. D. Tytell. The effect of intrinsic muscular nonlinearities on the energetics of locomotion in a computational model of an anguilliform swimmer. *Journal of Theoretical Biology*, 385:119–129, 2015.
- [37] X. He and L. Luo. Lattice boltzmann model for the incompressible navier–stokes equation. *J. Stat. Phys.*, 88:927, 1997.
- [38] G. Hersch and L. Miller. Reynolds number limits for jet propulsion: a numerical study of simplified jellyfish. *J. Theor. Biol.*, 285:84, 2011.
- [39] A. V. Hill. The heat of shortening and the dynamic constants of muscle. *Proceedings of the Royal Society of London. Series B-Biological Sciences*, 126(843):136–195, 1938.
- [40] H. H. Hu, M. Y. Zhu, and N. Patankar. Direct numerical simulations of fluid solid systems using the arbitrary lagrangian eulerian technique. *J. Comput. Phys.*, 169:427–462, 2001.

- [41] H. Huang and X.-Y. Lu. An ellipsoidal particle in tube poiseuille flow. *Journal of Fluid Mechanics*, 822:664–688, 2017.
- [42] H. Huang, X. Yang, and X.-y. Lu. Sedimentation of an ellipsoidal particle in narrow tubes. *Physics of Fluids*, 26(5):053302, 2014.
- [43] W.-X. Huang and H. J. Sung. Three-dimensional simulation of a flapping flag in a uniform flow. *Journal of Fluid Mechanics*, 653:301–336, 2010.
- [44] H. Jain and K. Deb. An evolutionary many-objective optimization algorithm using reference-point-based nondominated sorting approach, part ii: handling constraints and extending to an adaptive approach. *IEEE Transactions on Evolutionary Computation*, 18:602–622, 2014.
- [45] D. D. Joseph. *Fluid Dynamics of Viscoelastic Liquids*. Applied mathematical sciences, Vol. 84, Springer Verlag, New York, 1990.
- [46] V. Kalro and T. Tezduyar. A parallel 3d computational method for fluid-structure interactions in parachute systems. *Comput. Meth. Appl. Mech. Eng.*, 190:321, 2000.
- [47] Y. Katz, K. Tunstrøm, C. C. Ioannou, C. Huepe, and I. D. Couzin. Inferring the structure and dynamics of interactions in schooling fish. *Proceedings of the National Academy of Sciences*, 108(46):18720–18725, 2011.
- [48] S. Kern and P. Koumoutsakos. Simulations of optimized anguilliform swimming. *Journal of Experimental Biology*, 209(24):4841–4857, 2006.
- [49] J. Kim, D. Kim, and H. Choi. An immersed-boundary finite-volume method for simulations of flow in complex geometries. *Journal of Computational Physics*, 171:132–150, 2001.
- [50] S.-W. Kim, J.-G. Lee, S. An, M. Cho, and K.-J. Cho. A large-stroke shape memory alloy spring actuator using double-coil configuration. *Smart Materials and Structures*, 24(9):095014, 2015.
- [51] V. Kumaran, G. H. Fredrickson, and P. Pincus. Flow-induced instability at the interface between a fluid and a gel at low reynolds number. *J. Phys. II France*, 4:893–911, 1994.
- [52] V. Kumaran and R. Muralikrishnan. Spontaneous growth of fluctuations in the viscous flow of a fluid past a soft interface. *Phys. Rev. Lett.*, 84:3310–3313, 2000.
- [53] C. Lai, Z. Zheng, E. Dressaire, G. Ramon, H. Huppert, and H. Stone. Elastic relaxation of fluid-driven cracks and the resulting backflow. *Phys. Rev. Lett.*, 117:268001, 2016.
- [54] E. H. Lee and D. T. Liu. Finite-strain elastic-plastic theory particularly for plane wave analysis. *Journal of Applied Physics*, 38:19–27, 1967.

- [55] E. H. Lee. Elastic-plastic deformation at finite strains. *Journal of Applied Mechanics*, 36(1):1–6, 1969.
- [56] L. Li, S. Sherwin, and P. Bearman. A moving frame of reference algorithm for fluid/structure interaction of rotating and translating bodies. *International Journal for Numerical Methods in Fluids*, 38:187–206, 2002.
- [57] M. J. Lighthill. Note on the swimming of slender fish. *Journal of Fluid Mechanics*, 9:305–317, 1960.
- [58] Z. Lin, A. Hess, Z. Yu, S. Cai, and T. Gao. A fluid-structure interaction study of soft robotic swimmer using a fictitious domain/active-strain method. *Journal of Computational Physics*, 376:1138–1155, 2019.
- [59] C. Macosko. *Rheology: Principles, Measurements and Applications*. VCH Publishers, New York, 1994.
- [60] C. Majidi. Soft robotics: a perspective—current trends and prospects for the future. *Soft Robotics*, 1:5–11, 2014.
- [61] J. Martins, E. Pires, R. Salvado, and P. Dinis. A numerical model of passive and active behavior of skeletal muscles. *Computer methods in applied mechanics and engineering*, 151(3-4):419–433, 1998.
- [62] A. Masud and T. Hughes. A space-time galerkin/least-squares finite element formulation of the navier-stokes equations for moving domain problems. *Comput. Methods Appl. Mech. Eng.*, 146:91–126, 1997.
- [63] N. G. McCrum, C. P. Buckley, and C. B. Bucknall. *Principles of Polymer Engineering*. Oxford University Press, 1997.
- [64] L. Mihai and A. Goriely. Positive or negative poynting effect? the role of adscititious inequalities in hyperelastic materials. In *Proc. R. Soc. Lond. A*, volume 467 of number 2136, pages 3633–3646, 2011.
- [65] A. Miriyev, K. Stack, and H. Lipson. Soft material for soft actuators. *Nature Communications*, 8(1):596, 2017.
- [66] R. Mittal, H. Dong, M. Bozkurttas, F. Najjar, A. Vargas, and A. von Loebbecke. A versatile sharp interface immersed boundary method for incompressible flows with complex boundaries. *Journal of Computational Physics*, 227(10):4825–4852, 2008.
- [67] R. Mittal and G. Iaccarino. Immersed boundary methods. *Annu. Rev. Fluid Mech.*, 37:239–261, 2005.

- [68] S. Mora, T. Phou, J.-M. Fromental, L. M. Pismen, and Y. Pomeau. Capillarity driven instability of a soft solid. *Phys. Rev. Lett*, 105:214301, 2010.
- [69] R. Muralikrishnan and V. Kumaran. Experimental study of the instability of the viscous flow past a flexible surface. *Phys. Fluids*, 14:775–780, 2002.
- [70] J. Nawroth, H. Lee, A. Feinberg, C. Ripplinger, M. McCain, A. Grosberg, J. Dabiri, and K. Parker. A tissue-engineered jellyfish with biomimetic propulsion. *Nature Biotechnology*, 30:792–797, 2012.
- [71] R. W. Ogden. Nonlinear Elastic Deformations. Dover, 1984.
- [72] V. Palmre, J. J. Hubbard, M. Fleming, D. Pugal, S. Kim, K. J. Kim, and K. K. Leang. An ipmc-enabled bio-inspired bending/twisting fin for underwater applications. *Smart Materials and Structures*, 22(1):014003, 2012.
- [73] S. Park, C. Chang, W. Huang, and H. Sung. Simulation of swimming oblate jellyfish with a paddling-based locomotion. *J. Fluid Mech.*, 748:731, 2014.
- [74] S. Park, M. Gazzola, K. Park, S. Park, V. Di Santo, E. Blevins, J. Lind, P. Campbell, S. Dauth, A. Capulli, F. Pasqualini, S. Ahn, A. Cho, H. Yuan, B. Maoz, R. Vijaykumar, J. Choi, K. Deisseroth, G. Lauder, L. Mahadevan, and K. Parker. Phototactic guidance of a tissue-engineered soft-robotic ray. *Science*, 353:158–162, 2016.
- [75] S. Park, B. Kim, J. Lee, W. Huang, and H. Sung. Dynamics of prolate jellyfish with a jet-based locomotion. *J. Fluids Struct.*, 57:331, 2015.
- [76] J. K. Parrish, S. V. Viscido, and D. Grunbaum. Self-organized fish schools: an examination of emergent properties. *The Biological Bulletin*, 202(3):296–305, 2002.
- [77] C. S. Peskin. The immersed boundary method. *Acta Numer.*, 10:479–517, 2002.
- [78] J. Poynting. On pressure perpendicular to the shear planes in finite pure shears, and on the lengthening of loaded wires when twisted. *Proc. R. Soc. Lond. A*, 82(557):546–559, 1909.
- [79] E. M. Purcell. Life at low reynolds number. *Am. J. Phys.*, 45:3–11, 1977.
- [80] Y. Renardy. Stability of the interface in two-layer couette flow of upper convected maxwell liquids. *J. Non-Newtonian Fluid Mech.*, 28:99–115, 1988.
- [81] L. Ristroph and S. Childress. Stable hovering of a jellyfish-like flying machine. *J. R. Soc. Interface*, 11:20130992, 2014.

- [82] D. E. Rivera, M. Morari, and S. Skogestad. Internal model control: PID controller design. *Industrial & Engineering Chemistry Process Design and Development*, 25(1):252–265, 1986.
- [83] M. Al-Rubaiai, T. Pinto, D. Torres, N. Sepulveda, and X. Tan. Characterization of a 3d-printed conductive pla material with electrically controlled stiffness. In ASME 2017 Conference on Smart Materials, Adaptive Structures and Intelligent Systems, V001T01A003–V001T01A003. American Society of Mechanical Engineers, 2017.
- [84] D. Rus and M. T. Tolley. Design, fabrication and control of soft robots. *Nature*, 521:467–475, 2015.
- [85] M. Sahin and K. Mohseni. An arbitrary lagrangian-eulerian formulation for the numerical simulation of flow patterns generated by the hydromedusa aequorea victoria. *J. Comput. Phys.*, 228:4588, 2009.
- [86] M. Sahin, K. Mohseni, and S. Colin. The numerical comparison of flow patterns and propulsive performances for the hydromedusae *s*arsia tubulosa and *a*equorea victoria. *J. Exp. Biol.*, 212:2656, 2009.
- [87] B. Saintyves, T. Jules, T. Salez, and L. Mahadevan. Self-sustained lift and low friction via soft lubrication. *Proc. Natl. Acad. Sci.*, 113(21):5847–5849, 2016.
- [88] H. Seada and K. Deb. A unified evolutionary optimization procedure for single, multiple, and many objectives. *IEEE Transactions on Evolutionary Computation*, 20:358, 2016.
- [89] W. Shan, S. Diller, A. Tutcuoglu, and C. Majidi. Rigidity-tuning conductive elastomer. *Smart Materials and Structures*, 24(6):065001, 2015.
- [90] J. Skotheim and L. Mahadevan. Soft lubrication. Phys. Rev. Lett., 92(24):245509, 2004.
- [91] Z. Suo. Theory of dielectric elastomers. *Acta Mechanica Solida Sinica*, 23:549–578, 2010.
- [92] P. L. Tallec and J. Mouro. Fluid structure interaction with large structural displacements. *Comput. Methods Appl. Mech. Eng.*, 190:3039–3067, 2001.
- [93] J. Teran, L. Fauci, and M. Shelley. Viscoelastic fluid response can increase the speed and efficiency of a free swimmer. *Physical Review Letters*, 104:038101, 2010.
- [94] F.-B. Tian, H. Dai, H. Luo, J. F. Doyle, and B. Rousseau. Fluid–structure interaction involving large deformations: 3d simulations and applications to biological systems. *Journal of computational physics*, 258:451–469, 2014.

- [95] H. Tian, Z. Wang, Y. Chen, J. Shao, T. Gao, and S. Cai. Polydopamine-coated main-chain liquid crystal elastomer as optically driven artificial muscle. *ACS Applied Materials & Interfaces*, 10(9):8307–8316, 2018.
- [96] S. Trabia, Z. Olsen, and K. J. Kim. Searching for a new ionomer for 3d printable ionic polymer–metal composites: aquivion as a candidate. *Smart Materials and Structures*, 26(11):115029, 2017.
- [97] S. Turek and J. Hron. Proposal for numerical benchmarking of fluid-structure interaction between an elastic object and laminar incompressible flow. In *Fluid-structure interaction*, pages 371–385. Springer, 2006.
- [98] E. D. Tytell, M. C. Leftwich, C.-Y. Hsu, B. E. Griffith, A. H. Cohen, A. J. Smits, C. Hamlet, and L. J. Fauci. Role of body stiffness in undulatory swimming: insights from robotic and computational models. *Physical Review Fluids*, 1(7):073202, 2016.
- [99] W. M. van Rees, M. Gazzola, and P. Koumoutsakos. Optimal morphokinematics for undulatory swimmers at intermediate reynolds numbers. *Journal of Fluid Mechanics*, 775:178–188, 2015.
- [100] T. Williams, G. Bowtell, and N. Curtin. Predicting force generation by lamprey muscle during applied sinusoidal movement using a simple dynamic model. *J. Exp. Biol.*, 201:869, 1998.
- [101] J.-Z. Wu, H.-Y. Ma, and M.-D. Zhou. *Vorticity and Vortex Dynamics*. Springer, 2006.
- [102] C. Xuan and J. Biggins. Finite-wavelength surface-tension-driven instabilities in soft solids, including instability in a cylindrical channel through an elastic solid. *Phys. Rev. E*, 94(2):023107, 2016.
- [103] X. Yang, X. Zhang, Z. Li, and G.-W. He. A smoothing technique for discrete delta functions with application to immersed boundary method in moving boundary simulations. *Journal of Computational Physics*, 228(20):7821–7836, 2009.
- [104] Z. Yu. A DLM/FD method for fluid/flexible-body interactions. *Journal of Computational Physics*, 207:1–27, 2005.
- [105] Z. Yu, Y. Wang, and X. Shao. Numerical simulation of the flapping of a three-dimensional flexible plate in uniform flow. *J. Sound Vib.*, 331:4448–4463, 2012.
- [106] Z. S. Yu and X. M. Shao. A three-dimensional fictitious domain method for the simulation of fluid-structure interactions. *Journal of Hydrodynamics Ser B*, 22(5):178–183, 2010.
- [107] Z. Yu and X. Shao. A direct-forcing fictitious domain method for particulate flows. *Journal of Computational Physics*, 227:292–314, 2007.

- [108] J. Zhang, S. Childress, A. Libchaber, and M. Shelley. Flexible filaments in a flowing soap film as a model for one-dimensional flags in a two-dimensional wind. *Nature*, 408:835–838, 2000.
- [109] J. Zhou, R. J. Adrian, S. Balachandar, and T. Kendall. Mechanisms for generating coherent packets of hairpin vortices in channel flow. *Journal of fluid mechanics*, 387:353–396, 1999.